ISBN 90-365-1928-4

Heteroepitaxial growth of copper oxide superconductors by PLD

Victor Leca 2003

Heteroepitaxial growth of copper oxide superconductors by Pulsed Laser Deposition

Victor Leca

Heteroepitaxial growth of copper oxide superconductors by pulsed laser deposition

Ph.D. committee:

Chairman
Prof. Dr. D. Feil (University of Twente)

Secretary
Prof. Dr. D. Feil (University of Twente)

Supervisors
Prof. Dr. H. Rogalla (University of Twente)
Prof. Dr. ing. D.H.A. Blank (University of Twente)

Assistant supervisor
Dr. ing. A.J.H.M. Rijnders

Members
Prof. Dr. G. Balestrino (Universita di Roma "Tor Vergata", Italy)
Prof. Dr. K.J. Boller (University of Twente)
Prof. Dr. ir. B. Poelsema (University of Twente)
Prof. Dr. M. Rusu (University of Bucharest, Romania)
Dr. B. Dam (Vrije Universiteit Amsterdam)

The work described in this thesis has been financially supported by the "Stichting voor Fundamenteel Onderzoek der Materie" (FOM). It was carried out in the Low Temperature Division of the Department of Applied Physics and MESA+ Research Institute at the University of Twente, P.O. Box 217, 7500 AE Enschede, The Netherlands.

V. Leca
Heteroepitaxial growth of copper oxide superconductors by Pulsed Laser Deposition,
Ph.D. thesis University of Twente, Enschede, The Netherlands.

ISBN 90-365-1928-4

Print: Printpartners Ipskamp, Enschede

HETEROEPITAXIAL GROWTH OF COPPER OXIDE SUPERCONDUCTORS BY PULSED LASER DEPOSITION

PROEFSCHRIFT

ter verkrijging van
de graad van doctor aan de Universiteit Twente,
op gezag van de rector magnificus,
prof. dr. F.A. van Vught,
volgens besluit van het College voor Promoties
in het openbaar te verdedigen
op donderdag 5 juni 2003 te 15.00 uur

door

Victor Leca
geboren op 5 november 1966
te Campulung Arges (Roemenië)

Dit proefschrift is goedgekeurd door:

Prof. Dr. H. Rogalla (promotor)
Prof. Dr. ing. D.H.A. Blank (promotor) en
Dr. ing. A.J.H.M. Rijnders (assistent-promotor)

Contents

Chapter 1

Introduction

Development of devices based on high-temperature superconductor (HTSc) ceramics[1] requires knowledge of material aspects like the crystal structure and physicochemical properties. Great efforts have therefore been put to understand the dependence between the synthesis method and the properties of these compounds. A description of the main structural aspects of this class of materials (i.e., the role of the oxygen network and the charge reservoir concept) is given in the first part of Chapter 2.

The simplest structure among the HTSc materials is that of the $ACuO_2$ (A = alkaline earth metals) infinite layer (IL) compounds. It consists of corner-shared CuO_2 layers and A-metal(s) planes, alternately stacked along the c-axis. With the exception of the $Ca_{1-x}Sr_xCuO_2$ (with x = 0.15) member, the IL compounds are metastable phases that require high-pressure and high-temperature conditions for their synthesis. However, two end-member compounds, i.e., $BaCuO_2$ and $CaCuO_2$, are still difficult to be synthesized in bulk.[2,3] By using the stabilization effect of closely lattice matched substrates (e.g., $SrTiO_3$), these phases can be grown as thin films by means of deposition techniques such as molecular beam epitaxy (MBE), reactive sputtering, pulsed laser deposition (PLD), or chemical vapour deposition (CVD).[4] The oxygen pressure used during deposition of the IL films results in structural modifications that have substantial influence on their electrical transport properties.[5-7]

Superconductivity can be induced in the IL compounds by electron or hole doping. Hole doping (p-type) can be obtained through different methods: introduction of excess oxygen in the A-plane, creating alkaline earth deficient defect layers in the structure, or by monovalent ion (e.g., Na^+, Li^+) substitution.[5] The bulk p-type ILs show superconductivity with T_c[i] values as high as 110 K.[8] Electron doping (n-type) of IL phases is obtained by partial substitution of alkaline earth atoms with lanthanide Ln^{3+} (Ln = La, Pr, Nd, Sm, or Gd) atoms.[9] The $Sr_{1-x}Ln_xCuO_2$ compounds, synthesized at high-

[i] T_c represents the critical transition temperature below which a material becomes superconductor.

pressure and high-temperature conditions, show superconductuctivity with a maximum T_c of 43 K. The properties of $Sr_{1-x}Ln_xCuO_2$ thin films are not as good as those achieved in the bulk.[10,11] For example, T_c as high as 39 K was obtained only recently[12] for $Sr_{0.9}La_{0.1}CuO_2$ thin films grown by MBE on (001) $KTaO_3$. A short presentation of the synthesis methods (bulk and thin film) and properties of p- and n-type IL compounds is given in second part of Chapter 2.

Physical vapour deposition (PVD) techniques such as PLD and MBE are effectively used for the epitaxial growth of metastable and artificially structured oxides. These structures are stabilized by deposition on a lattice-matched substrate, with control of the stacking sequence at the atomic level.[5] The oxidation power during growth should be sufficiently high to enable growth of stable phases.[13,14] This can be achieved using relatively high oxygen pressures (i.e., 10^{-3}-1 mbar). Control of the growth process by *in situ* monitoring methods such as reflection high-energy electron diffraction (RHEED) is hampered at these pressures due to scattering of the electrons by the ambient gas. This problem was overcome with the development of high-pressure RHEED.[15] A short description of the high-pressure RHEED system is given in Chapter 3.

In PLD, the high deposition rates attained during the deposition pulse and the variable range of the kinetic energy of the deposited particles can be exploited to improve the film properties (e.g., crystallinity and surface smoothness). Taking advantage of the growth kinetics at the high supersaturation reached during the deposition pulses, a new approach has been developed, called pulsed laser interval deposition (PLiD).[16] This method enables 2-dimensional (2 D) growth and, therefore, a smooth film surface. A short presentation of the method will be given in Chapter 3. Its use in imposing layer-by-layer growth will be demonstrated for $ACuO_2$ phases and artificially layered structures, build by sequential deposition of different IL blocks.

Besides the control of the growth conditions, the fabrication of artificially layered structures using layer-by-layer growth requires an optimum surface smoothness of the starting substrate. The chemistry and morphology of the terminating atomic layer(s) influences the film-substrate interface properties and, consequently, the structural and physical properties of the film. Therefore, a substrate with good lattice matching and an atomically smooth surface with a known composition are essential. Commercially available single-crystal oxide wafers have a surface that is not sufficiently smooth for atomic layer epitaxy of complex oxide materials.[17-19] Different techniques have been used to improve the surface quality, including annealing in vacuum or oxygen,[20,21] the use of buffer layers[22] and chemical etching with a buffered NH_4F + HF (or BHF) solution.[17,19,20] The latter is successfully applied to reproducible obtain single TiO_2-terminated $SrTiO_3$ substrates.[15,17] In order to control the chemistry and morphology of the surface terminating layer(s) of $NdGaO_3$, $SrTiO_3$, LSAT, and $KTaO_3$ substrates, used for the studies in this thesis, different chemical and thermal treatment methods were developed. The preparation techniques and resulting substrate surface properties are presented in Chapter 4. Artificially layered structures of $BaCuO_2$/(Sr,Ca)CuO_2 and $SrCuO_2$/$CaCuO_2$ were synthesized by using these single terminated substrates and manipulated PLD growth technique. The results are given in Chapter 5.

Norton *et al.*[23] suggested that $BaCuO_2$/$SrCuO_2$ artificially layers structures grown on $SrTiO_3$ are not optimally doped; the T_c of these compounds might increase with an

increase or decrease in the hole carrier density. One possible solution for modifying the carrier density concentration is to apply a different level of strain[ii] on the CuO_2 planes by using a different substrate (e.g., $NdGaO_3$). This will result in an increased compressive strain applied to the CuO_2 planes[iii]. Therefore, $NdGaO_3$ single-crystal substrates were used as template layer in order to study the role of the compressive strain and of the deposition conditions on the structural and electrical properties of these structures. The results of epitaxial growth of infinite layer and IL artificially layered structures on (001) and (110) $NdGaO_3$ will be presented in Chapter 5 as well.

High-pressure RHEED, AFM, high-resolution electron microscopy (HREM), and electron diffraction (ED) measurements were used to study the growth and structural properties of $Sr_{1-x}La_xCuO_2$ ($0.10 \leq x \leq 0.20$). Roughening of the film surface is observed by RHEED during the initial growth, i.e., during growth of the first ~ 10 unit cell layers. PLiD and $BaTiO_3$ buffer layers were used in order to improve the quality of the substrate-film interface and, as a result, the smoothness of the film. For $Sr_{1-x}Ln_xCuO_2$ thin films, the superconducting transition temperature is modified by the strain due to the lattice misfit between the substrate and the film. For the compressive strained n-type IL films, T_c is reduced due to difficulty in removing the excess oxygen from the Sr(Ln) planes. Improved T_c values can be obtained by inducing tensile strain in the CuO_2 planes.[12] Here, the role of the substrate on the structural and electrical properties of PLD grown $Sr_{1-x}La_xCuO_2$ films, with tetragonal symmetry, will be presented and discussed in Chapter 6. Two types of substrates, i.e., $SrTiO_3$ and $KTaO_3$ (cubic symmetry, a = 3.989 Å), with or without a $BaTiO_3$ buffer layer, were used for these experiments.

In conclusion, the results on PLD (or PLiD) growth and properties of the simplest cuprate superconductors, i.e., the infinite layers compounds, will be discussed in Chapter 5, for the hole-doped $ACuO_2$ (A = Ca, Sr, Ba) phases, and in Chapter 6, for the electron-doped $Sr_{1-x}La_xCuO_2$ compounds. Different substrates ($NdGaO_3$, $SrTiO_3$ or $KTaO_3$) were used to stabilize these metastable structures using epitaxial growth. The role of the compressive or tensile strain in stabilization of p- or n-type IL phase will also be discussed. The IL compounds are ideal candidates for studies of the formation of artificially layered structures. PLiD growth of IL artificially layered structures on $NdGaO_3$ substrates by sequentially ablating $ACuO_2$ targets will be discussed in Chapter 5. A critical parameter in the film growth process is the substrate-film interface, determining the morphology and structural properties of the film. To improve the substrate surface morphology different chemical or thermal treatment were developed and the results will be presented in Chapter 4 for $NdGaO_3$, $SrTiO_3$, LSAT, $SrLaAlO_4$, and $KTaO_3$ substrates.

[ii] For hole doping a compressive strain is required.

[iii] The in-plane cell parameter of $NdGaO_3$ is a ~ 3.86 Å (for the pseudo-cubic cell; see Chapter 4), while for $SrTiO_3$ (cubic symmetry) its value is a = 3.905 Å.

References

1 J.G. Bednorz and K.A.Z. Muller, *Z. Phys. B* **64**, 189 (1986)
2 Z. Hiroi, M. Takano, M. Azuma and Y. Takeda, Nature **364**, 315 (1993); H. Ihara, K. Tokiwa, H. Ozawa, M. Hirabayashi, A. Negishi, H. Matuhata and Y.S. Song, *Jpn. J. Appl. Phys.* **33**, L503 (1994)
3 D.H. Lowndes, D.B. Geohegan, A.A. Puretzky, D.B. Norton and C.M. Rouleau, *Science* **273**, 898 (1996); C. Aruta, G. Balestrino, R. Desfeux, S. Martellucci, A. Paoletti and G. Petrocelli, *Appl. Phys. Lett.* **68**, 926 (1996); G. Balestrino, S. Martellucci, P.G. Medaglia, A. Paoletti, G. Petrocelli and A. A. Varlamov, *Phys. Rev. B* **58**, R8925 (1998)
4 D.B. Norton, B.C. Chakoumakos and J.D. Budai, *SPIE Proc* **2697**, 295 (1996)
5 A. Gupta, *Current opinion in Solid State and Material Science* **2**, 23 (1997)
6 A. Gupta, B.W. Hussey, T.M. Shaw, A.M. Guloy, M.Y. Chern, R.F. Saraf and B.A. Scott, *J. Solid State Chem.* **112**, 113 (1994)
7 T. Maeda, M. Yoshimoto, K. Shimozono and H. Koinuma, *Physica C* **247**, 142 (1995)
8 H. Zhang, L.D. Marks, Y.Y. Wang, H. Zhang, V.P. Dravid, P. Han and D.A. Payne, *Ultramicroscopy* **57**, 103 (1995)
9 see, e.g., M.G. Smith, A. Manthiram, J. Zhou, J.B. Goodenough and J.T. Markert, *Nature* **351**, 549 (1991)
10 C. Niu and C.M. Lieber, *Appl. Phys. Lett.* **61**, 1712 (1992)
11 N. Sugii, K. Matsuura, K. Kubo, K. Yamamoto, M. Ichikawa and H. Yamauchi, *J. Appl. Phys.* **74**, 4047 (1993)
12 S. Karimoto, K. Ueda, M. Naito and T. Imai, *Appl. Phys. Lett.* **79**, 2767 (2001)
13 D.H.A. Blank, D.J. Adelerhof, J. Flokstra and H. Rogalla, *Physica C* **162 - 164**, 125 (1989)
14 R.H. Hammond and R. Bormann, *Physica C* **162 - 164**, 703 (1989)
15 A.J.H.M. Rijnders, G. Koster, D.H.A. Blank and H. Rogalla, *Appl. Phys. Lett.* **70**, 1888 (1997)
16 G. Koster, A.J.H.M. Rijnders, D.H.A. Blank and H. Rogalla, *Appl. Phys. Lett.* **74**, 3729 (1999)
17 M. Kawasaki, K. Takahashi, T Maeda, R. Tsuchiya, M. Shinohara, O. Ishiyama, T. Yonezawa, M. Yoshimoto and H. Koinuma, *Science* **226**, 1540 (1994)
18 A.J.H.M. Rijnders, *The initial growth of complex oxides: study and manipulation*, PhD thesis ISBN 9036516579, University of Twente, The Netherlands (2001)
19 G. Koster, B.L. Kropman, A.J.H.M. Rijnders, D.H.A. Blank and H. Rogalla, *Appl. Phys. Lett.* **73**, 2920 (1998)
20 V. Leca, G. Rijnders, G. Koster, D.H.A. Blank and H. Rogalla, *Mat. Res. Soc. Symp.* **587**, O3.6.1 (2000)
21 M. Yoshimoto, H. Ohkubo, N. Kanda and H. Koinuma, *Jpn. J. Appl. Phys.* **31**, 3664 (1992)
22 M.Y. Chern, A. Gupta, B.W. Hussey and T.M. Shaw, *J. Vac. Sci. Technol.* **A11**, 637 (1991)
23 D.P. Norton, B.C. Chakoumakos, J.D. Budai, D.H. Lowndes, B.C. Sales, J.R. Thompson and D.K. Kristen, *Science* **265**, 2074 (1994)

Chapter 2

Structural aspects in cuprate superconductors

2.1 Introduction

Based on the studies of isolated Jahn-Teller ions in perovskite insulators, Georg Bednorz and Alex Müller showed in 1986 that ceramic materials based on copper, lanthanum and barium oxides (i.e., $La_{2-x}Ba_xCuO_4$) can superconduct below 30 K.[1,2] Discovery of superconductivity in cuprates was followed by the synthesis of the first compound ($YBa_2Cu_3O_{7-x}$, $T_c = 93$ K, Wu *et al.*, January 1987)[3] that shows superconductivity at a temperature higher than that of the boiling point of liquid nitrogen, a coolant cheaper than He. Since then several homologous series of compounds with $T_c > 100$ K were synthesised, the highest T_c (164 K) being obtained for $HgBa_2Ca_2Cu_3O_{8+\delta}$ (Hg1223).[4] This temperature is only 19 K lower than the lowest recorded temperature reached under natural conditions on Earth. The evolution of the superconducting transition temperature after the discovery of the phenomenon in 1911 is presented in Fig. 2.1. With the exception of two types of cuprate systems (the electron doped T'-phases $Nd_{2-x}Ce_xCuO_4$ and the infinite layer $Sr_{1-x}Ln_xCuO_2$ compounds), all high-T_c superconductors (HTSc) show p-type (hole) conductivity.

In the first part of this chapter, the crystal structure of the copper oxide superconductors will be described, with focus on the charge reservoir concept and the role of the oxygen network. Secondly, two methods that can be used to stabilize metastable phases, i.e. high-pressure synthesis and thin film growth, will be discussed. A short presentation of the synthesis and properties of infinite-layer compounds will be given in the last sections of the chapter.

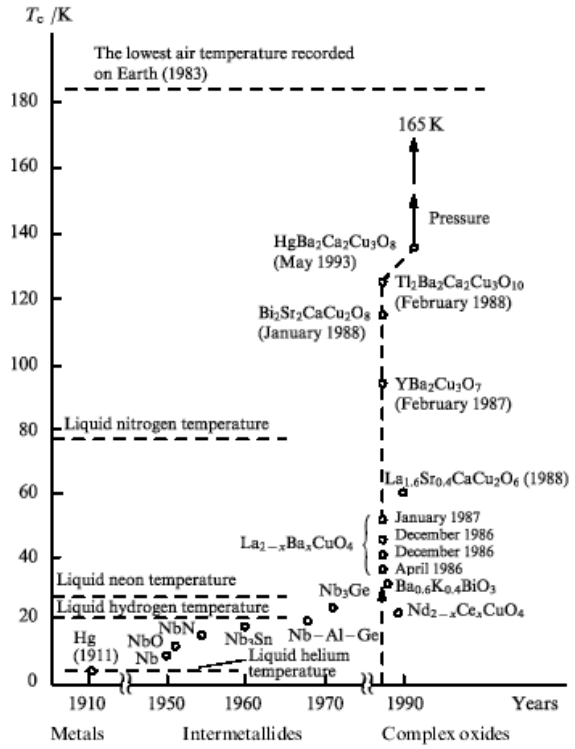

Fig. 2.1 *Superconducting critical temperature versus date (from Ref. 5).*

2.2 High-T_c superconductors

2.2.1 Structural aspects

Almost all HTSc's are layered copper-containing complex oxides whose structure contains oxygen deficient perovskite-like blocks. The two-dimensional CuO_2 planes (see Fig. 2.2a), with a formal charge of 2^-, consists of divalent copper and oxygen ions forming a square network with the oxygen atoms placed on the lines connecting the copper sites.[2,6-8] Although the mechanism of high T_c superconductivity has not yet been fully elucidated, it is generally accepted that this plane plays an essential role in the formation of the Cooper pairs, and therefore, in the appearance of superconductivity itself.[6-8] Divalent copper ion is a d^9 ion, therefore metallic behaviour is expected for a compound containing such ions.[8] However, because of the strong electron-electron interaction, the ninth electron tends to be localized on each copper site, resulting in semiconducting or insulating behaviour. At certain temperature, i.e., T_c, superconductivity appears if the CuO_2 plane is doped with holes (or electrons), so that the formal valence of the copper ion deviates from 2^+.[2,8] There is an optimum doping level for holes (electrons) and both underdoping and overdoping may deplete superconductivity or even completely suppress it (see Fig. 2.3).

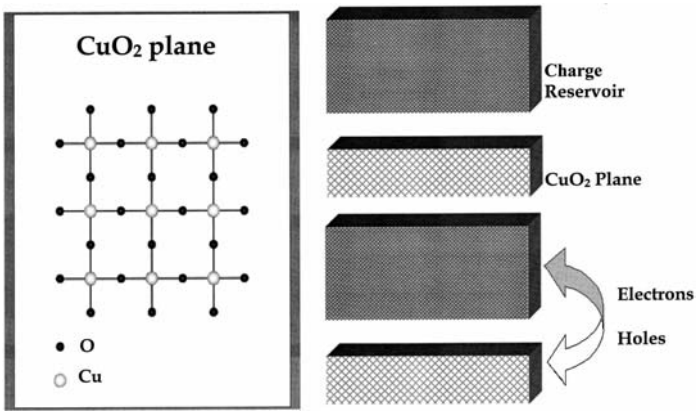

(a) *(b)*

Fig. 2.2 *(a) CuO_2 planes made from CuO_4 squares sharing corner oxygen. (b) Schematic view of the electronic layers in copper oxide superconductors (from Ref. 2).*

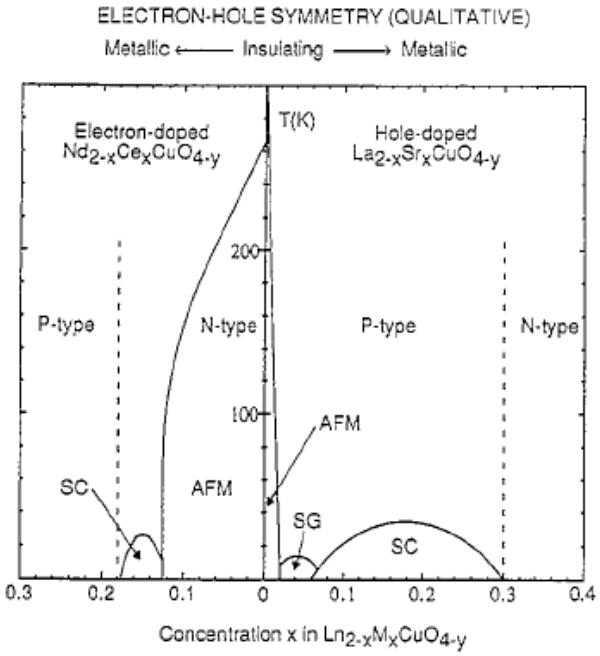

Fig. 2.3 *Temperature-dopant concentration (T-x) phase diagram indicating the regions of superconductivity and antiferomagnetic ordering of the Cu^{2+} ions for two type of copper-based superconductors: the hole-doped $La_{2-x}Sr_xCuO_4$ (right) and electron-doped $Nd_{2-x}Ce_xCuO_{4-y}$ (left).*
AFM = antiferromagnetic phase, SG = spin-glass phase, and SC = superconducting phase (from Ref. 9).

2.2.1.1 Charge reservoir

A high T_c cuprate superconductor is characterized by the simultaneous presence in the structure of two different functional blocks, individually non-superconducting:
1. a layered structure based on the CuO_2 planes, i.e., the *infinite layer* (IL) block, and
2. in between these CuO_2 planes, a certain structural block, called *charge reservoir* (CR), where charge carriers are created and doped into the CuO_2 plane (see Fig. 2.2b). The CR sub-unit easily incorporates extra-oxygen ions, uncompensating the electrical charge of the whole structure. The CR blocks serve to control, through chemistry, the number of electrons in the CuO_2 planes and to connect or isolate the CuO_2 planes in the third dimension.[8]

Superconductivity is induced through manipulation of the CR layer either by adding oxygen, by partial substitution of one atom of higher or lower valence, or by the naturally occurring electron count present because of the valences of the atoms in the compound.[8,10-14] Manifestation of superconductivity requires the formal oxidation state of copper in the CuO_2 plane to be within the range from +2.05 to +2.25 for hole-doped superconductors (e.g., RE123, Bi-, Tl- and Hg-families) or from +1.8 to +1.9 for electron doped cuprates.[8,15] The Cu-O bond length within a CuO_x layer should be around 0.190-0.198 nm, with the distance between the nearest copper atoms of 0.380-0.395 nm, in order for superconductivity to occur. The Cu-O from neighbouring layers (the so called apical positions of oxygen) should be much longer (> 0.22 nm). Because of the oxygen distribution in the structure, the superconducting cuprates contain strong in-plane bonds in CuO_2 layers and weaker bonds perpendicular to these layers. Because of the characteristic layered structure almost all HTSc materials posses a very high crystallographic anisotropy of physical properties.

In a compound containing a number n of CuO_2 planes, the hole distribution is not simple, the average copper valence may not be an exact measure of the effective carrier concentration. If one assumes that a constant number of holes are created in the charge reservoir and the holes are equally distributed in all CuO_2 planes, the hole concentration per copper atom decreases linearly with n. This variation of the hole concentration (average copper valence) with n suggests that a higher (lower) oxygen pressure is needed to stabilize a higher (lower) n member.[16] A systematic decrease of the carrier concentration with n (for $n > 3$) has been reported for several HTSc homologous series (Fig. 2.4), the n-value being considered one of the most important factors governing the carrier concentration. Further complications may come from various kinds of crystal defects that are often introduced into the HTSc. An average copper valence based on an ideal composition may sometimes be inaccurate because of excess lattice oxygen, oxygen or cation vacancies, mutual substitution of cations, etc.[16,17]

The variation of T_c is not always dependent on the changes of charge carriers' concentration.[18] T_c also depend on both d(Cu-Cu) in the CuO_2 plane and on ones between adjacent CuO_2 planes.[19] These distances can be modified by applying pressure (i.e., during bulk high pressure synthesis)[20] or epitaxial strain[21]. However, these distances can depend also on geometric factors, such as cation sizes in the CR block.

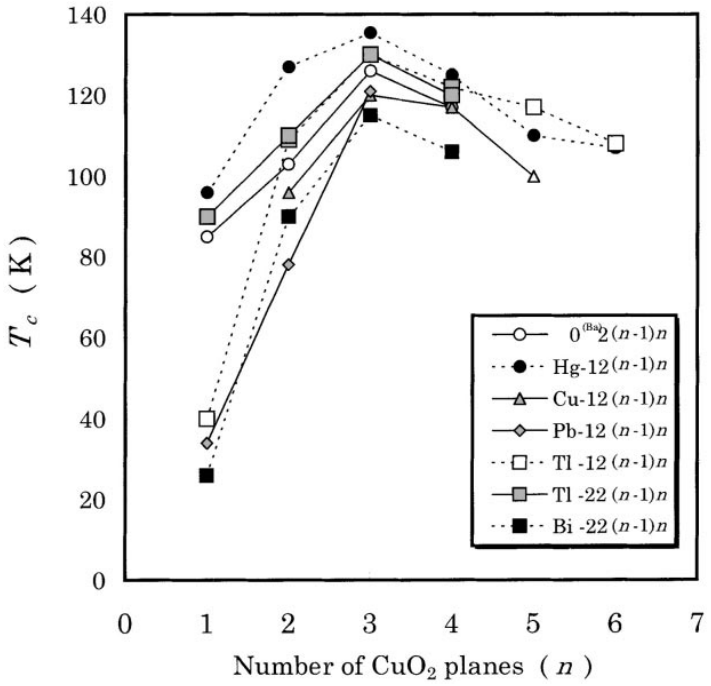

Fig. 2.4 *Superconducting transition temperature, T_c, versus number of stacked CuO_2 planes, n, for various homologous series. The n = 3 member of each homologous series most likely has the highest T_c (from Ref. 22).*

2.2.1.2 Oxygen network

The oxygen network plays an important role in creating charge carriers in HTSc. Its content affects both the concentration of the charge (hole) carriers in superconducting CuO_2 planes and the average Cu-O bond length and represents one of the factors influencing the stability of HTSc phases.[8] In this section, the main characteristics of the oxygen network in HTSc materials will be presented.

Among transition metal compounds, oxides are characterized by intermediate covalency, i.e., they possess an adequate extent of overlap between the d orbitals of the transition metal and the p orbitals of oxygen that favours delocalization of the charge. In high T_c-copper oxides, control over the charge carrier concentration has been achieved by tuning the 'nominal' valence value of the transition metal atoms. In order to tune the transition metal valence, structures allowing for oxygen non-stoichiometry are advantageous. Within the conductive transition-metal/oxygen framework the charge has to be uniformly distributed between each copper-oxygen network to ensure delocalisation of the carriers. Discovery of high-T_c superconductivity was facilitated by successful valence-tuning studies of Cu in the layered LaBaCuO system, for which Michel *et al.*[10] had previously demonstrated the occurrence of different oxidation states of copper.

Common to all metal oxides is that the Gibbs free energy of formation becomes less negative with increasing temperature. Therefore, metal oxides tend to be reduced, i.e.,

to lose oxygen, upon heating in air or even in oxygen gas. Obviously, with decreasing partial pressure of oxygen, reduction temperatures of metal oxides are lowered. For most of the metal oxides, reduction occurs in one or two discrete steps. However, for some transition metal oxides continuous variation of oxygen stoichiometry, i.e. oxygen non-stoichiometry, is allowed within certain limits set by the structure. In both cases, according to thermodynamics, oxygen tends to incorporate back into the reduced form of the oxide, i.e. metal or oxygen-deficient oxide, upon cooling. Of course, the kinetics of the back-oxygenation strongly depends on the system.

Tunability of oxygen non-stoichiometry and thereby the mixed-valence of the transition metal constituent by means of various reductive and oxidative annealing is especially common for perovskite-related structures. By modifying the oxygen content, it is possible to tune the valence of copper by selecting an appropriate temperature for the annealing. The perovskite-derived high-T_c superconductive copper oxides possess the ability to absorb and desorb oxygen reversibly upon normal-pressure annealing.[22] The changes in oxygen stoichiometry occur in the CR block only. Not only the amount but also the exact location of oxygen atoms in the superconductor crystal lattice influences the properties of the material.

Although the number of charge carriers is commonly associated with the oxidation state of copper, the excess positive or negative charge in a superconductor CuO_2 plane is likely to be delocalised over the framework formed by the copper atom and its surrounding oxygen atoms. The distribution of holes between copper and oxygen in the CuO_2 plane is important in terms of controlling T_c. Mismatch between the CR and superconductive blocks causes stress in the CuO_2 planes, which in the case of p-type copper oxides needs to be of compression-type. In general, the lattice stress leads to non-stoichiometry and/or structural distortions. In the case of the compression of the CuO_2 plane, it generates the mixed-valence values of the in-plane copper and/or oxygen atoms and controls the Cu-O_{api} bond length as well as the buckling of the CuO_2 plane. The Jahn-Teller type elongation of the Cu-O_{api} bond, i.e. shortening of the in-plane Cu-O bond, makes the in-plane Cu $3d_{x^2-z^2}$ orbital more favourable for the holes on the expense of the Cu $3d_{z^2}$ orbital. In each phase, the value of T_c depends crucially on the carrier concentration.

There is a strict restriction on the insertion interval of a charge reservoir (the *n*-value). With some exception in the Bi-, Tl-, and Hg-containing HTSc, most of the superconductors prepared under ambient pressure have *n*-values less than three. Using high-pressure synthesis methods, higher order phases with large n values for a variety of charge reservoirs can be stabilized. Most of the high-pressure stable series contain members whose T_c values are > 100 K.[16] In next section a short presentation of the characteristics of this synthesis method will be given.

2.2.2 High-pressure synthesis of HTSc

At the beginning of research on high-T_c superconductivity, conventional solid-state reaction under ambient pressure was the most used technique for synthesis of new materials. Later on, high-pressure synthesis became another powerful synthesis

technique of these materials. Most of the copper oxide superconductors with $T_c > 100$ K were obtained under high-pressure[i]. By means of high-pressure, a wider variety of charge reservoirs can be adjusted to the CuO_2 plane and, furthermore, a higher number of CuO_2 planes can be inserted in the structure (i.e., the insertion period of a charge reservoir becomes variable). The role of high pressure and its effect on the size mismatch between the charge reservoir and the CuO_2 plane had been the aim of many studies (see, e.g., Ref. 16).

When ionic compounds are subjected to high-pressure some of the interatomic distances, and consequently the unit cell volume, decrease. However, these distances cannot decrease below critical values at which the structure becomes unstable. Consequently, the compound either decomposes or undergoes a structural transformation. In ionic compounds, with increasing pressure, anions can decrease in size more readily than cations or, in other words, the former are more compressible than the latter.

Copper in oxide compounds can have three different valence states and, as a result, several coordination (dumbbell, square, tetrahedral, pyramidal, and octahedral) making it a good candidate to give rise to phase transformations under pressure. However, only a few pressure-induced transformations have been observed for high-T_c cuprates (e.g., orthorhombic to tetragonal phase transformation occurring in $ACuO_2$ compounds).

In-plane size mismatch between the CuO_2 plane, part of the IL block, and the charge reservoir block seems to be a key factor governing the energetic of the layered structures of high T_c superconductors. It is expected that high pressure will affect the structural stability due to different compressibility of the structural blocks. In a superconducting phase based on a charge reservoir with a small in-plane size, the charge reservoir block tends to shrink the in-plane dimensions, whereas the CuO_2 plane tends to expand them, which causes high strain energy. Due to difference in compressibility, the pressure-induced shrinkage is less pronounced in the charge reservoir than in the CuO_2 plane and the size mismatch between them tends to decrease under high pressure.

2.2.3 Role of the epitaxial strain

As an alternative method, the growth of single-crystal like thin films is increasingly used for preparation of samples with properties suitable for theoretical studies or for applications such as microelectronics. Epitaxial thin film growth gives the possibility of stabilization of metastable phases. Thin film growth can be used when these structures are less probable to be obtained by standard solid-state reaction methods or by high-

[i] High-pressure synthesis of oxide superconductors is usually conducted at pressures up to 8 GPa and temperatures up to 1400 ^oC. Piston cylinder, Bridgman anvil, belt, multi-anvil apparatus, etc. are generally used to generate such high-pressure/high-temperature conditions and among these, belt and multi-anvil devices are often used in HTSc-related synthesis research. In the high-pressure processing of the high-T_c materials, the starting mixture is usually sealed into a gold capsule that offers a completely closed environment. The oxygen pressure is controlled during processing by adding to the mixture a proper oxidizer (e.g., Ag_2O, $KClO_4$, SrO_2, BaO_2, etc.).

pressure/high-temperature synthesis. Chemical and physical deposition methods are used to prepare and study a large variety of materials of interest for today technology.

Epitaxy is the ordered growth of one crystalline layer upon a pre-existing crystalline surface.[23] The difference between different type of epitaxial growth is the supply of the source atoms: the source may be a molecular beam, gas, liquid or even an amorphous solid layer. The epitaxial growth of thin layers on crystalline substrates is possible when biaxial compressive or tensile strain in the layer accommodates the lattice mismatch between the film and substrate material.[24] In case of high-T_c copper oxide superconductors, the lattice parameters of the HTSc film and the (perovskite) substrate are, in general, different. The presence of this lattice misfit demands a relaxation. Thinner films are highly strained with the in-plane lattice spacing equal to that of the substrate. The strain energy increases with the film thickness. The strain relaxes by formation of structural defects.[25,26]

2.3 Infinite layer compounds

The ideal IL structure $ACuO_2$ (A = alkali-earth element, see Fig. 2.5) is an oxygen deficient perovskite where oxygen exists only in the conducting CuO_2 planes. The IL compounds do not have a CR block, such as a rock-salt or a fluorite like block. Due to the absence of the CR block, the IL phases have two characteristic features. First, the distance between adjacent CuO_2 planes is the shortest among all the cuprate superconductors (c ~ 3.4 Å), causing strong variations in physical properties.[16] Secondly, the charge carriers can be supplied only from the cations at the A site. Consequently, due to their rather simple crystal structure, the IL compounds have attracted much interest as a favorable system for the study of mechanism of the electron or hole doping of the CuO_2 planes in the same crystal structure. A short description of the synthesis methods and properties of hole and electron doped IL compounds will be given in next section.

2.3.1 p-type infinite layer compounds

2.3.1.1 Structural properties

At ambient pressure, the only stable IL phase found to this date is $Ca_{0.86}Sr_{0.14}CuO_2$ synthesized by standard solid-state reaction method at temperatures just below the melting point.[16] Increase in the composition range was obtained by application of high-pressure high-temperature (bulk) or by thin film synthesis methods.[27] Under a pressure of 6 GPa and at 1000 ^oC the low pressure phase (orthorhombic symmetry) transforms to a different structure (tetragonal symmetry) containing corner-sharing sheets of CuO_4 squares common to all superconducting cuprates, alternating with oxygen-depleted A layers. The coordination number of the Cu and A atoms are 4 and 8, respectively (the coordination number of A atom increases under pressure). Since the Cu valence in such compounds is 2^+ for both ambient and high-pressure phases, they were not found to be superconducting. Superconductivity appears in the CuO_2 plane after doping it with carriers (either holes or electrons) up to a certain level. Azuma *et al.*[28] were able to increase the valence of Cu cations by carring out the high-pressure high-temperature

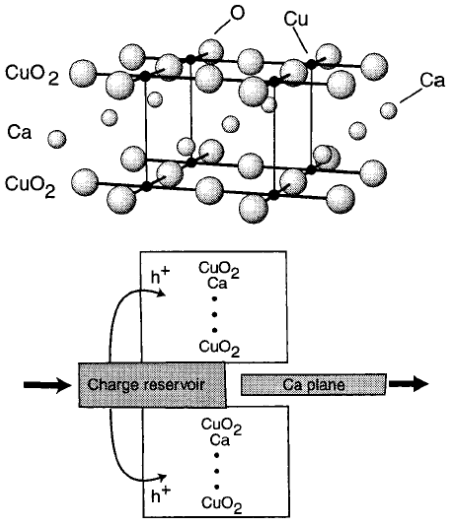

Fig. 2.5 *Crystal structure of $CaCuO_2$ infinite-layer compound and hole-doping mechanism into the CuO_2 plane (from Ref. 15).*

synthesis in the presence of $KClO_4$. The resulted product was an A-cation deficient sample, $A_{1-x}CuO_2$, which exhibits T_c as high as 100 K by doping of the conducting CuO_2 layers, achieved for $x > 0$. In other words, hole doping was achieved by inducing vacancies on A cation positions. Shaked *et al.*[29] argued that the presence of superconductivity in IL compounds should be attributed to secondary phases, belonging to the homologous series $Sr_{n+1}Cu_nO_{2n+1+\delta}$.

Another way to dope carriers into the CuO_2 plane in the IL compound is through heterovalent metal substitution for Ca/Sr. n-Type IL superconductors with electrons as carriers can be obtained by partial replacement of Ca/Sr by a trivalent metal, such as La or Nd.[14,16] This may imply that a p-type superconductor with holes as carriers can be formed by monovalent metal (such as sodium) substitution for Sr/Ca. However, attempts to produce such a material have not succeeded thus far. The possibility of the carrier doping seems to be related to the coordination number of the copper atoms. In IL compounds four coplanar oxygen atoms surround the copper atoms and an increase of the coordination number to five or six is needed for the hole doping. On the other hand, HREM measurements on p-type IL superconductors suggest that hole doping is attained by creation of randomly distributed defect layers. For example, the presence of c-axis modulation[30] or ordering of A cations, e.g., local ordering of Sr and Ba in $(Ba,Sr)CuO_2$,[31] may lead to presence of superconductivity. T_c values in range of 90-110 K were reported for the A = (Sr, Ba), Sr and (Ca, Sr)[ii] systems, all of these phases containing different types of structural defects.[33] For example, defect layers scattered along the c-axis were observed in $(Sr,Ca)CuO_2$.[34]

[ii] T_c of $(Sr_{0.7}Ca_{0.3})_{0.95}CuO_2$ reaches 120 K at 8 GPa.[32]

2.3.1.2 Bulk synthesis

As discussed before, Siegrist *et al.*[16] reported in 1988 for the first time the synthesis of an IL compound (i.e., $Ca_{0.86}Sr_{0.14}CuO_2$) with a structure consisting of CuO_2 planes separated by Ca and Sr atoms. This compound exhibits no superconductivity. Ultrahigh pressure (2-8 GPa) and high-temperature (1000 °C) reaction have been used to prepare tetragonal $SrCuO_2$ and metal-substituted $SrCuO_2$.[35] The tetragonal $SrCuO_2$ IL phase, which consists of alternating Sr^{2+} and CuO_2^{2-} layers,[36] is ideally suited for investigating high T_c superconductivity since it contains only the essential CuO_2 planes and ionic layers. Unfortunately, the ceramic products obtained from the high-pressure syntheses showed impurity phases that makes the samples not optimal for detailed physical studies that are needed to understand superconductivity in these materials. Therefore, thin film growth was used as an alternative synthesis method in order to obtain single-crystal like samples.

2.3.1.3 Thin film synthesis

Thin film processing can stabilize metastable phases that cannot be obtained by a standard solid-state reaction.[37] Thin film growth can also be used to artificially control the crystal structure. Thin films are especially attractive because they provide a well-defined surface that can be preserved from vacuum-type growth conditions and then used for different studies, such as STM;[38] they are also of interest for growth mechanism studies which reflects the systematic changes in the surface structure of the material.

Kanai *et al.*[39] have investigated the growth mechanism of $Ca_{1-x}Sr_xCuO_2$ films deposited by means of laser molecular beam epitaxy on $SrTiO_3$. A deposition pressure of 10^{-5} mbar NO_2 and substrate temperature of 600 °C was used during growth. When all the elements were simultaneously supplied, a layer-by-layer growth was achieved. One RHEED oscillation was observed during the growth of one-unit cell layers of $Ca_{1-x}Sr_xCuO_2$. They also showed that the compound could be grown by successive supply of each element under oxidation conditions (in a NO_2 atmosphere) and by monitoring of the RHEED intensity oscillation. In this case, two cycles of the RHEED intensity oscillations were observed during the growth of one unit cell of $Ca_{1-x}Sr_xCuO_2$, each cycle corresponding to separate layers of (Ca,Sr) and Cu. When Sr is deposited on $SrTiO_3$, clear RHEED intensitity oscillation could be seen and a typical streaky pattern resulted, while deposition of Cu on $SrTiO_3$ resulted in a 3D (spotty) pattern with no RHEED oscillations. These observations were explained by the fact that since SrO layer is charge neutral, stacking of SrO layers is possible, while stacking of CuO_2^{2-} layers having each a negative charge is not possible, 3D growth of neutral CuO or Cu_2O layers taking place instead. As a result, Sr and Ca layers had to be deposited prior to Cu deposition, the $Ca_{1-x}Sr_xCuO_2$ film being deposited by repetition of this process under oxidation conditions.

For each deposition method presented above, the growth of $Ca_{1-x}Sr_xCuO_2$ followed a 2D growth mechanism. Anyway, when the films were grown from the constituent elements, strict control of the composition was required otherwise the excess of Cu deposited over one atomic layer leads to 3D growth resulting in a film with a rough

surface. The films showed a solubility limit for Sr of x = 0.2; above this value, formation of impurity phases was observed.

The properties of $Ca_{1-x}Sr_xCuO_2$ thin films grown on $SrTiO_3$ by laser MBE were also studied by Koguchi *et al.*[38] The films were repeatedly annealed during and after deposition for about 10 to 20 min to enhance surface migration. The resulted surface microstructure was studied by ultrahigh-vacuum scanning tunnelling microscopy (UHV-STM) and RHEED. The films showed a 2D growth mode, the surface consisting of atomically flat and well-defined terraces separated by steps of one unit cell height. The same dependence of the growth mechanism on the Sr/Ca ratio was observed, but the films growth following a 3D growth mechanism with increasing Sr concentration.[38,39] In a related work, Feenstra *et al.*[40] observed that $SrCuO_2$ films grown by atomic layer epitaxy exhibit a natural tendency for deficiency. This is due to the formation of Sr vacancies that reduces the interfacial stress between the CuO_2 sheets and the intermediate alkaline earth metal layers.[34,40] As a result, Sr vacancies formed in the matrix of the IL compound lead to surface segregation of the expelled Sr atoms. This perturbed growth mechanism appears to have a profound impact on the doping mechanism of the films.[38]

PLD was also used to grow single-crystal like $Ca_{1-x}Sr_xCuO_2$ thin films with infinite layer structure by using single target configuration (codeposition).[41] The growth was carried out at a pressure of 0.35 mbar O_2 and substrate temperature of 700 °C. At these deposition parameters, epitaxial stabilization of this metastable phase was accomplished for the entire range of Sr (even though the composition range was large, i.e., $0.15 \leq x \leq 1.0$). The resulted films contained no impurity phases and showed semiconductor-like behaviour. The resistance values were much higher than those observed for other superconducting copper oxides.[41] This suggests that these infinite-layer films contain well-formed, but undoped, CuO_2 planes. A decrease in resistivity along with a slight contraction of the c axis was observed in some cases after post-annealing the films in oxygen for 1 h at 550 °C. This change in resistivity with oxygen post-annealing was more pronounced in films with a high Ca content.

2.3.2 n-type infinite layer compounds $Sr_{1-x}Ln_xCuO_2$

2.3.2.1 Structural properties

$Sr_{1-x}Ln_xCuO_2$ (Ln = La, Nd, Pr, Ga) compounds, in which the substitution of Ln for Sr adds electrons to the CuO_2 planes, are stable when synthesized by high-pressure high-temperature method.[14,42-45] They show superconductivity with maximum T_c of 43 K.[42-47] Substitution of Ln for Sr can reduce the CuO_2 planes without changing the oxygen content. Synthesis of the tetragonal $Sr_{1-x}Ln_xCuO_2$ compounds by high-pressure techniques takes advantage of the fact that the Sr-O bond is more compressible than the Cu-O bond. Addition of electrons into the CuO_2 sheets stretches the Cu-O bonds and increases the in-plane cell parameter a, while the replacement of the larger Sr^{2+} by a smaller Ln^{3+} ion decreases the spacing between the adjacent CuO_2 sheets and hence the lattice parameter c.

As was discussed above, the properties of the high-T_c copper oxides depend strongly on the Cu-O bond length and the oxygen coordination number of the copper atoms. In

the ideal IL structure there is only one Cu-O bond equal to one half of the lattice parameter a. Due to this simplification one can easily find an average level of doping of the CuO_2 planes with charge carriers proceeding from the structural data. Upon substitution of the small Ln^{3+} ion for the larger Sr^{2+}, the lattice constants a and c should decrease. On the other hand, substitution of the Ln^{3+} for Sr^{2+} introduces electrons into the CuO_2 layers expanding the lattice parameter a. Therefore the ratio a/c is expected to increase as compared to its value (a/c = 1.144) for undoped infinite-layer $SrCuO_2$. Also, an excess oxygen incorporated into the interstitial O(2) sites would compensate the lattice expansion along the planes and give rise to an increase of the c parameter, so that the c/a ratio becomes smaller. Podlesnyak *et al.*[42] used the ratio of the lattice parameters a/c as an empirical parameter for the existence of superconductivity in the electron doped IL $Sr_{1-x}Ln_xCuO_2$ system. They suggested that the interval $1.149 < a/c < 1.152$ would correspond to both unstable superconducting properties and a small volume fraction of the superconducting phase in the sample. Such behaviour was explained in terms of intergranular superconducting transitions. The ratio $a/c > 1.152$ was considered to correspond to the bulk superconducting properties and metal like behaviour of the normal state resistivity, not dependent on the sort of rare-earth ion.

Another way to monitor the average changes of the carrier concentration induced by doping is to calculate the bond valence sum (BVS). The changes in the BVS do not clearly reflect the level of doping as it was found for the a/c ratio.[42] This may result from the difference of the ionic radius of the doping element and from the square planar coordination in the Cu-O sheet assumed for the BVS calculation (no interstitial oxygen in the Sr(Ln) layers is taken into account). The existence of interstitial oxygen ions in the Sr layers, its influence on the superconductivity in the IL structure is not fully understood, and the reports in literature are contradictory, requiring future investigations. While there is only one oxygen position in the ideal IL structure, namely the O(1) position at the f(1/2, 0, 0) sites in the CuO_2 plane, the incorporation of excess oxygen to the O(2) interstitial b(0, 0, ½) sites is not restricted. The existence of O ions in Sr^{2+} layers compensates the extra charge of the rare-earth ion. Only a few detailed investigations have been carried out to clarify the role of the apical oxygen in electron-doped IL superconductors. From neutron diffraction studies, Jorgensen *et al.*[41] concluded that neither oxygen vacancies nor interstitial oxygen played a role in the doping of the compound. The metal and oxygen lattices were found to be perfectly stoichiometric and no excess oxygen in interstitial sites of the Sr layer was observed. Strong reduction atmosphere was required for rare-earth elements doping resulting in superconductivity in the electron-doped IL samples. The extra charge of rare-earth doping would be compensated by the oxygen ions in the Sr layers and few or no doping electrons would be generated. The reduction atmosphere is used to expel the oxygen ions from the Sr layers, and only under such conditions superconductivity arises in the electron-doped IL compounds.

For a correct analysis of the superconducting properties of the IL compounds reported in the literature special care should be paid to the preparation conditions. In particular, due to the presence of impurities as well as unknown oxygen and rare-earth contents in the IL phase, the determination of the superconducting volume fraction and the solubility limit of Ln can be ambiguous. According to electron diffraction data,

formation of a superstructure with lattice parameters $2\sqrt{2}a \times 2\sqrt{2}a \times c$ was observed for $Sr_{1-x}Nd_xCuO_2$ samples heated in vacuum (in a TEM chamber) at temperatures higher than 600 K.[48,49] The formation of the superstructure is related to the oxygen loss and is always accompanied by formation of antiphase domains. The ordering of the oxygen vacancies in the CuO_2 layers leading to the superstructure formation in the a-b plane, resulted in disappearance of superconductivity.

In the high-temperature high-pressure samples the solubility limit was found to be smaller than x = 0.15. Magnetic measurements showed that T_c onset remains constant for any doping concentration $0.05 < x \leq 0.12$, while the Meissner fraction increases with x, showing a maximum for x = 0.10. The decrease of the Meissner signal for x > 0.10 is related with the impurity phases presented in the bulk samples due to Ln solubility limit.[45] Another characteristic feature of the bulk $Sr_{1-x}Ln_xCuO_2$ phases is that the Ln content does not significantly affect the T_c values.

2.3.2.2 Bulk synthesis

The bulk synthesis of $Sr_{1-x}Ln_xCuO_2$ phases takes place at ultrahigh pressure (2.5-6 GPa) and high temperature (~ 1000 °C) reaction in a belt apparatus followed by quenching to room temperature before releasing the pressure, resulting in tetragonal $Sr_{1-x}Ln_xCuO_2$ (the orthorhombic $Sr_{1-x}Ln_xCuO_2$ phases do not contain CuO_2 planes).[44,50] Generally, "$Sr_{1-x}Ln_xCuO_2$" mixtures, as precursors for the IL phase, are synthesized mainly through three different routes:

1. a nitrate route[14] or using two conventional solid-state reaction procedures

2. from appropriate amounts of oxides CuO, Ln_xO_y and carbonates $SrCO_3$ (the mainly used method).[51] The products are, generally, mixtures of an ambient pressure phase of $SrCuO_2$, Ln_2O_3 and CuO. The main drawback of this method consist of the fact that, after high-pressure high-temperature synthesis, the samples contain dopant gradient, the solid solution $Sr_{1-x}Ln_xCuO_2$ being obtained in the central part of the samples. Due to the reductive atmosphere the surface of the samples contain monovalent copper as Cu_2O.[26]

3. from low-pressure $SrCuO_2$ phase and $NdCuO_2$,[42] as starting materials. Using this synthesis method, the conditions for yielding the IL phase are not so restricted as for the usual technology. For example, temperature and pressure gradients are less critical aspects of the method, and the preparation of large-scale samples became possible.

The "$Sr_{1-x}Ln_xCuO_2$" precursor is a multiphase mixture without any infinite-layer phase. The precursors are then reacted under high pressures (2-6 GPa) in a temperature range of 950-1050 °C for 0.5-2 h using high-pressure equipments. During synthesis at high-pressure and high-temperature $Sr_{1-x}La_xCuO_{2\pm\delta}$ compounds have to be reduced to yield superconductivity. This is achieved by removal of oxygen from Sr-plane (the apex oxygen). Due to large contribution of the grain boundaries, the polycrystalline samples are less suitable for characterization of transport properties. On the other hand, there is a possibility that the single crystals can develop a gradient of Ln concentration along the c-axis resulting in differences in reported range of doping level for which superconductivity exists.[52]

2.3.2.3 Thin film synthesis

As an alternative synthesis method, thin film growth enable the preparation of n-type IL phases by using the epitaxial stabilization effect of the substrate. Using different substrates ($SrTiO_3$, $KTaO_3$) as template layer it was shown that n-type IL can be grown using techniques such as PLD, MBE, RF sputtering etc.[43,45,51-54]

Soon after first bulk synthesis of an n-type IL compound ($Sr_{1-x}Ln_xCuO_2$, Ln = Nd, Pr),[14] Adachi *et al.*[54] reported the growth and properties of $Sr_{1-x}Nd_xCuO_2$ films with infinite-layer structure. The films were synthesized by means of RF magnetron sputtering on (001) $SrTiO_3$ in a reducing atmosphere (Ar) at substrate temperature of 550-600 °C and deposition pressure of 5×10^{-3} mbar. Cooling down was done under deposition pressure. For doping levels $x > 0.05$ the XRD data showed the presence of impurity phases ($SrCu_2O_3$, Sr_2CuO_3 and an unknown phase). For Nd content exceeding $x = 0.1$ the formation of the so-called IL-related phase characterized by a $2\sqrt{2}a \times 2\sqrt{2}a \times c$ superlattice and a c-axis parameter of c ~ 3.7 Å was observed. An a-axis value of a = 3.85-3.95 Å was estimated from RHEED patterns. For $x = 0.13$ the $Sr_{1-x}Nd_xCuO_2$ films contained the infinite-layer related phase, as single phase, and showed a metallic dependence of resistivity. The highest superconductive transition $T_{c,onset} = 16$ K was observed for $Sr_{0.88}Nd_{0.12}CuO_y$ films. The phase segregation into the infinite-layer related phase with increasing Nd concentration was considered the reason for the lower T_c value in the thin film compared to the bulk samples. Annealing the films in oxygen resulted in degradation of the superconducting properties.

Using RF-magnetron sputter deposition as well, Sugii *et al.*[43] also studied the growth and properties of $Sr_{1-x}Nd_xCuO_2$ films deposited on $SrTiO_3$. Their results showed that the infinite-layer structure formed only for $x < 0.05$ but the films were not single phase (the composition of the impurity phase was not specified - this phase is probably the infinite-related compound found also by Adachi *et al.*[54] in their study). For doping levels higher than 0.08 the films contained $(Sr,Nd)_{14}Cu_{24}O_{41}$ which become the only phase present in the films characterized by $x \geq 0.1$. The b-axis of this phase was parallel with the c-axis of $SrTiO_3$. The b-axis of $(Sr,Nd)_{14}Cu_{24}O_{41}$ phase decreases linearly with increasing Nd concentration. TEM analyses of their films showed the presence of an amorphous layer (with thickness of around 8 nm) between the substrate and the rest of the film. They considered that the amorphous interface layer formed during the TEM sample preparation due to the chemical instability of this layer. The difficulty in growing the n-type infinite layer on $SrTiO_3$ was suggested to be related to (1) the (small) in-plane cell parameters of $SrTiO_3$ which make less possible the elongation of the films a-axis and (2) to a higher phase stability of $(Sr,Nd)_{14}Cu_{24}O_{41}$, related to the energy of sputtered species and/or the oxygen activity during deposition. Therefore, $(Sr,Nd)_{14}Cu_{24}O_{41}$ phase formed preferentially for certain Nd concentration. Impurity phases such as $(Sr,Ln)_{14}Cu_{24}O_{41}$ and/or $(Sr,Ln)_{8-x}Cu_8O_{20-\delta}$ was observed also in PLD grown $Sr_{1-x}Ln_xCuO_2$ thin films.[4]

IL films on $SrTiO_3$ are epitaxially strained and have a smaller in-plane lattice constant a than the bulk values, which is considered the main reason for the inferior superconductivity of the films. Recently it was shown that T_c values as high as 39 K, close to the bulk value of 43 K, can be obtain for $Sr_{0.9}La_{0.1}CuO_2$ when grown on $KTaO_3$.[53]

In this case the CuO_2 planes are stretched and, consequently, electrons can be easily transferred to these planes.

2.4 Conclusions

Copper oxide superconductors represent a class of materials characterized by a layered structure with CuO_2 layers as a common component. The superconductivity occurs within two-dimensional copper-oxygen arrays based on the joining of CuO_4 squares at their oxygen corners to form infinite CuO_2 planes. The transition temperature from the normal to the superconductive state depends on the charge carrier (holes or electrons) concentration with the CuO_2 sheets. The role of the CR block as a source of charge carriers was shown, as well as the important role that oxygen network (concentration and position of the oxygen anions) plays in determining the final physical properties of the HTSc.

For yielding oxide superconductors with desired properties, knowledge of their structure and its relation with the final physical properties is required. A description of the charge reservoir concept and of the oxygen network characteristics of HTSc materials was given in the introduction of this chapter. A short description of the synthesis methods (high-pressure high-temperature method, a bulk technique, and thin film growth) and properties of infinite layer compounds was given next. It was shown that the control of the oxygen content is one of the requirements for tuning the valence of copper that can result in superconductivity in these oxide materials.

Since the need of very high external pressures impedes technological applications, simulating such effects by the use of internal strain in thin films offers an alternative way. The stability effect of the substrate can be used to grow metastable phases with structural characteristics similar with that of the bulk samples, but with no impurity phases, a condition required for theoretical studies on these materials. In Chapters 5 and 6 the results of PLD grown infinite layers and artificial layered structures will be presented with accent on the dependence between the deposition conditions and resulted structural and physical properties of the films. By using substrates with different in plane cell parameters (i.e., $SrTiO_3$ and $KTaO_3$) the misfit between the substrate and film was used to induce the desired p- or n-type doping. Control of the termination layer of the substrates used for this study was achieved by developing chemical and thermal treatments, the results being presented in Chapter 4.

In order to impose a layer-by-layer (2 D) growth mode a new technique, called Pulsed Laser interval Deposition (PLiD), is introduced in Chapter 3. It considers the high supersaturation rate typical for PLD. The technique allows enhanced interlayer mass transport and, consequently, formation of a multi-level growth front is avoided. In Chapter 5 and 6 the applicability of PLiD for heteroepitaxial growth of infinite layers and artificially layered structures will be demonstrated.

References

1 J.G. Bednorz and K.A. Müller, *Rev. Mod. Phys.* **60**, 585 (1988)
2 R.J. Cava, *J. Am. Ceram. Soc.* **83**, 5 (2000)
3 M.K. Wu, J.R. Ashburn, C.J. Torng, P.H. Hor, R.L. Meng, L. Gao, Z.J. Huang, Y.Q. Wang and C.W. Chu, *Phys. Rev. Lett.* **58**, 908 (1987)
4 S.K. Agarwal and A.V. Narlikar, *Progr. Crystal Growth Charact. Mater.* **28**, 219 (1994)
5 Y.D. Tretyakov and E.A. Goodilin, *Russian Chem. Rev.* **69**, 1 (2000)
6 see, e.g., H.A. Blackstead, J.D. Dow, P.J. McGinn and D.B. Pulling, *J. Supercond.: Incorporating Novel Magnetism* **13**, 977 (2000); H.A. Blackstead, J.D. Dow, P.J. McGinn and D.B. Pulling, *J. Supercond.: Incorporating Novel Magnetism* **13**, 981 (2000); J.D. Dow, H.A. Blackstead and D.R. Harshman, *Physica C* **364 - 365**, 74 (2001); J.D. Dow and D.R. Harshman, *Physica B* **312 - 313**, 53 (2002); J.D. Dow and D.R. Harshman, *J. Phys. Chem. Solids* **63**, 2309 (2002)
7 J.G. Bednorz and K.A.Z. Müller, *Z. Phys. B* **64**, 189 (1986)
8 E.T. Muromachi, Y. Matsui and K. Kosuda, *Physica C* **241**, 137 (1195)
9 M.B. Maple, *J. Magnetism and Magnetic Mater.* **177 - 181**, 18 (1998)
10 B. Raveau, C. Michel, M. Hervieu, J. Provost, F. Studer, *Earlier and Recent Aspects of Superconductivity*, J. Bednorz and K.A. Muller, Eds., Springer-Verlag, New York (1989)
11 P. Majewski, *J. Mater. Res.* **15**, 854 (2000)
12 K. Lebbou, R. Abraham, S. Trosset, J.L. Jorda and M.Th. Cohen-Adad, *Mater. Res. Bull.* **32**, 1027 (1997)
13 D. Risold, B. Hallstedt and L.J. Gauckler, *J. Am. Ceram. Soc.* **80**, 537 (1997)
14 M.G. Smith, A. Manthiram, J. Zhou, J.B. Goodenough and J.T. Markert, *Nature* **351**, 549 (1991)
15 E.T. Muromachi, *Chem. Mater.* **10**, 2686 (1998)
16 T. Siegrist, S.M. Zahurac, D.W. Murphy and R.S. Roth, *Nature* **334**, 231 (1988)
17 K. Lebbou, R. Abraham, S. Trosset, J.L. Jorda and M.Th. Cohen-Adad, *Mater. Res. Bull.* **32**, 1017 (1997)
18 L.M. Volkova, S.A. Polyshchuk and F.E. Herbeck, *J. Superconductivity: Incorporating Novel Magnetism* **13**, 583 (2000)
19 see, e.g., H. Nobumasa, K. Shimizu and T. Kawa, *Physica C* **167**, 515 (1990); K. Motida, *J. Phys. Soc. Jap.* **60**, 3194 (1991)
20 M. Marezio and J. Chenavas, *J. Solid State Chem.* **121**, 24 (1996)
21 J.–P. Locquet, J. Perret, J. Fompeyrine, E. Mächler, J.W. Seo and G. Van Tendeloo, *Nature* **394**, 453 (1998)
22 M. Karppinen and H. Yamauchi, *Mater. Sci. Eng.* **26**, 51 (1999)
23 P. Finnie and Y. Homma, *Surf. Sci.* **500**, 437 (2002)
24 A. Fischer, H. Kühne, B. Roos and H. Richter, *Semicond. Sci. Techol.* **9**, 2195 (1994)
25 A.J.H.M. Rijnders, *The initial growth of complex oxides: study and manipulation*, PhD thesis ISBN 9036516579, University of Twente, The Netherlands (2001)
26 T. Stoica and L. Vescan, *J. Cryst. Growth* **131**, 32 (1993)

27 G. Balestrino, R. Desfeux, S. Martellucci, A. Paoletti, G. Petrocelli, A. Tebano, B. Mercey and M. Hervieu, *J. Mater. Chem.* **5**, 1879 (1995)
28 M. Azuma, Z. Hiroi, M. Takano, Y. Bando and Y. Takeda, *Nature* **356**, 775 (1992)
29 H. Shaked, Y. Shimakawa, B.A. Hunter, R.L. Hitterman and J.D. Jorgensen, *Phys. Rev. B* **51**, 11784 (1995)
30 M.G. Smith, A. Manthiram, J. Zhou, J.B. Goodenough and J.T. Markert, *Nature* **351**, 549 (1991)
31 M. Takano, Y. Takeda, H. Okada, M. Miyamoto, T. Kusada, *Physica C* **159**, 375 (1989)
32 B. Wiedenhorst, H. Berg, R. Gross, B.H. Freitag and W. Mader, *Physica C* **304**, 147 (1998)
33 H. Takahashi, N. Môri, M. Azuma, Z. Hiroi and M. Takano, *Physica C* **227**, 395 (1994)
34 L.F. Mattheiss and D.R. Hamann, *Phys. Rev. B* **40**, 2217 (1989)
35 Z. Hiroi, M. Takano, M. Azuma and Y. Takeda, Nature **364**, 315 (1993)
36 Z. Hiroi, M. Takano, M. Azuma, Y. Takeda and Y. Bando, *Physica C* **185 - 189**, 523 (1991)
37 E.C. Jones, D.P. Norton, D.K. Christen and D.H. Lowndes, *Phys. Rev. Lett.* **73**, 166 (1994)
38 K. Koguchi, T. Matsumoto and T. Kawai, *Science* **267**, 71 (1995)
39 M. Kanai, T. Kawai and S. Kawai, *Appl. Phys. Lett.* **58**, 771 (1991)
40 R. Feenstra, X. Li, M. Kanai, T. Kawai, S. Kawai, J.D. Budai, E.C. Jones, Y.R. Sun, J.R. Thompson, S.J. Pennycook and D.K. Christen, *Physica C* **224**, 300 (1994)
41 J.D. Jorgensen, P.G. Radaelli, D.G. Hinks, J.L. Wagner, S. Kikkawa, G. Er and F. Kanamaru, *Phys. Rev. B* **47**, 14654 (1993)
42 A. Podlesnyak, A. Mirmelstein, V. Bobrovskii, V. Voronin, A. Karkin, I. Zhdakhin, B. Goshchitskii, E. Midberg, V. Zubkov, T. D'yachkova, E. Khlybov, J.-Y. Genoud, S. Rosenkranz, F. Fauth, W. Henggeler and A. Furrer, *Physica C* **258**, 159 (1996)
43 N. Sugii, M. Ichikawa, K. Kubo, T. Sakurai, K. Yamamoto and H. Yamauchi, *Physica C* **196**, 129 (1992)
44 N. Sugii, K. Matsuura, K. Kubo, K. Yamamoto, M. Ichikawa and H. Yamauchi, *J. Appl. Phys.* **74**, 4047 (1993)
45 N. Ikeda, Z. Hiroi, M. Azuma, M. Takano, Y. Bando and Y. Takeda, *Physica C* **210**, 367 (1993)
46 M.S. Kim, C.U. Jung, J.Y. Kim, J.-H. Choi and S.-I. Lee, *Solid State Commun.* **123**, 17 (2002)
47 N.-C. Yeh, C.-T, Chen, C.-C. Fu, P. Seneor, Z. Huang, C.U. Jung, J.Y. Kim, M.-S. Park, H.-J. Kim, S.-I. Lee, K. Yoshida, S. Tajima, G. Hammerl and J. Mannhart, *Physica C* **367**, 174 (2002)
48 Y.G. Peng, F.H. Li, X.J. Zhou and Y.S. Yao, *Physica C* **230**, 318 (1994)
49 Z.X. Zhao, X.J. Zhou, J.Q. Li and Y.S. Yao, *Physica C* **229**, 35 (1994)
50 X.-Y. Zheng, D.H. Lowndes, S. Zhu, J.D. Budai and R.J. Warmack, *Phys. Rev. B* **45**, 7584 (1992)
51 G. Er, S. Kikkawa, F. Kanamaru, Y. Miyamoto, S. Tanaka, M. Sera, M. Sato, Z. Hiroi, M. Takano and Y. Bando, *Physica C* **196**, 271 (1992)

52 E. Maiser, P. Fournier, J.-L. Peng, F.K. Araujo-Moreira, T. Venkatesan, R.L. Greene and G. Czjzek, *Physica C* **297**, 15 (1998)
53 S. Karimoto, K. Ueda, M. Naito and T. Imai, *Appl. Phys. Lett.* **79**, 2767 (2001)
54 H. Adachi, T. Satoh, Y. Ichikawa, K. Setsune and K. Wasa, Physica C **196**, 14 (1992)

Chapter 3

Technology and analysis

3.1 Introduction

Since its first application[1] in 1965, pulsed laser deposition (PLD) have demonstrated its flexibility with respect to the realization of novel, complex materials. PLD is used very efficiently for growth of metastable phases and artificial structures difficult or impossible to be stabilized by means of conventional synthesis methods. Furthermore, PLD permits the evaporation of both conducting and insulating materials and, therefore, the use of metallic and composite targets.[2] An advantage of PLD is the possibility to change, *in situ*, the deposited material, thus enabling the development of new structures. The structure of the film does not necessary correspond to that of the bulk material with the same composition, as will be shown in next chapters for infinite layer compounds.

One of the most used techniques for *in-situ* analysis of the surface structure during thin film growth is reflection high-energy electron diffraction (RHEED). By monitoring the evolution of the RHEED intensity during film deposition, one can control the evolution of the growth front and, consequently, the structural properties (e.g., surface morphology, crystal structure) of the film. In this chapter a PLD system equipped with high pressure RHEED will be described. Basic principles of both PLD and RHEED will be discussed. Finally, thin film analyses methods, such as Atomic Force Microscopy (AFM), X-Ray Diffraction (XRD), and High Resolution Electron Microscopy (HREM), will be shortly addressed.

3.2 Pulsed laser deposition (PLD)

3.2.1 Basic principles of PLD

PLD uses a highly energetic pulsed laser beam in order to ablate material from a target and transfer it to a substrate. When the beam hits the target a dense layer of vapor results in front of the target. After this early stage the pressure and the temperature of the vapor increases due to energy absorption from the laser beam during the remainder of the laser shot, with partial ionization of the vapor particles. Due to the resulting high pressure the layer expands from the target surface and forms the so-called 'plasma plume'. The kinetic energy of the ablated particles can vary from high initial energy, in vacuum, to low energies resulting from thermalization at (relatively high) deposition pressures. Under background pressure the kinetic energy of the particles arriving at the substrate is attenuated due to multiple collisions taking place during plasma expansion. At deposition pressures characteristic for deposition of complex oxides, thermalization occurs at a penetration length comparable to the target-substrate distance. The surface diffusivity and absorption/desorption probability of the adatoms arriving at the substrate or film surface can be controlled by kinetic energy of the arrival particles. In this way, the growth can be manipulated.

One of the unique features of PLD is the high deposition rate[i] that can be reached (e.g., 10^2-10^5 nm/s),[3-6] orders of magnitude higher than other physical vapor deposition techniques (e.g., MBE, sputter deposition). This extremely high deposition rate leads to a high degree of supersaturation. For a wide range of deposition conditions the time scale for the atomistic processes taking place at the growth front (e.g., collision and nucleation) exceeds that of the pulse duration. Therefore, deposition can be regarded as instantaneous for each laser pulse.[3] A relatively long time interval, determined by the pulse repetition rate, exists after each laser shot. During this interval, the adatoms rearrange on the surface by migration and subsequent incorporation through nucleation and growth.[3] These two processes, i.e., random deposition and growth are separated in time, another unique feature for PLD. This separation is also useful in studies of growth kinetics.[3]

The supersaturation determines the nucleation mechanism of the ablated particles arriving at the growth front.[7] Due to the high supersaturation, a high density of nuclei is expected, with very small nucleus size (i.e., of the order of one unit-cell). In the time interval between the laser shots, the unstable nuclei (clusters) dissociate into mobile atoms that can nucleate in new clusters or attach to the existing stable clusters. This process, where larger clusters grow at the expense of small ones, is considered similar to Oswald ripening.[3,6]

[i] The parameters that determine the deposition rate are the laser pulse energy and energy density at the target, substrate-target distance, mass and pressure of the ambient gas.

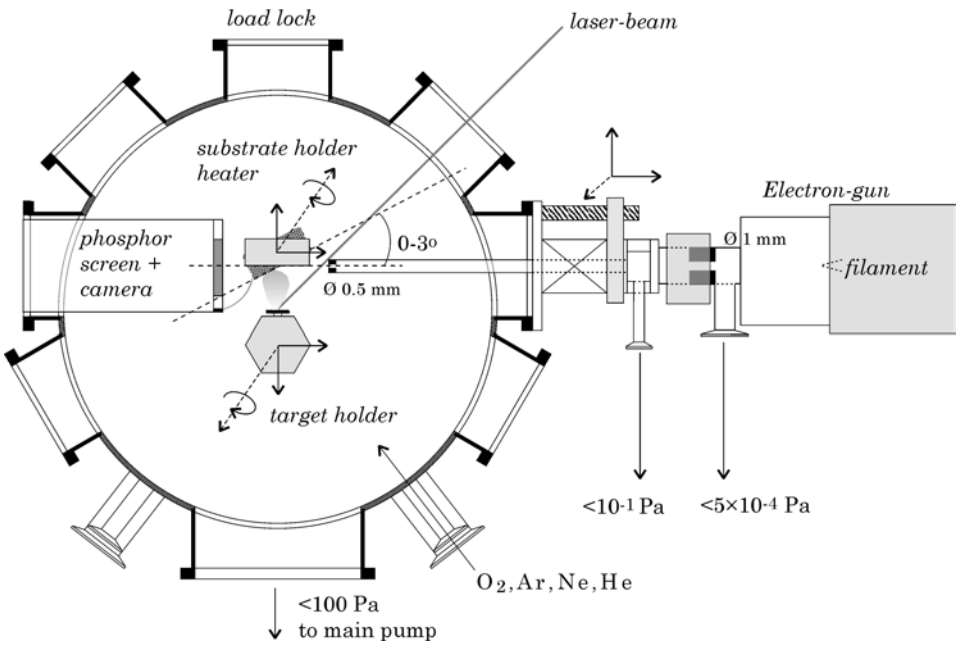

Fig. 3.1 *Schematic view of the PLD system, including the electron source assembly.*

3.3.2 PLD set-up

A schematic view of the deposition chamber,[3,6] including the electron source assembly, is given in Fig. 3.1. A KrF excimer laser ($\lambda = 248$ nm) is used for ablation of the target material. The laser beam is focused under 45° incidence onto the target using a lens with a focal length of ~ 500 nm. The multi-target holder and the substrate holder can be inserted inside the deposition chamber via a load-lock system without breaking the vacuum. The targets are mounted on a computer controlled XYZ-rotation target holder, which can hold up to 5 targets. The targets are either stoichiometric sintered pellets (e.g., $SrCuO_2$, $CaCuO_2$, $BaCuO_2$, $Sr_{1-x}La_xCuO_2$) or single crystals (e.g., $BaTiO_3$, SrO, BaO). During deposition the targets are scanned horizontally in the laser beam. Selection of the targets, laser repetition rate and the number of pulses for each target is fully automated.

For deposition the substrates are mounted on a thermo-coax heater using silver paste allowing for good thermal contacts. The temperature is measured inside the heater block with a K-type thermocouple and temperatures up to 950 °C can be attained. The pressure inside the deposition chamber is controlled by means of two mass flow controllers (Brooks Instruments, 0-40 ml/min) in combination with a pump restriction.[3,6] The aperture of the restriction and the gas flow settings determine the final pressure. For high pressure annealing (e.g., higher than 10 mbar), the valves to the pumps are closed and the chamber is flooded with either oxygen or nitrogen.

3.3.3 Pulsed laser interval deposition (PLiD)

By pulsed laser interval deposition (PLiD) one monolayer (e.g., one atomic or one unit layer) is deposited in a very short time interval, smaller or equal to the characteristic relaxation times[ii], followed by a much longer interval during which the deposited material can rearrange.[8-11] During the short deposition period, only small islands will be formed due to the high supersaturation. By PLiD a high interlayer mass transport is promoted which insures monolayer growth. In order to minimize the error introduced by the fact that only an integer number of pulses can be given the total amount of pulses has to be as high as possible[iii].[8] Both a high deposition rate and sufficiently accurate deposition rate can be obtained by PLD. The interval deposition was used with success to impose a layer-by-layer growth for $SrTiO_3$,[8-11] as well as for heteroepitaxial growth of infinite layer superlattices on $SrTiO_3$.[12] In chapters 5 and 6 the PLiD growth and properties of infinite layer compounds and artificially layered structures on $NdGaO_3$ substrates will be discussed.

3.3 Reflection high-energy electron diffraction (RHEED)

3.3.1 Basic principles of RHEED

RHEED provides information about the periodic arrangement of the surface atoms and, therefore, it is often used for the investigation of the surface structure and morphology during thin film growth. It gives a statistical view of disorder rather than a local picture. The mono-energetic electrons used in RHEED have a wavelength λ[iv] that is an order of magnitude smaller than the thickness of an atomic layer. The electrons are scattered from a crystal surface resulting in a diffraction pattern characteristic for the analysed surface. By using a low incidence angle (1-5°) for the electron beam, a penetration depth of few atomic layers results at these grazing angles. This makes RHEED a surface sensitive diffraction technique useful for investigating the crystallography and microstructure of surfaces, as well as for studies on growth mechanisms. The coherence length, determined by the beam convergence and the energy spread of the electrons, is typically of the order of few hundred nm.

An analysis of the intensity distribution along the (00) and/or its neighbouring diffracted dots or streaks (see Fig. 3.2) is used to obtain information about the surface roughness. The RHEED pattern from a perfectly flat surface consists of sharp spots aligned on arcs called Laue circles. For a surface with domains, e.g., terraces, grains, etc., the spots on the arcs are elongated into streaks perpendicular to the shadow edge. This is explained in terms of broadening of the reciprocal rods, i.e., the cross-sections

---

[ii] The characteristic relaxation time is related to the mean diffusion time of the material.

[iii] This is limited by the pulse repetition rate and the characteristic relaxation time.

[iv] The energy of the electrons used for RHEED is of ~ 10-50 keV,[1,3] which means that λ is ~ 0.05-0.1 Å [$\lambda(\text{Å}) = \sqrt{\frac{150}{E}}$]

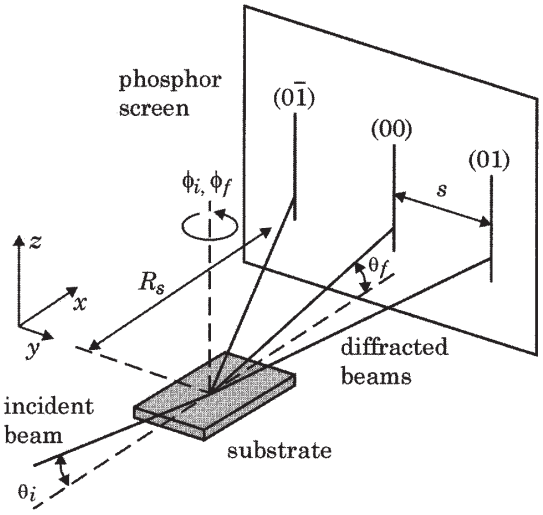

Fig. 3.2 *Schematic view of the RHEED geometry. θ_i (θ_f) and ϕ_i (ϕ_f) are the incident and azimuthal angles of the incident (diffracted) beam. R_S is the distance between substrate and phosphor screen and S the distance between the diffraction spots or streaks.*

between the reciprocal rods and the Ewald sphere[v] become longer. In case of a rough surface, the e-beam can penetrate through surface islands.[13] In this case, the electrons produce 3D Bragg diffraction and a spotty RHEED pattern that looks like an image from a transmission electron microscope. The variation of the RHEED intensity along the streaks is related to the step density of the surface and can be used to study basic processes during growth.

As a surface sensitive technique, RHEED can be used for study of the basic processes and mechanisms in the epitaxial growth of complex oxides. Understanding of these processes will permit manipulation of growth conditions in order to control film properties, such as interface properties, surface roughness, and phase stability.

Precisely defined growth conditions, the knowledge of mechanisms governing the evolution of the growth front helps to tailor film's morphology to obtain desired properties. Growth of thin films from atoms deposited from the gas phase is intrinsically a non-equilibrium phenomenon governed by a competition between kinetics and thermodynamics. Precise control of the growth and thus of the properties of deposited films becomes possible only after an understanding of this competition is achieved. The most important kinetic mechanisms of film growth include adatom diffusion on terraces,

---

[v] The Ewald sphere is defined[3,14] by the sphere around the origin of $\mathbf{k_0}$ with radius $|\mathbf{k_0}|$ (equals $2\pi/\lambda$ for elastic scaterring), where $\mathbf{k_0}$ represents the wave vector of the incident beam. The superpositioning of the Ewald sphere onto the reciprocal lattice shows the conservation of momentum as well as the energy in the form of the Laue conditions, $\mathbf{S} = \mathbf{G_{hkl}}$; $\mathbf{G_{hkl}}$ represents the reciprocal-lattice vectors, $|\mathbf{G_{hkl}}| = n2\pi/d_{hkl}$, and d_{hkl} is the distance between the (hkl) planes.

along steps, and around island corners, nucleation and dynamics of the stable nucleus, atom attachment to and detachment from terraces and islands, and interlayer mass transport.

3.3.2 High-pressure RHEED set-up

The pressure in a RHEED set-up has to be sufficiently low to avoid electron scattering by the ambient gas. Attenuation of the e-beam intensity is expected at high ambient pressure due to elastic and inelastic electron scattering. Furthermore, a low pressure is required near the filament of the electron gun (e-gun), to avoid decreasing the filament lifetime. To increase the operating pressure in RHEED to the relatively high deposition pressure used in PLD of oxides a low pressure in the e-gun should be maintained and the attenuation of the e-beam intensity[vi] has to be minimized.[3,15,16] The travelling distance of the e-beam has to be reduced to minimize electron scattering losses at the relatively high pressures used in PLD.

To satisfy the requirements of low pressure in the e-gun and short travelling distance at high pressure, a two-stage, differentially pumped RHEED system[3,6,17] has been used for the experiments that will be discussed in this thesis. A schematic view of this high-pressure RHEED system is depicted in Fig. 3.1. The e-gun (EK-2035-R, STAIB Instruments) has a minimum beam size of ~ 250 μm (FWHM) at the working distance of 500 mm. It is mounted on a flange connected to a stainless steel extension tube with an inner diameter of 8 mm. A differential pumping unit is used to maintain a vacuum of better than 10^{-6} mbar in the e-gun. An aperture (diameter 0.5 mm) separates the tube from the deposition chamber. The pressure in the tube, which depends on the pump speed and the size of the aperture, is kept below 10^{-3} mbar. Using this two stage pumping system the pressure in the deposition chamber can be increased up to 1 mbar, maintaining the low pressure in the electron source. The e-beam, which passes through the apertures inside the differential pumping unit and the tube, enters the deposition chamber near the substrate at a distance of 50 mm. The XY deflection capability of the electron source is used to direct the e-beam through the aperture at the end of the tube.

The fluorescent phosphor screen, with a diameter of 50 mm, is mounted on a flange located near the substrate. The distance between the screen and the substrate is 50 mm. The screen is shielded from the laser plasma to minimize deposition on the screen. The electron source, including the extension tube, is mounted on a XYZ-stage allowing adjustment of the distance between substrate and the end of the tube. The e-beam is shielded from magnetic fields (e.g., earth magnetic field) using μ-metal.

Using the extension tube, the travelling distance in the high-pressure regime is reduced to 100 mm. Intensity losses due to electron scattering inside the extension tube are negligible since the pressure is kept below 10^{-3} mbar. In the high-pressure regime, adjusting the e-beam current can be used to compensate the decrease in the RHEED intensity due to the scattering losses. The azimuthal and the incidence angles of the e-

[vi] The attenuation of the e-beam intensity is expressed as $I/I_o = exp(-l/L_E)$ where l is the distance of the travelling path of the electrons, L_E is the mean free path of the electrons, and Io is the intensity of the e-beam for $l << L_E$.

beam on the substrate can be adjusted by rotating the substrate holder. The substrate holder can be rotated and moved back and forward in order to adjust the azimuth and incidence angles for RHEED measurements. The intensity oscillations of the specular spot are monitored during growth with a Peltier cooled CCD camera (connected to a computer). The RHEED patterns can be recorded with KSA acquisition software (K-Space Associates).

3.4 Analysis tools

AFM was used for surface morphology study, while XRD and HREM were used for crystalline structure analyses. These techniques are briefly addressed in next sections.

3.4.1 Atomic force microscopy

A Nanoscope III instrument (DI, Santa Barbara, CA) was used for AFM experiments, in contact or tapping mode imaging. Lateral or frictional forces were measured simultaneously (by the four-quadrant detector). Standard Si_3N_4 triangular contact mode tips ($k = 0.58$ Nm^{-1}) and sharper rectangular tapping mode tips ($k = 20$-100 Nm^{-1}) were used with the total interaction force kept as low as possible (estimated to be < 10 nN). Lateral Force Microscopy (LFM) has been use to determine the presence of different termination(s) on the surface.[18]

Due to the experimental conditions (variation in the alignment of the laser on the cantilever and of the humidity in the laboratory) the exact lateral force constant of the cantilevers are unknown. Imaging took place after the substrates were treated (chemically or thermally) while the films were analyzed after they were removed from the processing chamber. This insures that surface contamination, that would affect the quality of the image, is minimized.

3.4.2 X-ray diffraction

X-ray diffraction (θ-2θ, Mathieson, ω-2θ, and ϕ scans) in the normal Bragg-reflection geometry was performed on a four-circle single-crystall difractometer (CAD4, Enraf Nonius Delft, The Netherlands), using Cu Kα radiation. The lattice parameters of the films (including the in plane cell parameters) were calculated from XRD data employing 18-25 reflections by a least square fitting technique. The orientation matrix of the substrate crystal was determined by performing scans along the direction perpendicular to the substrate surface. The miscut angle of the substrates was determined with the aid of a diode laser aimed at the surface acting as a small mirror and φ rotation around the (00l) axis. Since all the films were expected to be epitaxialy grown, the θ-2θ scans were performed around the (00l) direction of the substrate. Low-angle reflectivity measurements were performed as well in order to determine the film's thickness.

The instrumental broadening was estimated[6] from the substrate peaks to be 0.2°. The θ-2θ scans showed additional peaks corresponding to spectral λ/2 and λ/3 lines transmitted by the strong (00l) reflection of the substrates.

3.4.3 High-resolution electron microscopy (HREM)

HREM combined with electron diffraction (ED) allows obtaining information of the crystal structure and symmetry. The resolution is limited by the image transfer function, determined by the instrumental parameters such as spherical aberration, defocus spread and beam divergence, the focus of the objective lens and the acceleration voltage.[19]

A JEOL 4000EX operating at 400 kV and 376 kV was used for the HREM analyses. The instrument has a point-to-point resolution of 0.17 nm. Plan view imaging, which allows studying the microstructure in the plane parallel to the substrate surface, and cross-section imaging which allows to study the film/substrate interface region and the microstructure as function of the film thickness were performed. The specimens preparations requires a mechanical polishing of the samples down to a thickness of 30 μm (plan view preparation) or 10 μm (cross-section preparation), followed by ion-milling to reach electron transparency.[19] From all the studied samples, the films of (Ba,Sr,Ca)CuO_2 artificially layered structures suffered considerably from amorphisation and, therefore, HREM measurements were not possible.

3.5 Conclusions

A short description of PLD, the deposition technique used for the experiments described in this thesis, and of RHEED, AFM, XRD and HREM, as analysis tools, is given in this chapter. PLD can be distinguished from other thin film deposition techniques by the tunable high energy of particles arriving at the substrate of film surface, the high deposition rate, both dependent on the gas pressure, and the pulsed way of deposition. At a certain background pressure, most of the energy of the plasma plume species is dispersed in the background gas through collisions with cold gas molecules. The velocity of the particles arriving at the substrate is a function of gas pressure and, therefore, a strong influence of the pressure is expected on the growth behavior. Given the interaction of the plasma particles with the substrate material, the high supersaturation, characteristic for PLD, determines the nucleation mechanism of the arriving particles. The combination of substrate temperature, gas pressure, and the stabilizing effect of the substrate determine the phase of the film material.

The combination of PLD with *in situ* monitoring of the growth front with RHEED enables accurate control of the growth. For relatively high deposition pressures required for stability of complex oxides, a two-stage differentially pumped RHEED system is used for the experiments. Its applicability in inducing a layer-by-layer growth mode will be demonstrated in chapters 5 and 6 for hole and electron doped infinite layer compounds, as well as for artificially layered structures.

References

1 H.M. Smith and A.F. Turner, *Appl. Opt.* **4**, 147 (1965)
2 J.F. Hamet and B. Mercey, *Current Opinion in Solid State and Material Science* **3**, 144 (1998)
3 A.J.H.M. Rijnders, *The initial growth of complex oxides: study and manipulation*, PhD thesis ISBN 9036516579, University of Twente, The Netherlands (2001)
4 M.Y. Chern, A. Gupta and B.W. Hussey, *Appl. Phys. Lett.* **60**, 3045 (1992)
5 D.B. Geohegan and A.A. Puretzky, *Appl. Phys. Lett.* **67**, 197 (1995)
6 G. Koster, *Artificially layered oxides by pulsed laser deposition*, PhD thesis ISBN 9036513367, University of Twente, The Netherlands (1999)
7 I.V. Markov, *Crystal growth for beginners*, chapter I (World Scientific, 1994)
8 G. Koster, A.J.H.M. Rijnders, D.H.A. Blank and H. Rogall, *Appl. Phys. Lett.* **74**, 3729 (1999)
9 D.H.A. Blank, G. Koster, G. Rijnders, E. van Setten, P. Slycke and H. Rogalla, *Appl. Phys. A* **69**, S17 (1999)
10 D.H.A. Blank, G. Koster, A.J.H.M. Rijnders, E. van Setten, P. Slycke and H. Rogalla, *J. Crystal Growth* **211**, 98 (2000)
11 G. Rijnders, G. Koster, V. Leca, D.H.A. Blank and H. Rogalla, *Appl. Surf. Sci.* **168**, 223 (2000)
12 G. Koster, K. Verbist, G. Rijnders, H. Rogalla, G. van Tendeloo and D.H.A. Blank, *Physica C* **353**, 167 (2001)
13 K. Mae, V.V. Moshchalkov and Y. Bruynseraede, *Thin Solid Films* **340**, 145 (1999)
14 M.G. Lagally, D.E. Savage and M.C. Tringides, in *Reflection high energy electron diffraction and refelection electron imaging of surfaces*, P.K. Larsen and P.J. Dobson Eds. (Plenum Press, London, 1989), pp. 139-174
15 G. Garcia, M. Roteta and F. Manero, *Chem. Phys. Lett.* **264**, 589 (1997)
16 G. Garcia, F. Blanco and A. Williart, *Chem. Phys. Lett.* **335**, 227 (2001)
17 A.J.H.M. Rijnders, G. Koster, D.H.A. Blank and H. Rogalla, *Appl. Phys. Lett.* **70**, 1888 (1997)
18 J. Fompeyrine, R. Berger, H.P. Lang, J. Perret, E. Mächler, Ch. Gerber, and J.-P. Locquet, *Appl. Phys. Lett.* **72**, 1697 (1998)
19 K. Verbist, *Microstructure of high-T_c superconducting thin films and junctions*, PhD thesis, University of Antwerpen, Belgium (1996)

Chapter 4

Substrate surface morphology

4.1 Introduction

Substrates with perovskite (ABO_3) or related layered structures are often used as template for epitaxial growth of HTSc films due to the similarities in their crystal structure. Control of the substrate surface morphology, the chemistry of terminating layer, as well as knowledge of its vicinal angle[i] are important for better control the film's growth mode. When growing films of compounds with layered structure, such as HTSc,[1,2] the composition of the substrate terminating layer(s) can determine the surface morphology of the film,[3,4] as well as the stacking sequence,[2-5] as was shown for, e.g., $YBa_2Cu_3O_{7-\delta}$ on $SrTiO_3$.[5] Therefore, a single terminated surface is required for reproducible thin film growth with respect to morphology and epitaxy, while substrate-film interface properties can determine the physical properties of the film.[1-4,6,7]

In this chapter, chemical and thermal methods developed for better control of the substrate surface morphology (i.e., crystallinity and composition) will be presented and discussed. For this study, several substrates with layered structure (i.e., perovskite, $GdFeO_3$, and K_2NiF_4 type) were selected. The selection was made by considering their chemical compatibility and lattice match with those of the films (e.g., the infinite layer compounds and the artificially layered structures) of interest here. The substrates under investigation[8] were $SrTiO_3$, $NdGaO_3$, LSAT, $SrLaAlO_4$, and $KTaO_3$, all (001) oriented, except for $NdGaO_3$, for which both (001) and (110) orientations were used. They have a structure consisting of alternating layers of $AO_{1+\delta}$ (A = Sr, La, Nd or K) and $BO_{2-\delta}$ (B = Ti, Al, Ta or Ga) stacked in the c direction. The chemical treatments presented in this chapter were based on the methods developed for $SrTiO_3$.[9-12] New

[i] The vicinal angle (or miscut angle) of a substrate represents the angle made by crystallographic axis with the direction of cutting plane (see Fig. 4.1).

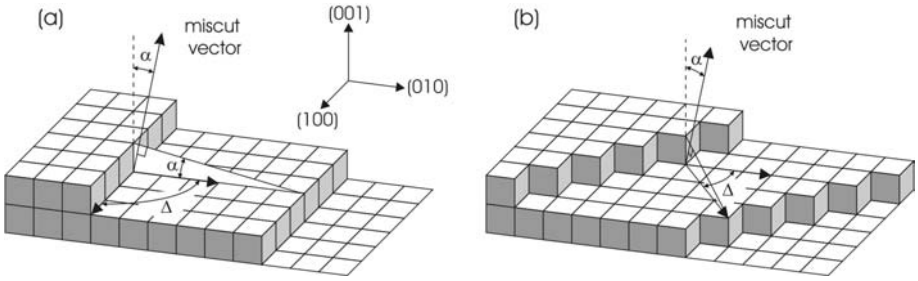

Fig. 4.1 *(a) Schematic representation of vicinal angle, α, toward (010) crystalographic direction, i.e., Δ = 90°. (b) Substrate with vicinal angle towards (110) crystallographic direction, i.e., Δ = f °.*

chemical solutions, adapted to the surface chemistry and substrate vicinal angle, were developed in order to produce an atomically smooth, single terminated surface.

The chapter contains a short description of the structural and physical properties of the oxides used as substrates in this thesis, followed by a presentation of the surface preparation methods described in literature. The experimental sections of the chapter will treat the results of the chemical and thermal treatments applied in order to yield atomically flat surfaces, with, preferably, either $AO_{1+\delta}$ or $BO_{2-\delta}$ as topmost layer. The substrates surface morphology after chemical and/or physical processes was studied using AFM and *in situ* high-pressure RHEED. The results will be presented and discussed for each substrate under investigation.

4.2 General properties

In this section, an overview of the structural and physical properties of the oxides used as substrates in this study will be given. In order, data on the following single crystal substrates will be presented: (110) and (001) $NdGaO_3$, (001) $SrTiO_3$, (001) LSAT, (001) $SrLaAlO_4$, and (001) $KTaO_3$. Some of the methods that can be generally applied in order to improve the surface morphology of these substrates will be presented at the end of this section.

4.2.1 (110) and (001) $NdGaO_3$

X-ray and neutron diffraction data showed that $NdGaO_3$ has, at room temperature, a $GdFeO_3$ type structure (see Fig 4.2). The structural and physical properties of this oxide are given in Table 4.1. While (001) $NdGaO_3$ has an orthorhombic symmetry, (110) $NdGaO_3$ has a perovskite-type crystal structure that is slightly distorted in comparison with the primitive perovskite structure. Therefore, the crystal structure of (110) $NdGaO_3$ is rather orthorhombic than cubic. Among the lanthanide gallates, it is the only oxide with no structural phase transitions below ~ 900 °C. Therefore, it can be used to grown twin free thin films.[13] Low rf loss of $NdGaO_3$ makes this substrate more suitable for microwave applications than, e.g., $SrTiO_3$. $NdGaO_3$ single crystals can be

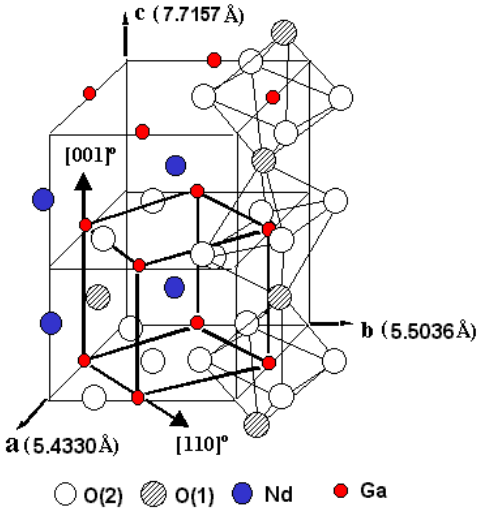

Fig. 4.2 *Schematic representation of the pseudocubic (110) $NdGaO_3$ structure constructed inside the orthorhombic (001) structure showing the tilting of the octahedral about the* b *and* c *axes.*

used as substrate for epitaxial growth of high T_c superconductors (HTSc),[14-17] infinite layer phases,[18] or other compounds (e.g., GaN, Sr_2RuO_4).[19-22]

Regarding surface treatments, Ohnishi *et al.*[23] have shown that an A-site (i.e., NdO_{1+x}) single terminated (001) $NdGaO_3$ surface can be obtained after 2h annealing in air at high temperature (1000 °C), as demonstrated by coaxial impact-collision ion scattering spectroscopy (CAICISS) measurements (see Table 4.2). There are no reports of studies on the effect of chemical etching on the surface morphology of $NdGaO_3$ substrates. Different solutions (e.g., HCl, HNO_3) have been used in order to remove the surface contaminants, but no details on the influence of this process on the surface properties were given.[24]

4.2.2 (001) $SrTiO_3$

$SrTiO_3$ is a dielectric material with a perovskite structure. The structural and physical properties of this oxide are given in Table 4.1. It undergoes a second-order phase transition (from cubic to tetragonal symmetry) at a temperature of ~ 108 K. This phase transition is induced by rotation of neighbouring TiO_6 octahedra in opposite directions.[25] The unit cell of $SrTiO_3$ is shown in Fig. 4.3a. Ti ions are at the cube corners, Sr ion in the centre of the cube, and O ions on the cube edges. In the (001) direction, the crystal is made up from a stack of alternating TiO_2 and SrO layers (see Fig. 4.3b). Therefore, two charge neutral (001) terminations are possible: SrO and TiO_2 surfaces. According to chemical potential calculations,[26] both surfaces have comparable thermodynamic stability, while a preference towards a TiO_2 termination is predicted by surface energy calculations.[27] As a result, a (001) surface of a $SrTiO_3$ crystal may

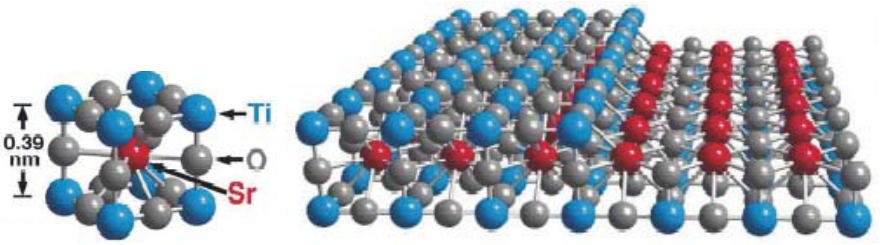

(a) *(b)*

Fig. 4.3 *(a) Schematic representation of the $SrTiO_3$ unit cell. Ti ions are located at the cube corners, Sr ion in the center of the cube, and O ions on the cube edges. (b) (001) surface with the two possible (1×1) terminations (TiO_2 on left, SrO on right) (from Ref. 5).*

display both types of terminations. $SrTiO_3$ is often used as substrate material for HTSc thin film because of compatible crystal structure and good lattice matching.

Different treatments have been developed aiming at improving the surface morphology of this substrate. The main techniques used were wet etching with a HF + NH_4F (ammonia buffered HF or BHF) solution, annealing in O_2, Ar^+ sputtering, Bi deposition/desorption.[9-12, 28-30] From these methods, etching and annealing are used with success in controlling the chemistry of the terminating layer (see Table 4.2) and for yielding atomically flat surfaces. BHF etching method considers the difference in reactivity of the component oxides (i.e., SrO is a basic oxide, while TiO_2 is an acidic oxide).[9] In the first step a Sr-hydroxide complex is formed by soaking the substrate in water. The hydroxide is then removed with a BHF solution (pH ~ 4.5). In order to facilitate recystallization, a final annealing step is performed at 950 °C in O_2 flow, typically for 1h. The result of this treatment in an atomically smooth TiO_2-single terminated surface.[9-12] A detailed description of the etching procedure can be found in Ref. 11.

For Bi cleaned (100) $SrTiO_3$, the low-energy electron diffraction (LEED) measurement showed a sharp (1×1) pattern, while the CAICISS data showed a mixed termination surface, consisting of at least 75 % TiO_2 and SrO for the rest.[30] The method results in minimal damage to the structure of the surface and does not require high temperature annealing[ii] of the substrate. A similar mixed termination surface results for Ar^+ sputtered $SrTiO_3$, followed by annealing for surface reconstruction. RHEED pattern after this treatment exhibits a clear (1×1) pattern.[31]

High-temperature (900-1000 °C) annealing of the as-received substrates results in re-growth of the surface.[12] The combination of miscut angle, the duration and the temperature of annealing determine the morphology of the surface. After an optimum annealing treatment, an A-site terminated surface is considered to result.[9-12]

[ii] A temperature of ~ 500 °C is used in the Bi deposition/desorption cleaning method.[31]

4.2.3 (001) LSAT

LSAT represents the $Sr_{1-x}La_xAl_{1-y}Ta_yO_3$ solid solution, with typical values for x and y of x = 0.3 and y = 0.35, respectively (i.e., $(LaAlO_3)_{0.3}(Sr_2AlTaO_6)_{0.35}$ formula). The structural and physical properties of LSAT are given in Table 4.1. It has a perovskite structure for temperatures above 150 K.[32,33] There are few reports on surface treatment of LSAT, probably due to difficulty of yielding an A- or B-site single terminated surface for this solid solution compound. The main technique used is annealing at 1300 °C in air for 2 h which resulted in a composition of ~90% $AlO_{2-\delta}/TaO_{2-\delta}$ for the topmost layer (Table 4.2).[23]

4.2.4 (001) $SrLaAlO_4$

$SrLaAlO_4$ has a tetragonal K_2NiF_4 layered structure (Table 4.1). The lattice constants of this compound can be tuned through formation of $SrLaAl_{1-x}Ga_xO_4$ solid solutions.[34] The main units of the $SrLaAlO_4$ structure are the slightly distorted AlO_6 octahedra that form a two-dimensional net of corner-shared oxygen. The apex oxygen and Sr/La ions (distributed in nine-coordinated sites) form slabs with a rock salt structure and they are situated between the AlO_6 layers.

$SrLaAlO_4$ is used as substrate material for growth of high-T_c thin films, in particular for microwave and far-infrared applications.[35-39] Substrate-induced in-plane compressive strain has been credited for the reported highest T_c value (49 K) in $La_{2-x}Sr_xCuO_4$ ($0.045 \leq x \leq 0.11$) grown on $SrLaAlO_4$ substrate in atomic oxygen.[38] Rare-earth doped $SrLaAlO_4$ crystals are considered suitable for the development of all solid-state lasers because of the comparatively large absorption and emission cross-section obtained.[40]

There are few reports on surface treatments of $SrLaAlO_4$ substrates. For example, in their paper on YBCO grown on $SrLaAlO_4$, Le Paven-Thivet *et al.*[37] mentioned the use of annealing and chemical etching for improving the surface morphology, but no information about the actual procedure is given.

4.2.5 (001) $KTaO_3$

$KTaO_3$ is an incipient ferroelectric material that exhibits a dielectric nonlinearity at low temperatures (< 30 K).[41] A potential application of $KTaO_3$ crystals is as tunable element in microwave circuits and has been used as substrate for growth of high-T_c superconductors.[42-44] Its close lattice match with $KNbO_3$ also makes $KTaO_3$ ideal as substrate or buffer layer for the growth of ferroelectric $KNbO_3$ films.[45]

$KTaO_3$ has a perovskite structure (see Table 4.1) with cell parameter a = 3.989 Å, in bulk, and slightly smaller unit cell parameter for thin films.[41,46] It does not have any phase transition up to ~ 1640 K,[47] making it an ideal substrate for growing twin-free thin films. However, even that $KTaO_3$ is an oxide intensively studied for its ferroelectric properties, there is no specific data on surface morphology studies when used as substrate.

Table 4.1 *Structural parameters of oxides used as substrates in this thesis.*

Oxide	Orientation	Symmetry	Space group	Lattice parameters[i]	ε^{i}	Tan δ	α (10^{-6}/K)	Phase transf. (K)	mp (K)	Ref.
$SrTiO_3$	001	cubic, perovskite type	$Pm\bar{3}m$ (T > 108 K)	a = 3.905 Å	277	6×10^{-2} (100 K, 300 GHz)	8.6	108	2353	60
		tetragonal	I4/mcm (T < 108 K)							
$NdGaO_3$	001	orthorhombic, $GdFeO_3$ type	Pbnm	a = 5.428 Å b = 5.498 Å c = 7.708 Å	20	3×10^{-4} (77 K, 5 GHz)	7.45	> 1300	1873	60, 61
	110	Pseudocubic (perovskite type with displaced oxygen ions)	-	a_p = 3.865 Å c_p = 3.857 Å γ = 89.26°						60, 61
LSAT	001	cubic, perovskite type	$Pm\bar{3}m$ (T > 150 K)	a = 3.868 Å	22	1.7×10^{-4} (77 K, 8.8 GHz)	5.8	150		32, 33, 60
		tetragonal	I4/mcm (T < 150 K)							33
$SrLaAlO_4$	001	tetragonal, K_2NiF_4 type	I4/mmm	a = 3.754 Å c = 11.263 Å	17	5×10^{-4} (100 K, 8 GHz)		-	1923	60, 62
$KTaO_3$	001	cubic, perovskite type	$Pm\bar{3}m$	a = 3.989 Å				1630		41, 46

[i] room temperature values

ε = dielectric constant, tan δ = dielectric loss, α = thermal expansion coefficient, mp = melting point

Table 4.2 *Known surface preparation methods of oxides used as substrates in this work.*

Substrate	Terminating layer	Coverage (%)	Surface preparation	Ref.
(001) $SrTiO_3$	TiO_2	100	BHF etched	23
(001) $SrTiO_3$	SrO	80-100[i]	O_2 annealing at 950-1000 °C, 0.5-2 h	11,12,23
(001) $NdGaO_3$	$NdO_{1+\delta}$	100	Annealing at 1000 °C in air for 2 h	23
(001) LSAT	$AlO_{2-\delta}/TaO_{2-\delta}$	91±3	Annealing at 1300 °C in air for 2 h	23

[i] The actual coverage value depends on the substrate miscut angle.

4.3 Experimental methods

The morphology of the as-received (commercial) substrates is determined by the polishing method. Their surface consists of islands, randomly distributed on the surface, with typical height of (n + ½) uc resulting, therefore, in a mixed termination (i.e., AO and BO_2 for a perovskite oxide). Impurities, such as C and organic compounds, and surface defects are often present on the surface of the as-received substrates. A low-temperature annealing (typically at 500-600 °C) in O_2 flow (*ex situ*) or in vacuum is generally used for removing the surface contaminants.[48] Here, chemical or thermal treatments are used to further improve the surface crystallinity and, if possible, to control the chemistry of the terminating layer. These surface preparation methods will be discussed next.

Single crystal wafers[8] with dimensions[iii] of 10×10×1 mm^3 were used for annealing and chemical etching experiments. Each wafer was cut in slices of about 3×5×1 mm^3 and sequentially cleaned with chloroform (30 min), acetone (20 min), and ethanol (20 min) to remove the wax used during cutting. The resulted slices were then used for the annealing or etching experiments.

4.3.1 Thermal procedures

The evolution of the surface morphology versus oxygen partial pressure was studied by performing the annealing experiments *in situ*, in the PLD system equipped with high-pressure RHEED (presented in Chapter 3) and *ex situ*, in a tube oven. For *in situ* experiments, vacuum and oxygen annealing ($pO_2 \leq 10^{-1}$ mbar) were performed. For these annealing conditions (*in situ* or *ex situ*), the evolution of the surface morphology was studied as a function of angles Δ and α.

The *ex situ* annealing experiments of the as-received or chemically etched substrates have been performed in a modified tube-oven, using flowing oxygen (at a rate

[iii] For (001) $KTaO_3$ substrates these dimensions were 10×10×0.5 mm^3

of 50-400 l/h) or air. The substrates were placed on an Al_2O_3 boat inside a quartz tube. For re-growth or recrystallization of the step ledges, the annealing temperatures were selected above the threshold temperature for each substrate (e.g., about 800 °C for $SrTiO_3$). The temperature was ramped to the desired value with a rate 0.3 °C/s. The annealing temperature, time and atmosphere used take into account the substrate type and the value of the vicinal angle.

4.3.2 Chemical procedures

Chemical etching considers the layered structure of the substrate materials under investigation and the difference in chemical reactivity of the constituent oxides. The etching procedure is based on the methods developed for $SrTiO_3$.[9,11,12] By this method, one of the surface oxides (i.e., the one with base character, e.g., NdO_{2-x} in case of $NdGaO_3$) is selectively removed by means of a chemical reaction (see next for a complete discussion). In finding the right etching conditions (i.e., the etching time and the pH of the etchant), one has to consider several parameters, such as:

a) the characteristic surface properties of each substrate (e.g., the type of constituent oxides, the vicinal angle);
b) the correlation between etching speed and the orientation of the miscut angle vs. in-plane crystallographic axes[iv] (the etching being more aggressive with increasing this angle),[10] and, off course,
c) the reactivity (pH) of the etching solution.

The etching experiments were done at temperature of up to 70 °C, in a ultrasound bath. HF + NH_4F + H_2O (a modified commercial BHF solution), HCl + NH_4OH + H_2O (or BHCl), HCl + HNO_3 + H_2O, and HCl solutions were used as etchants. The preparation and properties (e.g., pH value) of these solutions will be discussed separately for each substrate. The general etching procedure consisted of several steps.[9-12] The substrates were first soaked in analytical grade and deionised water (Q_2)[v] for up to 0.5 h (depending on the substrate type and the value of its miscut angle, the lower the later the longer the soaking time used). Taking into account the differences in chemical properties of the substrates component oxides, the aim of this step is the selective transformation of the surface A_nO_m in a hydroxide complex, which then can be easily removed by the etchant through transfer of the hydroxide complex into solution.[11,12] The chemical reactions taking place during etching can be generally written as:

$$A_nO_m(s) + xH_2O(l) \rightarrow A(OH)_m \cdot x(H_2O)(s) \quad (4.1)$$

$$HX(aq) \xrightarrow{H_2O} X^-(or\ HX^{2-})(aq) + H^+(aq) \quad (4.2)$$

$$A(OH)_m \cdot x(H_2O)(s) + X^-(or\ HX^{2-})(aq) \rightarrow AX_m \cdot y(H_2O)(aq) \quad (4.3)$$

The etching solutions were chosen based on the reactivity of the A_nO_m and the solubility in water of the reaction product $AX_m \cdot y(H_2O)$, which has to go in solution. To remove any traces of the $AX_m \cdot y(H_2O)$ from the substrate surface (the $AX_m \cdot yH_2O$ complex can

[iv] This angle will be defined as Δ (see Fig. 4.1b).

[v] The deionised water (pH = 6-7, R = 10-15 MΩ) used for the etching experiments was produced with Millipore Elix equipment

decompose in the A_nO_m and then it can precipitate on the surface during the annealing step, see further) the etched wafers are manually rinsed in Q_2 for about 10-20 seconds. To facilitate surface recrystalization a final (ex-situ) annealing step is performed at 800-1100 °C in air or in oxygen flow.

The surface morphology after the chemical or thermal treatment was analysed by means of *ex situ* AFM and *in situ* high-pressure RHEED. In case of AFM, contact and tapping mode has been used. Lateral Force Microscopy (LFM) has been performed in order to determine the presence of different termination(s).[1] The RHEED patterns were recorded in the pulsed laser deposition chamber equipped with the high-pressure RHEED[49-51] described in Chapter 3. The patterns were generally recorded at 5×10^{-2} mbar O_2 at a substrate holder temperature of 550 °C.

In next section, the experimental results of chemical and thermal treatments will be presented. Most data regard the (001) or (110) $NdGaO_3$ substrates, the methods developed for this substrate being then applied and adapted to the other substrates used in this study.

4.4 Experimental results

4.4.1 (110) and (001) $NdGaO_3$

4.4.1.1 Thermal treatment

In Fig. 4.4a an AFM topographic image of the surface of an as-received (110) $NdGaO_3$ substrate after an annealing step at 550 °C (below the threshold for recrystalization) for 0.5 h in O_2 flow is shown. While the surface of such annealed as-received substrates can be considered atomically flat, step ledges of the terraces are rough and, sometimes, hardly visible. The RHEED patterns recorded at 10^{-1} mbar O_2 from such as-received surface showed the formation of a two-domain (2×1) superstructure (Fig. 4.5a and b). The intensity of the superstructure spots decreases in case of patterns recorded in vacuum (8×10^{-7} mbar, see, e.g., Fig. 4.5c). The superstructure formation is possibly due to displacement of cations on the surface, which is enhanced by oxygen adsorption, resulting in an increase in RHEED intensity of the superstructure spots for the surface analysed in oxygen. The formation of streaks for the surface analysed at 900 °C (Fig. 4.5d) indicates an additional roughening by formation of surface defects. At this temperature, formation of oxygen and cation vacancies is enhanced. For an as-received (001) $NdGaO_3$ substrate, the recorded RHEED pattern at 800 °C in vacuum (5×10^{-7} mbar) showed the formation of a two-domain (2×1) superstructure (Fig. 4.8a-c).

In order to improve the surface morphology of the as-received wafers, vacuum annealing was performed. The $NdGaO_3$ samples were annealed in high vacuum (10^{-6}-10^{-7} mbar) or under an O_2 pressure (10^{-1} mbar), at temperatures of 500-900 °C. After the thermal treatment, the surface contaminants were removed, but the mixed termination character of the surface remained. For example, the evolution of surface morphology for (110) $NdGaO_3$ annealed at 800 °C for 0.5 h in vacuum and in O_2

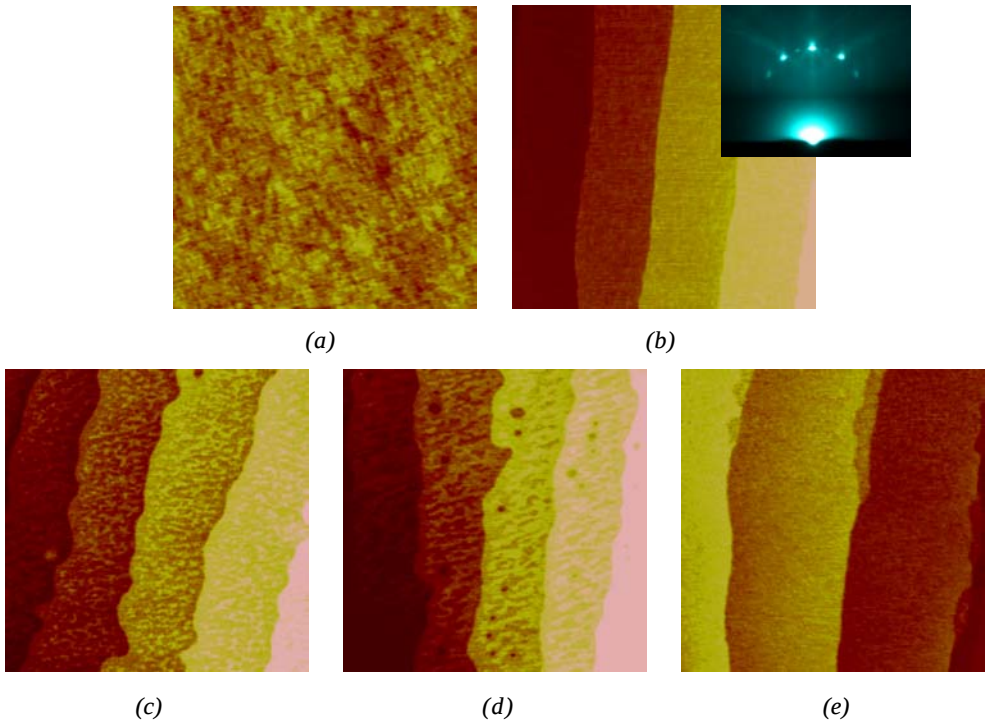

Fig. 4.4 *Topographic AFM micrographs of (110) $NdGaO_3$: (a) as-received and annealed 0.5 h at 550 °C in O_2 flow (100 l/h), (b) annealed 0.5 h at 950 °C in air and corresponding RHEED pattern, (c) annealed 1 h at 950 °C, in O_2 flow (200 l/h), (d) annealed 1 h at 950 °C, in O_2 flow (500 l/h), and (e) annealed 1 h at 1000 °C in O_2 flow (100 l/h). Scan size: (a) 4×4 μm², (b) 1×1 μm², (c) and (d) 2×2 μm², (e) 1.25×1.25 μm²*

(10^{-1} mbar) is presented in Fig. 4.6. Annealing under O_2 resulted in a better surface morphology as shown by the topographic AFM (Fig. 4.6a and b) and confirmed by RHEED patterns depicted in Fig. 4.7. The RHEED patterns of the vacuum annealed surface show diffraction spots on a streaky background, while the annealing in O_2 results mainly in a RHEED pattern without streaks, an indication of a smoother surface with better crystallinity. Both vacuum and O_2 annealing lead to surfaces presenting a two-domain (2×1) superstructure (see Fig. 4.7a-d). Stronger superstructure patterns resulted after O_2 annealing (Fig. 4.7c and d), comparing with those of vacuum annealed (Fig. 4.7a and b), which are very fade. The RHEED and AFM analyses showed that further roughening of the surface takes place when the annealing time (Fig. 4.7e) or annealing temperatures (Fig. 4.6c and d, and Fig. 4.7f) are increased.

The (001) surface energy seams to be lower than that of (110) $NdGaO_3$. A single domain (2×1) superstructure was observed in RHEED patterns of the as-received (001) $NdGaO_3$ wafers (see, e.g., Fig. 4.8a). However, vacuum annealing (1 h at 800 °C) resulted in a (1×1) surface, as can be seen from the RHEED data (Fig. 4.8b and c).

Next, the evolution of surface morphology was studied for *ex situ* annealing (in air or O_2 flow). In Fig. 4.4b a topographic AFM image of the surface morphology of an (110) $NdGaO_3$ wafer annealed for 0.5-1h at 950 °C in air is shown. An atomically smooth surface with terraces of one unit cell (c_p) high has resulted. The surface quality is confirmed by the corresponding RHEED pattern (recorded at 550 °C and 0.1 mbar O_2). A similar result was obtained for 0.5 h annealing at 950 °C in O_2 flow (100 l/h). For O_2 annealing, surface defects probably formed as result of surface decomposition were observed for longer annealing time (i.e., 1 h) and higher temperature (e.g., 1000 °C). In Fig. 4.4c is depicted the surface morphology of an (110) $NdGaO_3$ wafer annealed in an O_2 flow at 950 °C for 1 h. The annealing resulted in a surface with mixed termination. The following mechanism is proposed for this change in surface morphology with temperature and oxygen partial pressure. For this, the structural properties of the (110) surface[vi] and the possible terminating layer(s) at the actual annealing conditions are considered. Ga-terminated surface is oxygen reach compared to the Nd-terminated surface. Oxygen evolution from the Ga-O surface upon heating (for example in air) would render this surface unstable. The loss of surface oxygen will favour segregation of the surface Ga atoms into oxygen-rich subsurface sites and outward segregation of the Nd atoms to the surface. Loss of the O atoms from the Ga-O surface decreases the oxygen coordination of the adjacent Ga atoms and, at sufficiently high temperatures the Ga-O bonds are destroyed. Ga atoms would diffuse out of the surface; a switch in termination can also take place, Nd-O surface been more stable. The stability of Ga-O surface it is therefore expected to be higher in an oxygen environment than in air, while in air the Nd-O termination is preferably formed, as was shown by Ohnishi *et al.*[23] Therefore, the islands that can be seen in Fig. 4.4c are expected to be $GaO_{2-\delta}$ terminated.

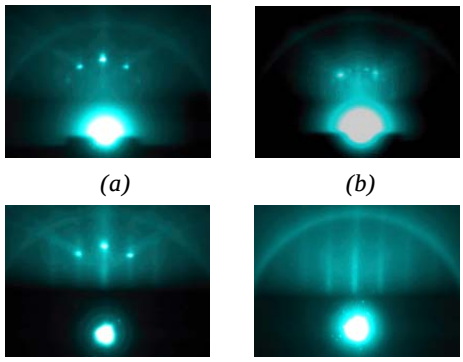

Fig. 4.5 *RHEED patterns of as-received (110) $NdGaO_3$ recorded at (a) 800 °C and 10^{-1} mbar O_2 (on $[100]_p$ direction), (b) 800 °C and 10^{-1} mbar O_2 (on $[110]_p$ direction), (c) 800 °C and 8×10^{-7} mbar (on $[100]_p$ direction), and (d) 900 °C and 2×10^{-6} mbar (on $[100]_p$ direction).*

[vi] i.e., the position of the oxygen ions determined by tilting of the oxygen octahedral (see Fig. 4.2).

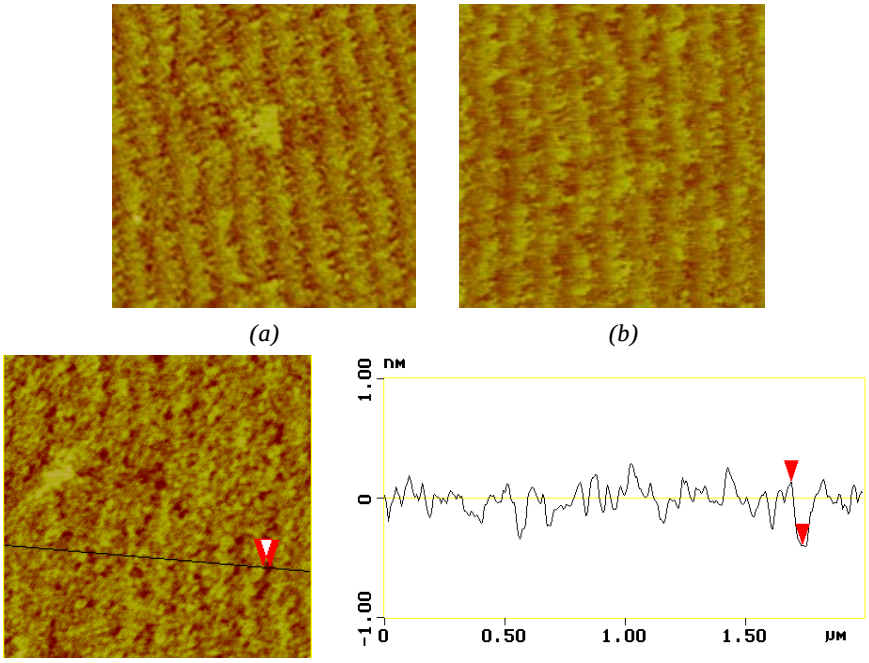

Fig. 4.6 *AFM micrographs of (110) $NdGaO_3$. (a) annealed 0.5 h at 800 °C in vacuum (5×10^{-7} mbar). (b) annealed 0.5 h at 800 °C in O_2 (10^{-1} mbar). (c) annealed 1 h at 900 °C in vacuum (10^{-6} mbar). (d) cross section of (c). Scan size a) - c): 2×2 μm^2.*

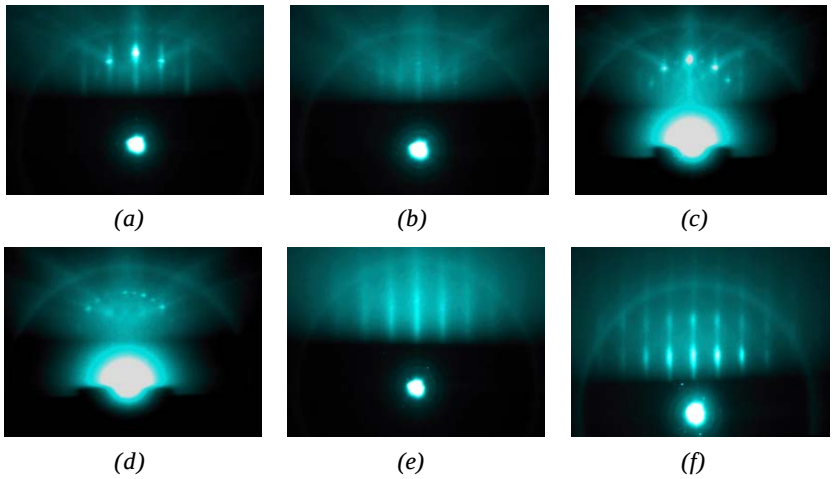

Fig. 4.7 *RHEED patterns of (110) $NdGaO_3$ annealed 0.5 h at 800 °C: (a) and (b) in vacuum (5×10^{-7} mbar), (c) and (d) in O_2 (10^{-1} mbar); annealed 1 h at (e) 800 °C in vacuum (4×10^{-7} mbar) and (f) 900 °C in vacuum (10^{-6} mbar).*
Electron beam on [100] direction of substrate for (a), (c), (e) and (f), and on [110] direction for (b) and (d), respectively.

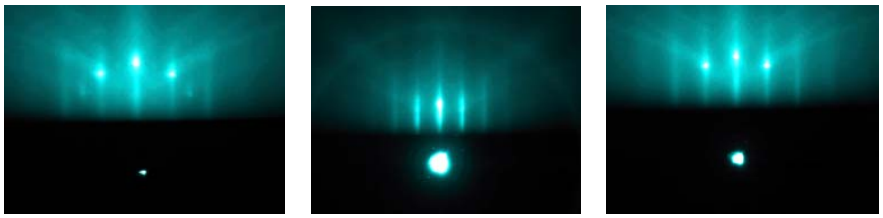

(a) *(b)* *(c)*

Fig. 4.8 *RHEED patterns of (001) $NdGaO_3$: (a) and (b) the as-received substrate, and (c) after annealing for 1 h at 800 °C in vacuum (3×10^{-7} mbar).*
RHEED patterns were recorded at 800 °C and 5×10^{-7} mbar with the beam on [100] direction for (a) and (c), and on [110] direction for (b), respectively.

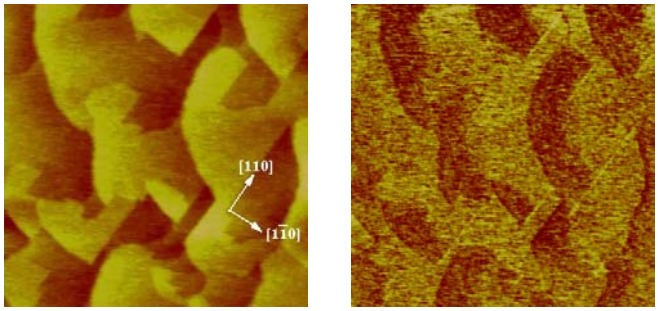

(a) *(b)*

Fig. 4.9 *(a) Topographic AFM micrographs of (110) $NdGaO_3$ annealed 1h at 950°C in air (scan size 1.5×1.5 μm^2); the crystallographic axes form and angle of 45° with the direction of the terraces – the surface miscut is along the [110] crystallographic axis. (b) LFM of (a) showing the mixed termination of the substrate surface.*

Following the above mechanism, it is expected that annealing in an increased O_2 flow and/or at lower temperature to better stabilize the $GaO_{2-\delta}$ surface. This is demonstrated in Fig. 4.4c and d, showing two (110) surfaces of $NdGaO_3$ wafers annealed under different O_2 flows (200 and 500 l/h, respectively). At higher temperatures (e.g., 1000 °C) $GaO_{2-\delta}$ surface is unstable, the main termination of the wafers annealed in oxygen flow at these temperatures being $NdO_{1+\delta}$ (see, e.g., Fig 4. 4e). For this surface a height difference of 0.1 nm was determined from scan profile line (not shown) between the main top layer (considered to be $NdO_{1+\delta}$)[23] and the ledge defect layer ($GaO_{2-\delta}$). Therefore, an increase of about 0.1 nm of the Ga-O bond length resulted for the ledges defect layer. Surface relaxation and rumpling of top layers of surfaces were already observed and studied experimentally (by LEED[52] or RHEED[53] measurements), theoretically (e.g., shell model)[54] or by a combination of HREM and theoretical direct methods[55] for substrates such as $SrTiO_3$ annealed in vacuum or in oxygen.

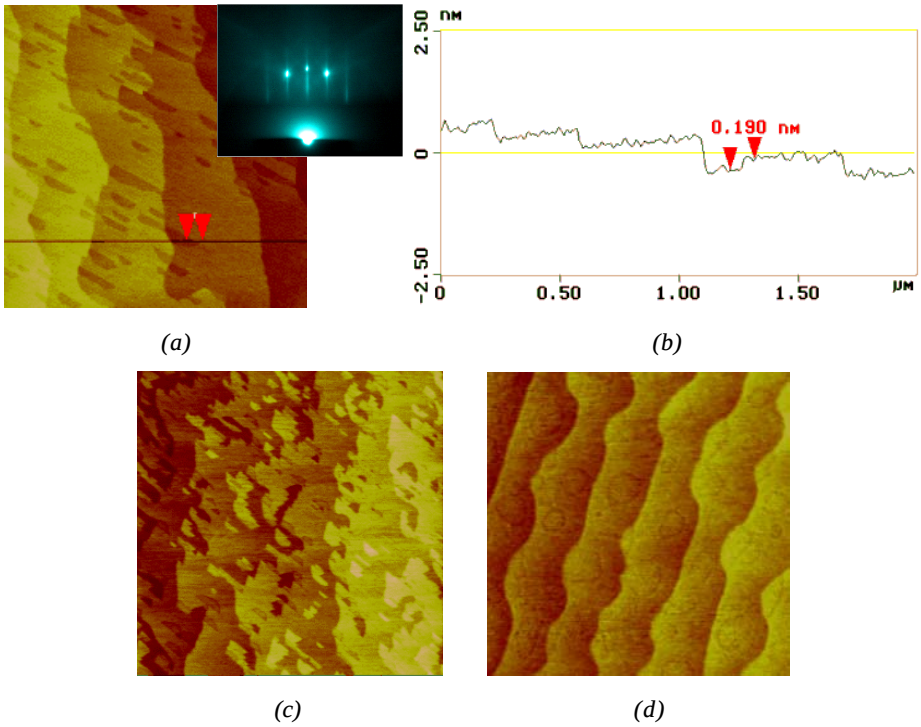

Fig. 4.10 *AFM micrographs of (110) $NdGaO_3$ (a) annealed 2 h at 1000 °C in O_2 flow (400 l/h) and corresponding RHEED pattern on [100] direction (recorded at 550 °C, 5×10^{-2} mbar O_2). (b) line scan profile of (a) showing the presence of ½ unit cell height defects on one unit cell height terraces. (c) annealed for 1 h at 950 °C in O_2 flow (400 l/h). (d) annealed 1 h at 1000°C in O_2 flow (200 l/h).*
Scan size: (a) 2×2 μm^2, (c) 2.5×2.5 μm^2, and (d) 1.5×1.5 μm^2.

As mentioned above, the value of angle Δ is one of the parameters that may determine the surface morphology. As an example, in Fig. 4.9a topographic AFM micrograph of an (110) $NdGaO_3$ characterized by $\Delta = 45^o$ is shown. The substrate was annealed at 950 °C for 1 h in air, the same conditions as for the sample presented in Fig. 4.4b. As resulted from the LFM image of Fig. 4.9b, the topmost layer consists of $NdO_{1+\delta}$ and $GaO_{2-\delta}$ (differences in friction contrast are associated with the presence of different phases on the topmost layer). This is in contrast with the results on surface morphology for substrates characterized by $\Delta \sim 0^o$, where a single terminated surface was obtained under similar annealing conditions.

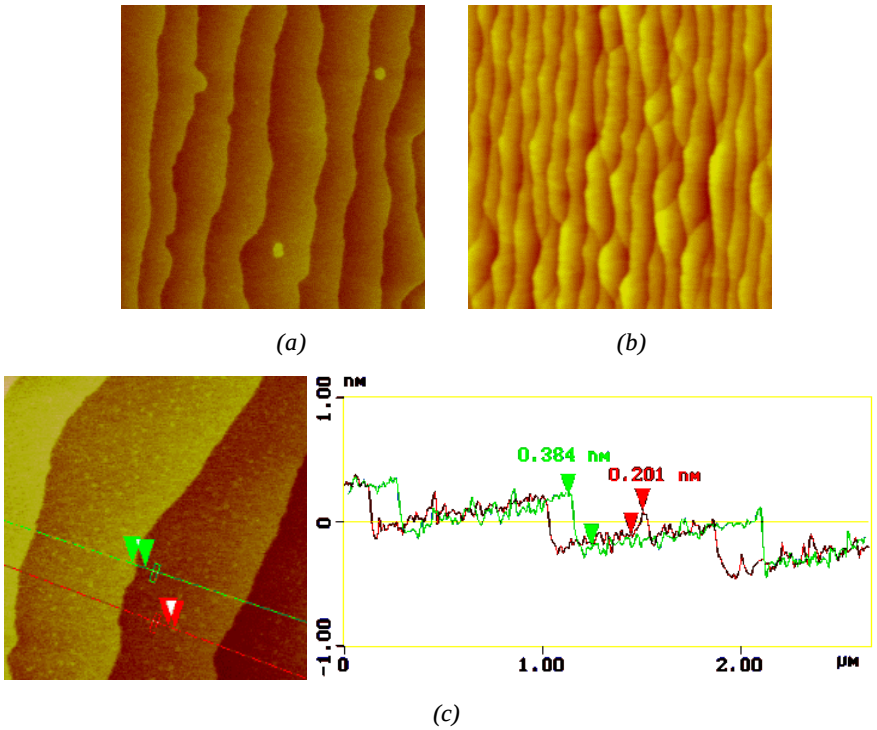

Fig. 4.11 *Topographic AFM micrographs of annealed (001) $NdGaO_3$ (a) 0.5 h at 1000 °C in air or O_2 flow (200 l/h). (b) 1 h at 950 °C in air. (c) 1 h at 1000 °C in air; the line scan profiles shows the presence of ½ unit cell height islands on one unit cell height terraces. Scan size: (a) 3×3 μm², (b) 2×2 μm², and (c) 2.5×2.5 μm².*

Oxygen annealing of (110) $NdGaO_3$ characterized by different values of Δ have resulted in surface defects. For example, in Fig. 4.10a is depicted the topographic AFM micrograph for a substrate ($\Delta \approx 45^o$) annealed in O_2 flow (400 l/h) at 1000 °C for 2 h showing the presence of surface defects as rectangular-shaped pits of half unit cell high (~ 0.2 nm, as determined from the AFM line scan profile, Fig. 4.10b). The associated RHEED pattern shows diffraction dots on a streaky background. The presence of the diffraction dots is an indication of an atomically flat surface, while the formation of the streaks is due to the existence of the surface defects. A longer annealing time in O_2 flow at 950-1000 °C leads to a higher concentration of the surface defects. Similar results yields the annealing of (110) $NdGaO_3$ characterized by $\Delta \sim 0^o$, with the difference in the shape of the surface defects. They form at the terraces ledge and on the terraces and they have a height of about 0.1 nm, which indicates an increase of the Ga-O bond length on the area of these defects. Formation of the surface defects could be avoided or reduced by annealing at lower temperatures or for shorter time.

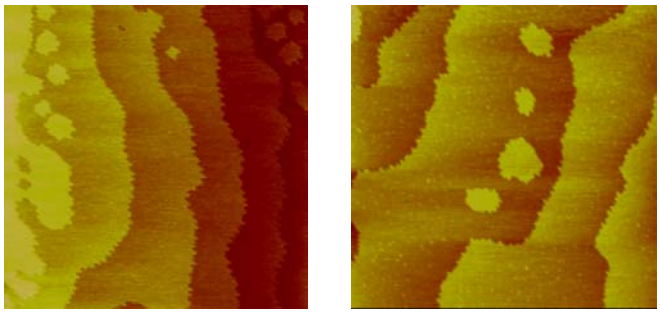

(a) *(b)*

Fig. 4.12 *Topographic AFM micrographs of annealed (001) $NdGaO_3$: (a) 70 min at 1000 °C in O_2 flow (50 l/h) and (b) 2 h at 1000 °C in air.*
Scan size: (a) 5×5 μm^2 and (b) 3×3 μm^2.

As for (110) $NdGaO_3$, the annealing of (001) $NdGaO_3$ for 0.5 h at 950–1000 °C in air resulted in an atomically flat surface with one-step high terrace structure, as shown in Fig. 4.11a. However, while this is valid for wafers characterized by a miscut angle $\alpha \sim 0.1\text{-}0.2^0$, formation of step bunching was observed for higher vicinal angles (see, e.g., Fig. 4.11b). It is worth to mention that while the annealing in O_2 flow (50-200 l/h) at these conditions resulted in a better surface morphology than in the case of (110) $NdGaO_3$ annealed under the same conditions, the AFM micrographs showed the presence of surface defects presumably due to Nd and/or oxygen deficiency. Their concentration increased with the annealing time and for higher O_2 flow values. For (001) $NdGaO_3$ wafers characterized by $\alpha < 0.1^o$, an increase of the annealing time at 1000 °C to 1 h resulted in a surface presenting small islands. These islands have a height of ~ 0.2 nm (see Fig. 4.11b and the line scan profile) corresponding to $½c_p$ or the distance between $NdO_{1+\delta}$ and $GaO_{2-\delta}$ planes. By considering the $NdO_{1+\delta}$ as the main termination,[23] the resulted composition of the islands termination layer is $GaO_{2-\delta}$. A longer annealing time was required for yielding a single terminated surface for substrates with low miscut angles (of the order of 0.1^o or lower).

For (001) $NdGaO_3$ wafers characterized by similar value of the vicinal angle, annealing in O_2 flow takes less time to yield a single terminated surface than annealing in air. Fig. 4.12a shows a topographic AFM micrograph of an (001) $NdGaO_3$ annealed for 70 min at 1000 °C in flowing O_2. A terraced surface with steps of one unit cell height had resulted. However, annealing in air at same temperature for 2 h resulted in a mixed terminated surface - small islands with $½\times c_p$ height can be observed (Fig. 4.12b). The edges of the terraces show a saw tooth structure, with facet faces parallel to the [100] or [010] directions.

The results of annealing are complex and there are many parameters determining the final surface morphology. A control of the surface morphology for the annealed $NdGaO_3$ substrates is difficult. It requires knowledge of the substrate vicinal angle as well as its direction. Therefore, chemical etching was applied with the aim of

reproducibly obtaining single terminated (110) and (001) $NdGaO_3$ substrates, with $GaO_{2-\delta}$ as single termination.

4.4.1.2 Chemical etching

For chemical etching experiments, a modified commercial buffered hydrogen fluoride solution ($HF + NH_4F + H_2O$ or modified-BHF) has been used. The etching process consists of soaking the wafers in deionised water for 10-20 min resulting in hydroxide [$Nd(OH)_3 \cdot xH_2O$] formation at the surface, followed by immersion in the etchant for different periods of time (30 to 120 s). The etching time is selected so that the lower the substrate vicinal angle value, the longer the etching time. The entire procedure takes place in an ultrasonic bath, at room temperature. The substrates are then rinsed for few seconds with deionized water, and finally dried with ethanol and nitrogen flow. The etched samples are finally annealed at 950-1000 ºC for 0.5-4 h in air or oxygen flow (50-200 l/h) to facilitate surface recrystallisation.

Due to different surface energy (as concluded from annealing experiments), chemical treatment of (110) and (001) $NdGaO_3$ substrates had to be done in solutions with different pH values, higher for former and lower for latter, respectively. Therefore, an etchant with a lower reactivity was used for removing $NdO_{1+\delta}$ from (110) $NdGaO_3$ surface. The commercial available BHF solution (12.5 vol% HF + 87.5 vol% NH_4F) used for $SrTiO_3$ etching[19-12] was too strong for the purpose of this work. Chemical solutions with different pH values were prepared for (110) $NdGaO_3$ and (001) $NdGaO_3$, considering the surface properties. As prepared, the etching solution for (110) $NdGaO_3$ consisted of 10 ml commercial BHF + 4 ml NH_4OH (37 vol%) + 90 ml Q_2. The resulted solution has a pH = 5.0-5.5. For (001) $NdGaO_3$ the etching solution consisted of 20 ml commercial BHF + 3 ml NH_4OH (37 vol%) + 110 ml Q_2; a solution with pH = 4-4.5 had resulted.

The etching solutions were prepared based on the following considerations: due to the strong electrolyte properties of NH_4F, a large amount of F^- ions is generated in the $HF + NH_4F + H_2O$ solution.[57] Consequently, a large amount of difluoride ions, HF_2^-, is formed in solution according to the following reaction:

$$HF(aq) + F^-(aq) = HF_2^-(aq) \qquad (4.4)$$

The F^- formation is part of the ionisation process in the $HF + H_2O$ system. By reducing the amount of F^- and HF_2^- ions through neutralisation with NH_4OH, the reactivity of the resulted modified BHF solution is reduced to yield the desired pH and, therefore, the necessary reactivity. By this procedure, the reactivity of the modified-BHF solution is suitable for reproducible preparing atomically smooth (001) and (110) $NdGaO_3$ substrates surface without etch pits.

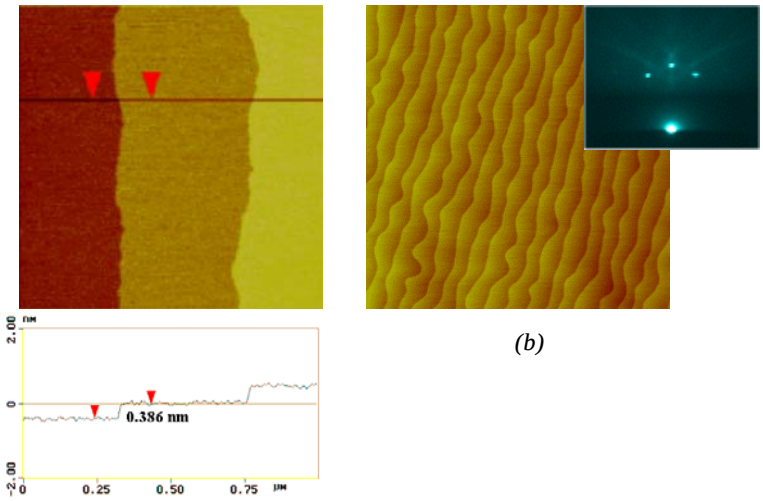

Fig. 4.13 *Topographic AFM micrographs and corresponding RHEED pattern of (110) $NdGaO_3$ etched 0.5 min in BHF and then annealed 2 h at 1000 °C in O_2 flow (100 l/h). The cross section shows one unit cell terraces; the RHEED pattern, recorded at 5×10^{-2} mbar O_2 and 550 °C, shows sharp Kikuchi lines typical for an atomically smooth crystalline surface. Scan size: (a) 1×1 μm^2 and (b) 7×7 μm^2.*

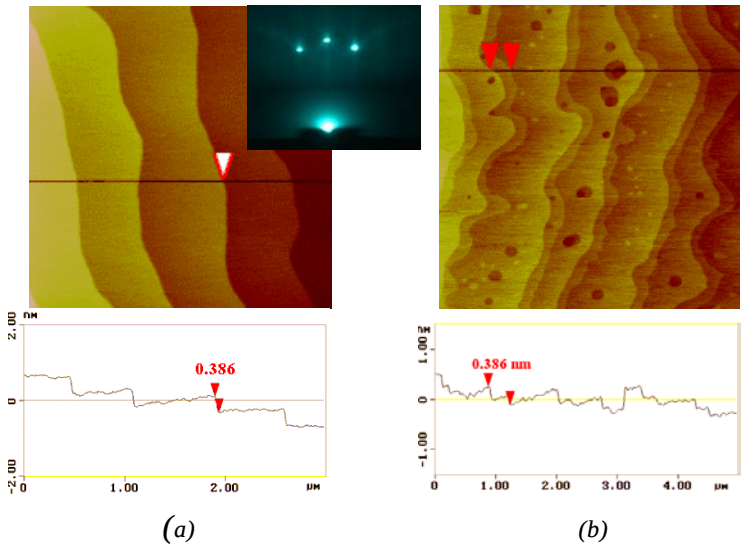

Fig. 4.14 *Topographic AFM micrographs of (001) $NdGaO_3$. (a) etched 2 min in BHF (pH = 4) and annealed 2 h at 1000 °C in air or O_2 (200 l/h). (b) etched 2 min in BHF (pH = 5.5) and annealed 2 h at 1000 °C in O_2 flow (200 l/h).*
Scan size: (a) 3×3 μm^2 and (b) 5×5 μm^2.

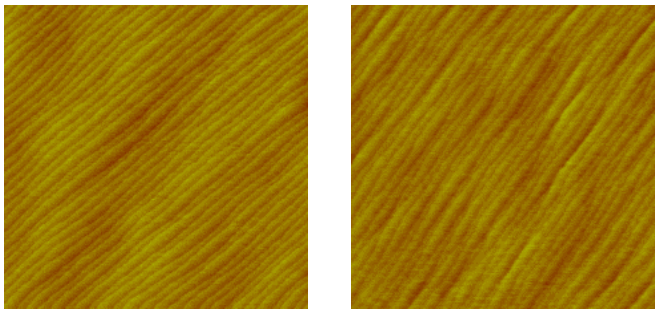

(a) *(b)*

Fig. 4.15 *Topographic AFM micrographs of (001) $NdGaO_3$ (a) etched 5 min in HCl and annealed 1 h at 950 °C in O_2 flow (200 l/h). b) etched 1 min in commercial BHF and annealed 1 h at 950 °C in O_2 flow (200 l/h). Scan size: (a) and (b) 2×2 μm^2.*

As will be shown further, the actual shape of the step edges depends not only on the pH of the etchant and on the etching time, but also on the substrate miscut angle and its direction, due to difference in etching speed.[10] In Fig. 4.13a-b topographic AFM micrographs and corresponding RHEED pattern of an etched (110) $NdGaO_3$ wafer are shown. As proved by the cross section line a surface morphology characterised by a terraced structure with one-unit cell (c_p) steps has resulted. The RHEED pattern of the etched and annealed wafer shows sharp narrow spot and Kikuchi lines characteristic of a surface with high crystallinity. A similar surface properties yield the etching of (001) $NdGaO_3$ with the pH = 4 modified-BHF solution, as shown in Fig. 4.14a. The substrates are etched for 0.5-2 min and then annealed at 950-1000 °C in air or O_2 flow (50-200 l/h). A slightly higher etching time (about 2 min) was found to be necessary to yield B-site single terminated surface for substrates with relatively low miscut angle (< 0.1°). Etching the (001) $NdGaO_3$ with the solution prepared for (110) $NdGaO_3$ leads to an incomplete etching. The AFM image of such surface showed a mixed termination, see Fig. 4.14b. An increase of the etching time resulted in a decrease of the amount of $NdO_{1+\delta}$, but also in the presence of etched pits in the $GaO_{2-\delta}$ layer. The mixed termination character of the surface did not change. This result confirmed the difference in the surface energies for (110) and (001) $NdGaO_3$, with lower for later.

A less reactive etching solution, i.e., buffered hydrochloric acid (HCl + NH_4OH + H_2O or BHCl), was found to give similar results for etching of $NdGaO_3$ substrates with relatively high miscut angle (> 0.5°). The solution consisted of 10 ml HCl (25 vol%) + 4 ml NH_4OH (37 vol%) + 90 ml Q_2. The resulted solution had a pH ~ 1.5. In Fig. 4.15 are shown the AFM images of two (001) $NdGaO_3$ wafers etched in BHCl (for 5 min, Fig. 4.15a) and in commercial BHF (for 1 min, see Fig. 4.15b), respectively. A terraced structure of one-unit cell (c_p) height steps resulted in both cases, with some step bunching presented for the wafer etched in BHF.

4.4.1.3 Discussions

The results of high temperature thermal treatment on (001) and (110) $NdGaO_3$ substrates strongly depend on the annealing atmosphere (e.g., air or oxygen), on the value of the substrate vicinal angle, α, as well as on its direction, Δ. The annealing temperature was selected so that sufficient atomic mobility will enable the formation of a well-defined surface, with terraced structure; their formation is function of annealing temperature and time. The steps form as result of the lowering of the total free energy of the system.[56]

For (001) and (110) $NdGaO_3$, characterized by $\alpha \sim 0.1\text{-}0.2^0$ and $\Delta \sim 0^0$, annealing in air or oxygen flow for ~ 0.5 h at 950 °C can result in a single terminated surface. The topmost layer is $NdO_{1+\delta}$.[23] Increasing the O_2 flow during annealing resulted in an enhancement of the surface decomposition at the terrace ledges, with islands formation. This phenomenon is more pronounced for the (110) surface. Part of the islands coalesce, while the $GaO_{2-\delta}$ remained on the surface formed a closed layer at the terraces ledge. A possible explanation of these results is a difference in the composition of the topmost layer for substrates annealed at temperatures lower than 950 °C and for those annealed at higher temperature (e.g., 1000 °C). The switch in termination is enhanced at higher annealing temperatures and by annealing in air, which results in faster decomposition of one of the surface oxides. Further experiments are necessary to validate this conclusion. An important conclusion of the annealing experiments is the observation that the (001) surface is more stable than the (110) surface. This is determined by the oxygen network, as well as by the strength of the Nd-O and Ga-O bonds on the surface. This feature have to be considered when selecting the proper annealing procedure and the chemical solution for etching treatments.

Different etching procedures were developed for (001) and (110) $NdGaO_3$ substrates based on their surface chemistry and miscut angle. Modified BHF solutions can be applied for control of the surface morphology of substrates characterized by relatively low miscut angle, whereas for higher miscut angle (e.g., $\alpha > 0.3^0$) a buffered HCl solution can be used with similar results. The etching process (which involves the chemical and thermal treatment steps) is considered to result in a B-site terminated surface.

4.4.2 (001) $SrTiO_3$

4.4.2.1 Thermal treatment

The annealing of $SrTiO_3$ substrate in different conditions had been intensively studied and presented in literature. It is considered that annealing in O_2 flow at temperatures of 900-1000 °C can lead to an A-site single terminated surface and that regrowth of the step ledges starts at 800 °C.[28] The process is not simple to control and a dependence of the surface morphology for the annealed samples on the substrate miscut angle was observed. In Fig. 4.16 are shown the AFM micrographs of $SrTiO_3$ substrates characterised by different miscut angle values, annealed at 900 °C (Fig. 4.16a and b) and 1000 °C, respectively (Fig. 4.16c). Annealing at 900 °C, even for 2.5 h resulted in a mixed termination, as shown by the LFM in Fig 4.17b. A higher temperature annealing (i.e., 1000 °C) can leads to an A-site single terminated surface, but the miscut angle and

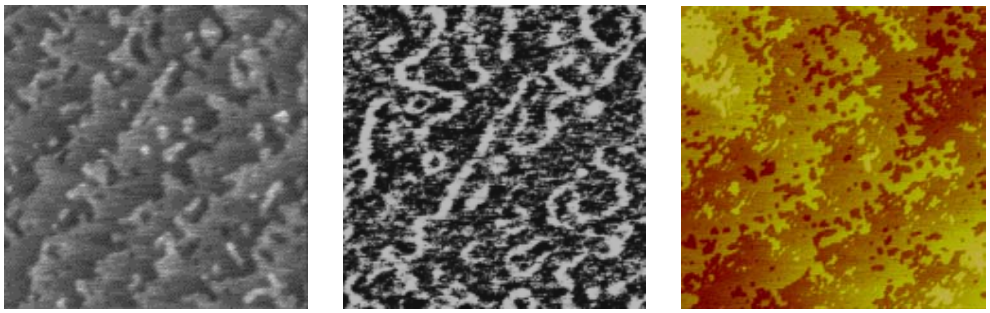

(a) *(b)* *(c)*

Fig. 4.16 *Topographic AFM micrographs of (001) $SrTiO_3$ annealed (a) at 900 °C for 2.5 h in O_2 flow (300 l/h). (b) LFM of (a), but scan size of 0.5x0.5 μm^2. (c) annealed at 1000 °C for 1 h in O_2 flow (400 l/h).*
Scan size: (a) 1×1 μm^2 and (c) 4×4 μm^2.

the annealing time determines the shape of the terrace edges, as shown in Fig. 4.16c. A substrate with low miscut angle (i.e., < 0.1°) requires a longer annealing time and a higher annealing temperature. However, these conditions can result in surface decomposition and nonstoichiometry if the annealing parameters are not selected properly. This requires the knowledge of the miscut angle value before the thermal treatment. The lower the miscut angle, the longer the annealing time and the higher the annealing temperature.

4.4.2.2 Chemical etching

HCl + NH_4OH + H_2O and HCl + HNO_3 + H_2O have been studied as alternative etching solutions to the BHF.[58] The first solution was prepared from 10 ml HCl (35 vol%) + 1 ml NH_3 (25 vol%) + 10 ml Q_2 with a pH = 1-1.25. The role of NH_4OH is to increase the solubility of the reaction products and, therefore, to avoid formation of precipitates on the substrate surface after drying and annealing. The etching procedure consisted of soaking of the wafer in Q_2 for 20-30 min, etching for about 10-12 min and then rinsing in Q_2 for few seconds. All these steps take place in an ultrasound bath at temperatures of 50-70 °C. The use of this temperature was essential for yielding B-site single terminated surface. In Fig. 4.17a topographic AFM of an (001) $SrTiO_3$ etched at these conditions is shown. An atomically flat surface with a terraced structure of one-unit cell steps resulted. The role of soaking in water before etching is shown in Fig. 4.17b, where an AFM image of an (001) $SrTiO_3$ substrate (from the same wafer as the one presented in Fig. 4.17a) etched without the rinsing step is shown. Step bunching and incomplete removal of SrO have resulted. A similar morphology was observed when the etching was performed at room temperature. The increase of the temperature leads to an increase of the reactivity of the etchant with the Sr-hydroxide complex, thus avoiding the formation of etched pits by prolong exposure of the surface to the etchant. After etching the wafers were annealed at 850–1000 °C in O_2 flow (200-400 l/h). The higher the miscut angle the lower the annealing temperature and the value of the O_2 flow. The results showed that a high annealing temperature (e.g., 1000 °C) and/or high

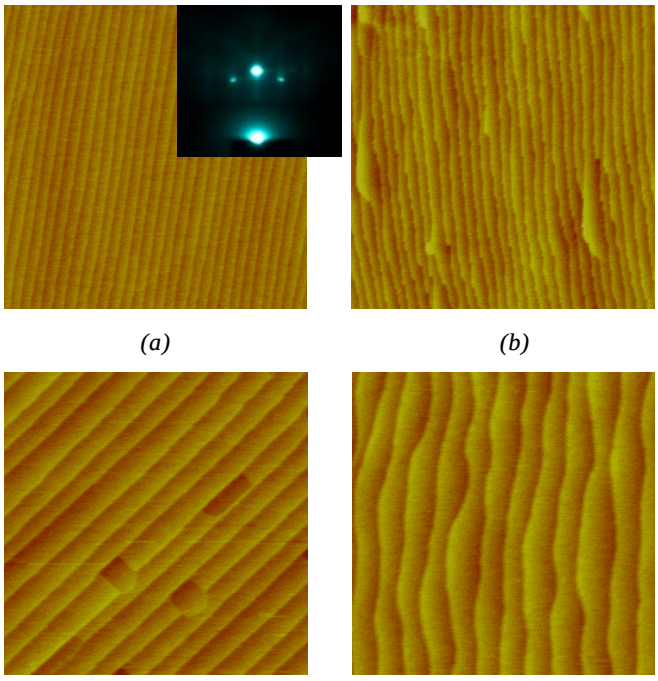

Fig. 4.17 *Topographic AFM micrographs of (001) $SrTiO_3$ (a) etched 10 min in hot (70 °C) BHCl and annealed at 1000 °C for 1 h in O_2 (300 l/h) and corresponding RHEED pattern. (b) idem (a), but no soaking in Q_2 before etching. (c) etched 4 min in hot (70 °C) HCl + HNO_3 and annealed at 1000 °C, 1 h in O_2 (300 l/h). (d) etched 1 min in commercial-BHF and annealed at 950 °C, 1 h, in O_2 flow (400 l/h);*
Scan size: (a) and (b) 2×2 μm^2, (c) and (d) 1×1 μm^2.

oxygen flow (e.g., 400 l/h) associated with a high miscut angle (1-2°) leads to an increase of the probability of a step bunching formation. These parameters (annealing temperature and the O_2 flow) determine the surface mobility during annealing.

The second etching solution discussed here was prepared from 3 ml HCl (35 vol%) + 1 ml HNO_3 (35 vol%) + 10 ml Q_2. For the as prepared solution a pH = 1-1.25 has resulted. The etching procedure consisted of soaking the wafer in Q_2 for 20-30 min, etching for about 3-5 min and then rinsing in Q_2 for few seconds. All these steps take place in an ultrasound bath at temperatures of 50-70 °C, with the temperature set to yield the required reactivity of the etchant for the used etching time. The result of this etching procedure for an (001) $SrTiO_3$ with miscut angle of about 0.35° annealed after etching at 1000 °C for 1 h in O_2 flow (400 l/h) is presented in Fig. 4.17c. A terraced structure with one-unit cell steps was obtained. Some surface defects are presented on some region of the surface. These are probably etched pits (0.2 nm height), but a surface nonstoichiometry induced by the high annealing temperature (1000 °C) or local crystal

defects cannot be ruled out. For comparing, a BHF etched surface is shown in Fig. 4.17d.

Next, the effect of etching using the BHCl solution on (001) $SrTiO_3$ with relatively low miscut angle (< 0.2°) is studied. In Fig. 4.18a and b the surface morphology of two (001) $SrTiO_3$ substrates, characterized by different miscut angles, etched in BHCl and annealed at low temperature (650 °C) in O_2 flow is shown. The effect of 10 min BHCl etching on the $SrTiO_3$ with a miscut angle of about 0.03° is close to insignificant, the surface morphology been similar with the one of an as-received substrate annealed in the same conditions. A more evident effect results for the etching of the $SrTiO_3$ presenting a miscut angle value of about 0.12°. As can be seen from the AFM image of Fig. 4.18b, the etching front developed and evolved from the step edges at the kink sites, characterized by the highest surface energy. The etching front did not developed from a close surface of a terrace. High temperature annealing of the BHCl etched $SrTiO_3$ (the wafer from Fig. 4.18b) leads to surface recrystalization (Fig. 4.18c), but a mixed termination surface with SrO precipitated at the terraces ledge has resulted, as proved

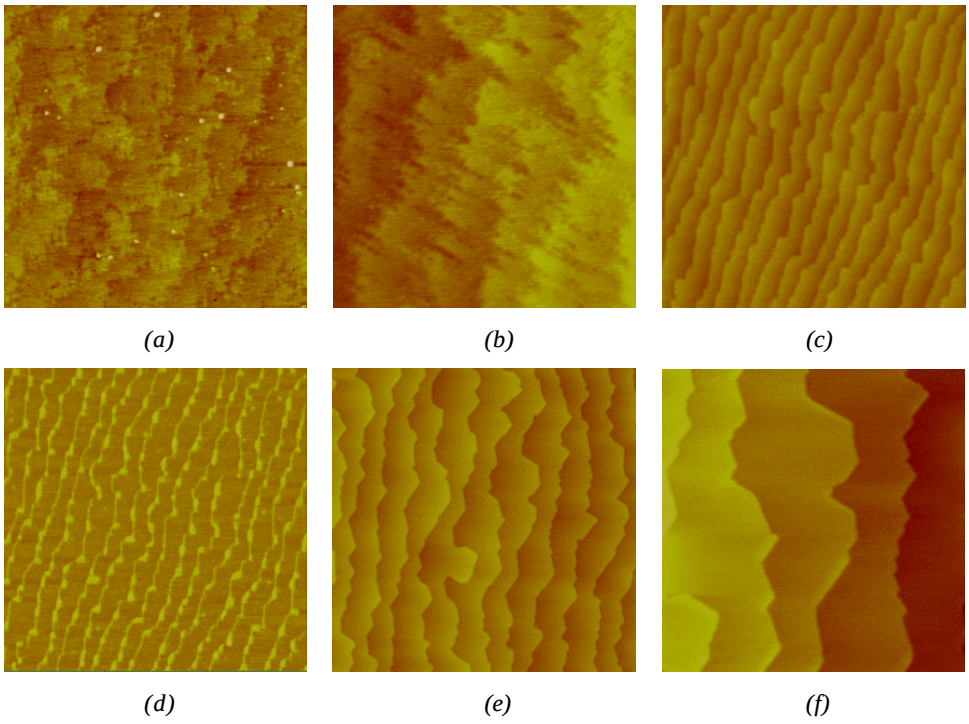

Fig. 4.18 *AFM micrographs of (001) $SrTiO_3$: (a) etched 10 min in hot BHCl and annealed at 650 °C for 45 min in O_2 flow (400 l/h), (b) etched for 12 min in hot BHCl and annealed at 650 °C for 45 min in O_2 flow (400 l/h), (c) etched for 12 min in hot BHCl and annealed at 1000 °C for 10 min, (d) LFM of (c), (e) etched for 10 min in hot BHCl and annealed at 950 °C for 3 h in O_2 flow (400 l/h), and (f) idem (e), but scan size 2×2 μm^2. Scan size: (a) 5×5 μm^2, (b) 1×1 μm^2, (c) 3×3 μm^2, and (e) 5×5 μm^2.*

by the LFM images (Fig. 4.18d). Therefore, the BHCl solution is not suitable (at least for the etching conditions presented in this work) for completely removing the SrO from the substrate surface. The BHF solution remains the right choice for etching (001) $SrTiO_3$ characterized by relatively low miscut angle.

4.4.2.3 Discussions

Surface mobility determines the surface morphology of the annealed wafers. Dependence between the surface morphology and the substrate miscut angle was observed, resulting in not always reproducible results for the annealed wafers. A longer annealing time is required for wafers characterized by values of miscut angle lower than 0.1^o; on the other hand, a too long thermal treatment results in a mixed termination. By optimum annealing, atomically smooth (001) $SrTiO_3$ surface having one unit cell high steps and atomically flat terraces with SrO_x as topmost layer could be obtained. Anyway, high temperature treatment may induce decomposition and nonstoichiometry after a too long annealing time.

Chemical etching was applied in order to selectively remove the surface SrO_x. The etching procedure has to consider the surface characteristics of the wafer (miscut angle, orientation of the terraces, etching speed determined by the local atomic-scale configuration), as well as the etchant properties, e.g., pH value. The main conclusion of the etching experiments is that the first step of the procedure (the soaking in water before the chemical etching) and the use of a solution with an optimum pH are essential for yielding a single terminated surface, without etch pits. The result of the etching process (a B-site terminated surface) is also dependent on the miscut angle and its orientation. For substrates with relatively high value of miscut angle (> 0.5^o) formation of step bunching was observed. Their formation can be avoided or reduced by decreasing the annealing temperature (the higher the miscut angle, the lower the annealing temperature and time).

4.4.3 (001) LSAT

4.4.3.1 Thermal treatment

In Fig. 4.19a the AFM micrograph of an (001) LSAT substrate (miscut angle of 0.18^o) annealed at 1100 ^{o}C in an O_2 flow is presented. As shown by the line scan profile a terraced structure with one-unit cell steps has resulted. Annealing at lower temperature, i.e. 1000 ^{o}C, leads also to a stepped and terraced surface morphology but with a 'wavy' structure of the terraces ledge. The resulted surface shows a mixed termination (Fig. 4.19b). Annealing at higher temperatures (i.e., 1200-1300 ^{o}C), which should result in an improved surface morphology,[23] was not possible in the oven used for the annealing experiments. The thermal treatment is considering to result in mainly $AlO_{2-\delta}/TaO_{2-\delta}$ (B-site) termination, as reported in Ref. 23 (see also Table 4.2). Considering the lower annealing temperature used here, compared with the values (i.e., 1300 ^{o}C) reported by Kawasaki *et al*.[23] in their experiments, a different composition of the termination layer for the annealed (001) LSAT substrates can not be ruled out (see also section 4.4.3.2). For yielding a single B-site termination chemical etching was studied.

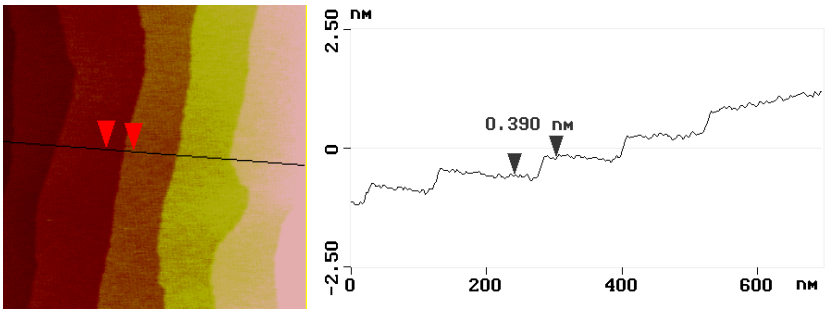

(a)

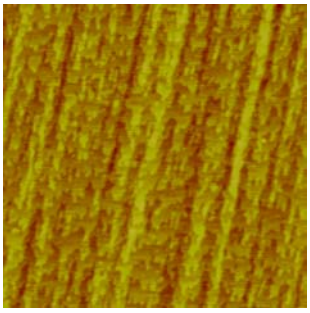

(b)

Fig. 4.19 *Topographic AFM micrographs of (001) LSAT (a) annealed at 1100 °C for 2 h in O_2 flow, and (b) annealed at 1000 °C for 3 h in O_2 flow.*
Scan size: (a) 0.7×0.7 μm^2, and b) 3×3 μm^2. The O_2 flow was set at 300 l/h.

4.4.3.2 Chemical etching

The chemical etching was carried out using two different solutions. The first etching solution was prepared from a mixture of commercial HCl (25 vol%) and HNO_3 (35 vol%) solutions, with the ratio of the acids in solution of HCl:HNO_3 = 3:1. The etching took place at 50-70 °C for 2 min. The wafers were soaked in Q_2 before etching for 2 min and rinsed for few seconds in Q_2 after etching to remove the precipitates from the surface. The etching procedure took place in an ultrasound bath at the same temperature (50-70 °C) for all steps. After drying with ethanol and N_2 flow, the etched wafers were annealed at 1000 °C for 1-36 h in an O_2 flow (200 l/h). In Fig. 4.20a an AFM image of an (001) LSAT substrate etched and annealed at low temperature (in order to remove the surface contaminants) is shown. Some etch pits are visible as holes. After annealing at 1000 °C in O_2 flow the surface recrystalise and a terraced structure with steps of ~ 0.4 nm in height is visible (see Fig. 4.20b). Due to low annealing temperature and relatively low miscut angle of the substrate, the terraces edge are not well defined. However, improved surface morphology was obtained at this temperature after annealing for 36 h. The resulted surface morphology is depicted in Fig. 4.20c.

The second studied etching solution was HCl. The wafers were soaked in Q_2 for 3 min, etched in HCl solution for 3 min and then rinsed in Q_2. All the etching procedure

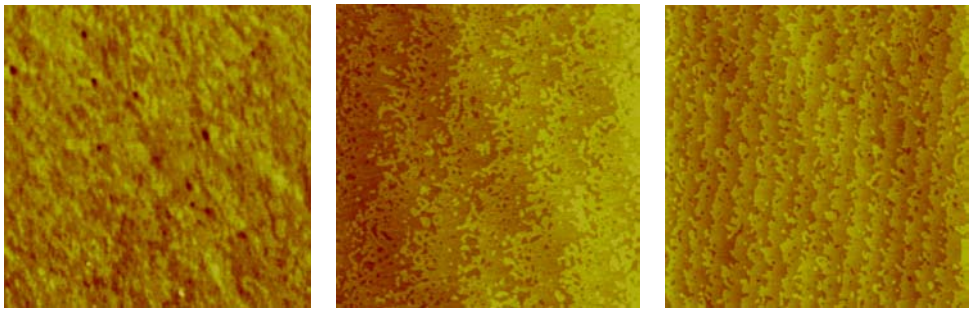

(a) *(b)* *(c)*

Fig. 4.20 *AFM of (001) LSAT etched 2 min in Aqua Regia and annealed at (a) 650 °C for 0.5 h in O_2 flow, (b) 1000 °C for 3 h in O_2 flow, and (c) 1000 °C for 36 h in O_2 flow. Scan size: (a) 2×2 μm^2, (b) 5×5 μm^2, and (c) 10×10 μm^2. The O_2 flow was set at 300 l/h.*

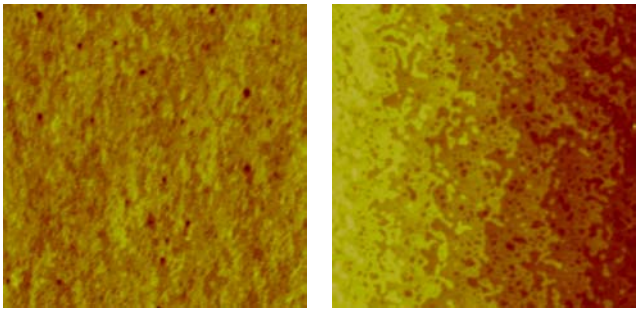

(a) *(b)*

Fig. 4.21 *AFM of (001) LSAT etched 3 min in HCl and annealed at (a) 650 °C, 0.5 h, in O_2 flow. (b) 1000 °C, 1 h, in O_2 flow. Scan size: (a) 2.5×2.5 μm^2 and (b) 2×2 μm^2. The O_2 flow was set at 300 l/h.*

steps took place in an ultrasound bath at a temperature of about 50-70 °C. The etching temperature was selected so that a complete removal of the surface $LaO_{2-\delta}/SrO_{2-\delta}$ oxides had resulted. A typical AFM image of an as-etched (001) LSAT substrate annealed at low temperature is presented in Fig. 4.21a. Etch pits can be seen, but their number is smaller and they are less deep than in the case of HCl + HNO_3 etching. After annealing at 1000 °C for 1-36 h in O_2 flow, the AFM micrograph shows a surface morphology characterized by a terraced structure with one-unit cell height steps (Fig. 4.21b).

4.4.3.3 Discussions

The surface morphology for the annealed LSAT wafers (Fig. 4.19b) and for the one etched and then annealed (Fig. 4.20b and 4.21b) is different, a possible indication of different termination layers. By considering $AlO_{2-\delta}/TaO_{2-\delta}$ as the composition of the termination layer of the etched wafers (from the chemical point of view) and from AFM data of this work, a $SrO/LaO_{2-\delta}$ termination results for the annealed LSAT at 1000 °C in

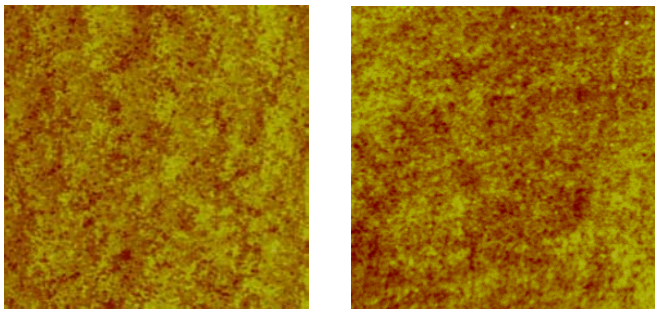

(a) *(b)*

Fig. 4.22 *Topographic AFM of (001) $SrLaAlO_4$ annealed at 650 °C, 0.5 h in (a) O_2 flow. (b) N_2 flow. Scan size: a) 3×3 μm², b) 2×2 μm². The gas flow was, in both cases, 300 l/h.*

O_2 flow. Therefore, annealing of LSAT substrates at these parameters would yield a different composition of the topmost layer than that reported in Ref. 23 (see also Table 4.2).

4.4.4 (001) $SrLaAlO_4$

As discussed in section 4.2.4, $SrLaAlO_4$ crystallize in a tetragonal K_2NiF_4-type structure consisting of perovskite-type and rock-salt layers. The Al ions in the unit cell have an octahedral coordination and form the perovskite block, while Sr and La ions have a coordination of nine forming blocks with a rock-salt structure situated between the AlO_6 layers. Taking into account these structural aspects of the $SrLaAlO_4$ crystal, a surface preparation method has to consider the difference in chemical properties (e.g., reactivity with varies solutions) and thermal stability of the constituent oxides.

4.4.4.1 Thermal treatment

It is expected that surface structural changes to take place in association with oxygen deficiencies on the surface, resulting in different morphology when annealing in an oxidizing or reducing environment. Of course, surface temperature is another factor that can determine the actual surface oxygen network. The formation of different surface morphologies for $SrLaAlO_4$ wafers annealed in O_2 or N_2 flow under the same conditions (650 °C, 0.5 h and a flow of 300 l/h) is shown in Fig. 4.22a (O_2) and 4.22b (N_2). Even at these (relatively low) temperatures an increased surface mobility can be observed for annealing in oxygen environment, with formation of atomically flat terraces of 5.7-8.5 Å in height. This indicates a surface with mixed termination. A rougher surface with no defined terraced structure resulted after annealed in N_2 flow, an indication of lower surface mobility due, possibly, a change in composition of the topmost layer, the Al-O bond being unstable[59] at these annealing conditions. Oxygen evolution from the Al-O plane upon heating would render this bond unstable and, as a result, an increased annealing temperature would decrease the mixed character of the topmost layer by removing the AlO_x plane. Considering the above observations, a difference on surface structure is expected if annealing takes place in air or oxygen, as

shown by the AFM results (see Fig. 4.23 and 4.24). An atomically smooth $SrLaAlO_4$ surface, with well-defined terraces, can be obtained by annealing in air for 1.5 h at 850 °C (see, e.g., Fig. 4.23). The main step height is about 5.7 Å, corresponding to the thickness of half structural unit (or one chemical formula unit). However, terraces with height of ¼-¾uc, as well as pits of ~ 2.5 nm can be observed. These results may be explained by the heating rate (too fast), which leads to (only) partial removal of the AlO_x from the surface. If this conclusion is valid, a slower heating rate should eliminate or reduce the formation of the pits. The formation of these pits could be avoided by oxygen annealing (850 °C, 1.5 h, see Fig. 4.24a) but, due to increased stability of AlO_x in oxygen environment, a surface with a mixed termination have resulted, as shown by friction mode AFM (Fig. 4.24b). The resulted surface shows steps of ~ 5.7 Å height, corresponding to one formula unit. When annealing in O_2 was performed at higher temperature (e.g., 950 °C), surface steps with height corresponding to c-axis of $SrLaAlO_4$ also formed.

4.4.4.2 Chemical etching

Several NH_4Cl + HCl solutions with different pH values (i.e., pH = 1-5.5) have been used for etching experiments. The procedure followed the steps described above, i.e., soaking in water, etching, rinsing in water and annealing. After ~ 5 min soaking in O_2, the samples were etched for different time intervals (from 30 s up to 10 min), depending on the etchant pH. The annealing step was performed at temperatures of 800-950 °C, in air or O_2 flow. After etching and annealing, all investigated substrates display a rough surface with etched pits, the actual surface morphology strongly depending on the etchant pH. However, even for the weaker etching solution used (e.g., pH = 5.5), the AFM observations indicate a rough surface morphology. In Fig. 4.25 the results of etching (1 min in a pH = 5 solution) on a $SrLaAlO_4$ wafer is shown. The average peak-to-valley distance is ~ 1nm, but no terraced structure can be observed. The result of the etching experiments can be explained by a wrong approach of the etching procedure. One has to consider the difference in chemical reactivity of the constituent oxides, i.e., NH_4Cl + HCl solution easily removes $LaO_{1+\delta}$[vii], while the reactivity of SrO with the etching solution is much lower and $AlO_{1+\delta}$ does not react with it. Therefore, an etching procedure for $SrLaAlO_4$ substrates has to consider the difference in chemical reactivity not only between the surface $SrO/LaO_{1+\delta}$ and $AlO_{1+\delta}$, but also between SrO and $LaO_{1+\delta}$. Here, a three steps method is proposed for chemical etching of $SrLaAlO_4$ substrates:

1. removal of La_2O_3 from the surface by using a weak NH_4Cl + HCl solution;
2. removal of SrO from the surface with a commercial BHF solution;
3. surface recrystalization through annealing.

This method is currently under investigation.

[vii] La_2O_3 is soluble in mineral acids.

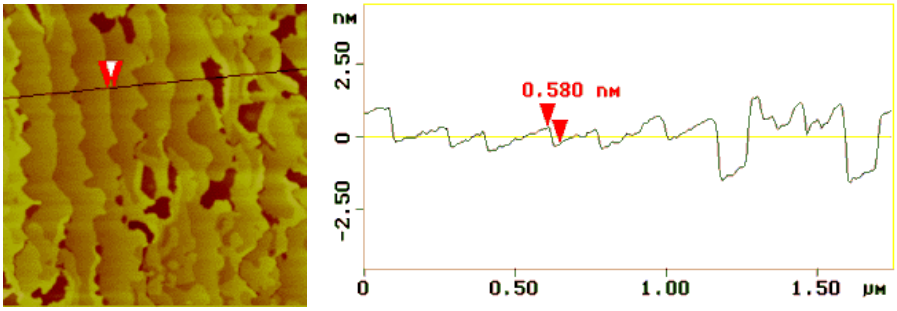

Fig. 4.23 *Topographic AFM and scan line profile of an (001) $SrLaAlO_4$ wafer annealed for 1.5 h at 850 °C in air. Scan size 1.75×1.75 µm².*

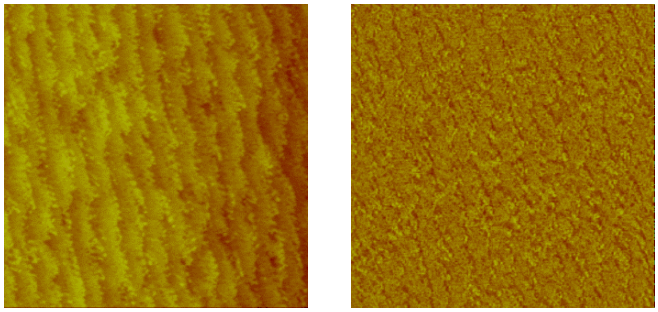

(a) *(b)*

Fig. 4.24 *(001) $SrLaAlO_4$ annealed 1.5 h at 850 °C in O_2 flow (200 l/h). (a) topographic AFM, (b) LFM of (a), indicating a surface with a mixed termination. Scan size 2×2 µm².*

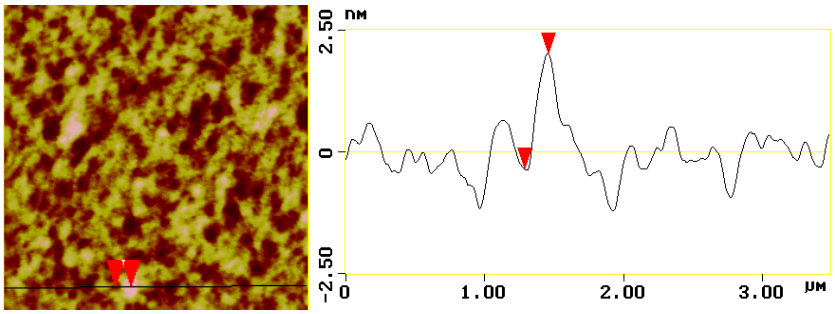

Fig. 4.25 *Topographic AFM of (001) $SrLaAlO_4$ etched for 1 min in NH_4Cl + HCl solution (pH = 5) and subsequently annealed at 850 °C for 1 h in O_2 flow (200 l/h).*
Scan size 3.5×3.5 µm².

4.4.4.3 Discussions

Optimisation of the annealing procedure for (001) $SrLaAlO_4$ substrates has to consider the heating speed and the atmosphere in which the treatment is done. Annealing in air at optimum conditions can make possible yielding of $SrLaAlO_4$ substrates with an atomically smooth surface suitable for today technology.

An important structural feature of $SrLaAlO_4$ substrates that have to be taking in account when consider thermal or chemical treatment is the high difference in physical and chemical properties of the constituent oxides (SrO, La_2O_3, and AlO_x). From these three components, the AlO_x has the most unstable oxygen network (Al-O bond), a characteristic that can be used to selectively remove it during surface preparation treatments. Oxygen annealing gives the best results from the point of view of surface morphology, while chemical treatment has to be optimised in order to produce acceptable results.

4.4.5 (001) $KTaO_3$

For $KTaO_3$, the results of thermal and chemical treatments will be determined mainly by the properties of the K-O surface. K_2O is readily soluble in mineral acids, but also in organic solvents (i.e., ethanol). On the other hand, Ta-O surface is much stable, thermally and chemically. The choice of a particular surface treatment method has to consider these structural properties.

4.4.5.1 Thermal treatment

The surface morphology of the as-received substrates is governed by polishing defects and, therefore a rough surface may result. This is demonstrated in Fig. 4.26a where the surface morphology of an as-received (001) $KTaO_3$ is shown. No surface treatments were applied. The corresponding RHEED pattern is characterized by weak streaks. Cleaning of the substrate in organic solvents (chloroform, acetone, and ethanol) followed by a short annealing step al low temperature (500 ^oC) resulted in formation of deep pits (see Fig. 4.26b) due to local removal of K_2O through reaction with ethanol. Ta_2O_3 is removed by lift off. RHEED data showed that vacuum annealing of this surface at 550 ^oC for 0.5 h resulted in an improved surface morphology. However, if a higher temperature (e.g., 700-800 ^oC) is used for vacuum annealing, a 3D RHEED pattern (indicated by arrows in Fig. 4.26c), corresponding to a phase with in-plane cell parameters of about 4.2 Å,[viii] could sometimes be observed. By avoiding the use of ethanol during the cleaning procedure, a surface with improved morphology was obtained, as showed by AFM observations and confirmed by the corresponding RHEED patterns (see Fig. 4.26d). In order to straighten the steps, an additional thermal treatment was performed. The substrate was annealed at a temperature of 950 ^oC for 1h in flowing O_2 (200 l/h). However, this additional treatment resulted in an increased surface roughness, as can be observed from Fig. 4.27.

[viii] The in-plane cell parameters of this phase are close to that of TaO (cubic symmetry, a = 4.422 Å, space group Fm3m), corresponding to a reduced (4^+) valence for Ta (from 5^+ in Ta_2O_5) due to vacuum annealing.

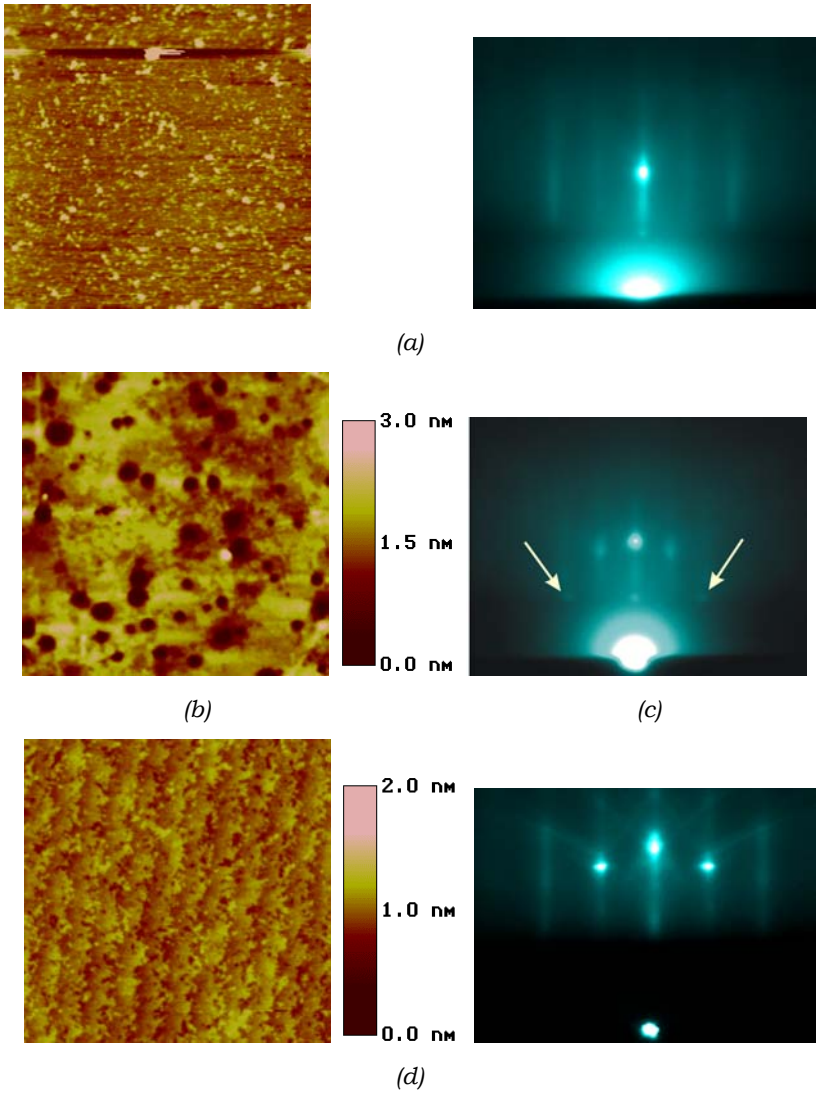

Fig. 4.26 *Topographic AFM micrographs of (001) $KTaO_3$: (a) as-received (no cleaning) and corresponding RHEED pattern (recorded at 550 °C, 0.10 mbar O_2), (b) cleaned in organic solvents (chloroform, acetone, and ethanol) and annealed 0.5 h at 500 °C in O_2 (200 l/h); (c) RHEED pattern of substrate (b) after vacuum annealing (30 min at 550 °C and 10 min at 700 °C), and (d) cleaned in organic solvents (chloroform and acetone) and annealed 0.5 h at 500 °C in O_2 (200 l/h).*
Scan size of the AFM images: (a) 3.5×3.5 μm^2, (b) 3×3 μm^2, and (d) 3×3 μm^2.

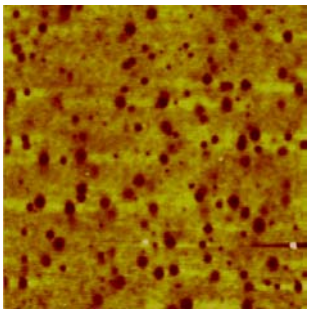

Fig. 4.27 *Topographic AFM micrograph of (001) $KTaO_3$ substrate annealed 1 h at 950 °C in O_2 flow (200 l/h). Scan size 5×5 μm^2.*

4.4.5.2 Chemical etching

A HPO_3 (1 vol%) solution was used for chemical etching. Following etching[ix], the wafers were annealed in an oxygen flow (200-400 l/h) at temperatures in range of 500 °C to 950 °C. The resulted surface morphology was similar with that of the annealed samples, as shown in Fig. 4.27. As will be discussed in Chapter 6, heteroepitaxial growth of $BaTiO_3$ (2-10 nm) can be used to further improve the surface morphology, as confirmed by RHEED data.

4.4.5.3 Discussions

The surface morphology of the chemically and/or thermally treated (001) $KTaO_3$ substrates is mainly determined by the evolution of the K-O surface. Similar morphology was obtained independent of the treatment applied, which can be explained by the chemical and physical properties of the K-O surface.

4.5 Conclusions

Several substrates (i.e., $NdGaO_3$, $SrTiO_3$, LSAT, $SrLaAlO_4$, and $KTaO_3$), with perovskite or related structure, consisting of alternating layers of $AO_{1+\delta}$ (A = Sr, La or Nd) and $BO_{2-\delta}$ (B = Ti, Al, Ta or Ga) stacked in the c direction have been used for chemical etching and annealing experiments. The aim of this study was to achieve controllable surface morphology with properties suitable for epitaxial thin film growth. These substrates were selected for their chemical and structural compatibility with the phases under investigation in this thesis (i.e., p- and n-type IL and artificially layered structures).

By considering the layered structure, selective removal of one of the surface oxides was achieved by a thermal treatment or through chemical etching, followed by annealing. The resulted surface morphology was studied *ex situ* by AFM and *in situ* by high-pressure RHEED. A-site single terminated surface can be obtained after annealing at certain conditions, while chemical etching associated with a thermal treatment can

[ix] An etching time of 5 min was used.

result in a B-site single terminated surface, free of etch pits. Vacuum annealing at high temperatures leads to generation of oxygen vacancies. The reduced surface show ordered structures due to O-vacancy ordering; e.g., a two-domain (2 × 1) structure was observed for vacuum annealed (110) $NdGaO_3$. The superstructure periodicity is absent for the surfaces chemically and/or thermally treated (in air or in O_2 flow). There is a strong dependence of the final surface morphology on the properties of the substrate (e.g., surface chemistry, vicinal angle and its orientation), on the characteristics of the etching solution, and on the annealing conditions (temperature, time, and type of ambient). This dependence suggests that the termination influences the kinetics on the surface.

References

1 J. Fompeyrine, R. Berger, H.P. Lang, J. Perret, E. Mächler, Ch. Gerber and J.–P. Locquet, *Appl. Phys. Lett.* **72**, 1697 (1998)

2 J.M. Huijbregtse, J.H. Rector and B. Dam, *Physica C* **351**, 183 (2001)

3 G. Koster, B.L. Kropman, A.J.H.M. Rijnders, D.H.A. Blank and H. Rogalla, *Mater. Sci. Eng.* **B56**, 209 (1998)

4 G. Koster, G. Rijnders, D.H.A. Blank and H. Rogalla, *Physica C* **339**, 215 (2000)

5 A.J.H.M. Rijnders, *The initial growth of complex oxides: study and manipulation*, PhD thesis ISBN 9036516579, University of Twente, The Netherlands (2001)

6 see, e.g., R. Guo, A.S. Bhalla, L.E. Cross and R. Roy, *J. Mater. Res.* **9**, 1644 (1994); J.M. Phillips, *J. Appl. Phys.* **79**, 1829 (1996) and references therein

7 I.N. Chan, D.C. Vier, O. Nakamura, J. Hasen, J. Guimpel, S. Schultz and I.K. Schuller, *Bull. Am. Phys. Soc.* **37**, 481 (1992)

8 Single crystal (001) $SrTiO_3$, (001) and (110) $NdGaO_3$, (001) LSAT, (001) $LaAlO_3$, (001) $KTaO_3$ and (001) $SrLaAlO_3$ substrates have been used in this study. Except for $KTaO_3$ and LSAT, they were produced by ESCETE, Single Crystal Technology B. V., NL-7547 RD, Enschede, The Netherlands, and were one side mechano-chemically polished, with the misorientation of the surface with respect to (001) or (110) crystal plane of 0.02-0.5°. The LSAT single crystals were supplied by Bell Labs). The value of the miscut angle was determined by XRD or by AFM (from the ratio of step height and terrace width)

9 M. Kawasaki, K. Takahashi, T Maeda, R. Tsuchiya, M. Shinohara, O. Ishiyama, T. Yonezawa, M. Yoshimoto and H. Koinuma, *Science* **226**, 1540 (1994); M. Kawasaki, A. Ohtomo, T. Arakane, K. Takahashi, M. Yoshimoto and H. Koinuma, *Appl. Surf. Sci.* **107**, 102 (1996)

10 M. Lippmma, K. Takahashi, A. Ohtomo, S. Ohashi, T. Ohnishi, N. Nakagawa, T. Sato, M. Iwatsuki, H. Koinuma and M. Kawasaki, Mater. *Sci. Eng. B* **56**, 111 (1998)

11 G. Koster, B.L. Kropman, G.J.H.M. Rijnders, D.H.A.Blank and H. Rogalla, *Appl. Phys. Lett.* **73**, 2920 (1998)

12 G. Koster, *Artificially layered oxides by pulsed laser deposition*, PhD thesis ISBN 9036513367, University of Twente, The Netherlands (1999)

13 L.X. Cao, J. Zegenhagen, E. Sozontov and M. Cardona, *Physica C* **337**, 24 (2000)

14 See, e.g., R.L. Sandstrom. E.A. Giess, W.J. Gallagher, A. Segmüler, E.I. Cooper, M.F. Chisholm, A. Gupta, S. Shinole and R.B. Laibowitz, *Appl. Phys. Lett.* **53**, 1874 (1988); D. Schweitzer, T. Bollmeier, B. Stritzker and B. Rauschenbach, *Thin Solid Films* **280**, 147 (1996); D.H.A. Blank, A.J.H.M. Rijnders, F.J.G. Roesthuis, G. den Ouden and H. Rogalla, *Appl. Surf. Science* **96-98**, 685 (1996)

15 B. Dam, J. Rector, R. Surdeanu, R.J. Wijngaarden, G. Koster, F. Peerdeman, J. van Berkum, D.G. de Groot and R. Griessen, *Physica C* **282-287**, 665 (1997); J. Rector, P. Koster, F. Peerdeman, D.G. de Groot and B. Dam, *J. Alloys and Compounds* **251**, 114 (1997)

16 Y. Sun, J.D. Guo, X.L. Xu, G.J. Lian, Y.Z. Wang and G.C. Xiong, *Physica C* **312**, 197 (1999); C. Klemenz, I. Utke and H.J. Scheel, *J. Cryst. Growth* **204**, 62 (1999)

17 R. Unger, T.A. Scherer, W. Jutzi, Z.G. Ivanov and E.A. Stepantsov, *Physica C* **241**, 316 (1994); Y.Y. Divin, H. Schulz, U. Poppe, N. Klein, K. Urban, P.M. Shadrin, I.M. Kotelyanskii and E.A. Stepantsov, *Physica C* **256**, 149 (1996)
18 G. Balestrino, R. Desfeux, S. Martellucci, A. Paoletti, G. Petrocelli, A. Tebano, B. Mercey and M. Hervieu, *J. Mater. Chem.* **5**, 1879 (1995)
19 X.T. Zeng and H.K. Wong, *Appl. Phys. Lett.* **66,** 3371 (1995); X.T. Zeng, H.K. Wong, J.B. Xu and I.H. Wilson, *Appl. Phys. Lett.* **67**, 3272 (1995); L. Kebin, Q. Zhenzhong, L. Xijun, Z. Jingsheng and Z. Yuheng, *Thin Solid Films* **304**, 386 (1997)
20 V.V. Mamutin, A.A. Toropov, N.F. Kartenko, S.V. Ivanov, A. Wagner and B. Monemar, *Mater. Sci. Eng. B* **59**, 56 (1999)
21 S. Madhavan, J.A. Mitchell, T. Nemoto, S. Wozniak, Y. Liu, D.G. Schlom, A. Dabkowski and H.A. Dabkowska, *J. Cryst. Growth* **174**, 417 (1997)
22 L. Vasylechko, L. Akselrud, W. Morgenroth, U. Bismayer, A. Matkowskii and D. Savytskii, *J. Alloys Comp.* **297**, 45 (2000)
23 T. Ohnishi, K. Takahashi, M. Nakamura, M. Kawasaki, M. Yoshimoto and H. Koinuma, *Appl. Phys. Lett.* **74**, 2531 (1999)
24 C. Kwon, Qi Li, X.X. Xi, S. Bhattacharya, C. Doughty, T. Venkatesan, H. Zhang, W. Lynn, J.L. Peng, Z.Y. Li, N.D. Spencer and K. Feldman, *Appl. Phys. Lett.* **62**, 1289 (1993); G. Liu, H. Wang, H. Makino, H.-J. Ko, T. Hanada and T. Yao, *J. Cryst. Growth* **227-228**, 960 (2001)
25 G. Shirane and Y. Yamada, *Phys. Rev.* **177**, 858 (1969)
26 J. Padilla and D. Vanderbilt, *Surf. Sci.* **418**, 64 (1998)
27 S.P. Chen, *J. Mater. Sci.* **13**, 8148 (1998)
28 R. Sum, H.P. Lang and H.–J. Güntherodt, *Physica C* **242**, 174 (1995)
29 S. Watanabe, T. Hikita and M. Kawai, *J. Vac. Sci. Technol. A* **9**, 2394 (1991)
30 M. Kawai, Z.Y. Liu, T. Hanada, M. Katayama, M. Aono and C.F. McConville, *Appl. Surf. Sci.* **82-83**, 487 (1994)
31 T. Hikita, T. Hanada, M. Kudo and M. Kawai, *J. Vac. Sci. Technol. A* **11**, 2649 (1993)
32 S.C. Tidrow, A. Tauber, W.D. Wilber, R.T. Lareau, C.D. Brandle, G.W. Berkstresser, A.J. Ven Graitis, D.M. Potrepka, J.I. Budnick and J.Z. Wu, *IEEE Trans. Appl. Supercond.* **7**, 1766 (1997)
33 B.C. Chakoumakos, D.G. Schlom, M. Urbanik and J. Luine, *J. Appl. Phys.* **83**, 1979 (1998); Y. Li, X.J. Wu, J.G. Wen, Y. Takahashi and K. Tanabe, *J. Appl. Phys.* **87**, 3707 (2000)
34 V.G. Hadjiev, M. Cardona, I. Ivanov, V. Popov, M. Gyulmezov, M.N. Iliev and M. Berkowski, *J. Alloys Comp.* **251**, 7 (1997)
35 R. Brown, V. Pendrick, D. Kalokitis and B.H.T. Chai, *Appl. Phys. Lett.* **57**, 1351 (1990)
36 R. Sobolewski, P. Gierowski, W. Kula, S. Zarembinski, S. Lewandowski, M. Berkowski, A. Pajaczkowska, B.P. Gorshunov, D.B. Lyudmirsky and O.I. Sirotinski, *IEEE Trans. Magn.* **27**, 876 (1991)
37 C. Le Paven-Thivet, M. Guilloux-Viry, J. Padiou, A. Perrin, M. Sergent, L.A. de Vauchier and N. Bontemps, *Physica C* **244**, 231 (1995)

38 J.–P. Locquet, J. Perret, J. Fompeyrine, E. Machler, J.W. Seo and G. Van Tendeloo, *Nature* **394**, 453 (1998)
39 T. Manako, Y. Okimoto, M. Izumi, S. Shinomori, M. Kawasaki, T. Fukumura, M. Ohtani and Y. Tokura, *Appl. Phys. Lett.* **79**, 1754 (2001)
40 R.W. Mosses, J.-P.R. Welles, H.G. Gallagher, T.P.J. Han, M. Yamaga, N. Kodama and T. Yosida, *Chem. Phys. Lett.* **286**, 291 (1998)
41 G.K.L. Goh, V.G. Levi and F.F. Lange, *J. Mater. Res.* **17**, 2852 (2002)
42 R. Feenstra, L.A. Boatner, J.D. Budai, D.K. Christen, M.D. Galloway and D.B. Poker, *Appl. Phys. Lett.* **54**, 1063 (1988); S.K. Patapis. E.C. Jones, J.M. Phillips, D.P. Norton and D.H. Lowndes, *Physica C* **244**, 198 (1995)
43 O.G. Vendik, E.K. Hollmann, A.B. Kozyrev and A.M. Prudan, *J. Superconductivity* **12**, 325 (1999); S. Karimoto, K. Ueda, M. Naito and T. Imai, *Appl. Phys. Lett.* **79**, 2767 (2001)
44 T. Greibe, M. Hepp and M. Naito, *Physica C* **372-376**, 1082 (2002); M. Naito, S. Karimoto and A. Tsukada, *Supercond. Sci. Technol.* **15**, 1663 (2002)
45 H.M. Christen, L.A. Boatner, J.D. Budai, M.F. Chisholm, L.A. Gea, P.J. Marrero and D.P. Norton, *Appl. Phys. Lett.* **68**, 1488 (1996)
46 A. Meldrum, L.A. Boatner, W.J. Weber and R.C. Ewing, *J. Nuclear Materials* **300**, 242 (2002)
47 H. Vogt, *Phys. Rev. B* **41**, 1184 (1990); H. Vogt, *J. Phys. Condens. Matter.* **3**, 3697 (1991); M.D. Glinchuk, V.V. Laguta, I.P. Bykov, J. Rosa and L. Jastrabik, *Chem. Phys. Lett.* **232**, 232 (1995)
48 A. Ikeda, T. Nishimura, T. Morishita and Y. Kido, *Surf. Sci.* **433-435**, 520 (1999)
49 G. Rijnders, G. Koster, D.H.A. Blank and H. Rogalla, *Appl. Phys. Lett.* **70**, 1888 (1997); D.H.A. Blank, G.J.H.M Rijnders, G. Koster and H. Rogalla, *Appl. Surf. Sci.* **127-129**, 633 (1998); D.H.A. Blank, G.J.H.M Rijnders, G. Koster and H. Rogalla, *Appl. Surf. Sci.* **138-139**, 17 (1999)
50 See, e.g., G. Rijnders, G. Koster, V. Leca, D.H.A. Blank and H. Rogalla, *Appl. Surf. Sci.* **168**, 223 (2000)
51 G. Koster, G. Rijnders, D.H.A. Blank and H. Rogalla, *Appl. Phys. Lett.* **74**, 3729 (1999); D.H.A. Blank, G. Koster, G. Rijnders, E. van Setten, P. Slycke and H. Rogalla, *Appl. Phys. A* **69**, S17 (1999); D.H.A. Blank, G. Koster, A.J.H.M. Rijnders, E. van Setten, P. Slycke and H. Rogalla, *J. Cryst. Growth* **211**, 98 (2000)
52 N. Bickel, G. Schmidt, K. Heinz and K. Mueller, *Phys. Rev. Lett.* **62**, 2009 (1989)
53 T. Hikita, T. Hanada and M. Kudo, *Surf. Sci.* **287-288**, 377 (1993)
54 J. Prade, U. Schroeder, W. Kress, F.W. de Wette and A.D. Kukarni, *J. Phys. Condensed. Mater.* **5**, 1 (1993)
55 see, e.g., N. Erdman, K.R. Poeppemeler, M. Asta, O. Warschkow, D.E. Ellis and L.D. Marks, *Nature* **419**, 55 (2002)
56 M.G. Norton, S.R. Summerfelt and C.B. Carter, *Appl. Phys. Lett.* **56**, 2246 (1990)
57 The complex processes from the HF + NH_4F + H_2O system are presented in detail in, e.g., H. Kikyuama, N. Miki, K. Saka, J. Takano, I. Kawanabe, M. Miyashita and T. Ohmi, *IEEE Trans. Semicond. Manufact.* **4**, 26 (1991); H. Kikuyama, M. Waki, M. Miyashita, T. Yabune, N. Miki, J. Takano and T. Ohmi, *J. Electrochem. Soc.* **141**, 366 (1994)

58 V. Leca, G. Rijnders, G. Koster, D.H.A. Blank and H. Rogalla, *Mat. Res. Soc. Symp.* **587**, O3.6.1 (2000)
59 J. Yao, P.B. Merrill, S.S. Perry, D. Marton and J.W. Rabalais, *J. Chem. Phys.* **108**, 1645 (1998)
60 R.F. Belt and R. Uhrin, *Science and Technology of Thin Film Superconductors*, R.D. McConnell and S.A. Wolf, Edt (Plenum, New York), 353 (1989)
61 I. Utke, C. Klemenz, H.J. Scheel and P. Nüesch, *J. Cryst. Growth* **174**, 813 (1997); W. Marti, P. Fischer, F. Altorfer, H.J. Scheel and M.J. Tadin, *Phys. Condens. Matter.* **6**, 127 (1994)
62 R.D. Shannon, R.A. Oswald, J.B. Parise, B.H.T. Chai, B. Byszewski, A. Pajaczkows kand R. Sobolewski, *J. Solid. State Chem.* **98**, 90 (1992); A. Pajaczkowska and P. Byszewski, *J. Cryst. Growth* **128**, 694 (1993)
63 M.R. Castell, *Surf. Sci.* **505**, 1 (2002)

Chapter 5

(Ba,Sr,Ca)CuO_2 artificial superlattices

5.1 Introduction

In search for new high-T_c superconducting materials, high-pressure synthesis methods are used for the synthesis of new series of layered cuprate superconductors. One of these is the $CuBa_2Ca_{n-1}Cu_nO_{2n+2+\delta}$ homologous series,[1] with T_c's as high as 125 K. The chemical advantage of these phases is the lack of toxic elements, like in Tl or Hg-based HTSc. As discussed in Chapter 2, the main drawback of the bulk high-pressure synthesis is the difficulty in controlling the doping, impurity or oxygen level, all influencing the final properties of the synthesised compounds. Advances in thin film growth techniques and in the understanding of epitaxial thin-film growth of cuprates make these techniques very promising as potential tool for the synthesis of new metastable phases and an alternative to the bulk methods.[2] Making use of the stabilization effect of the substrate, epitaxial films of metastable structures, such as 'infinite layer' phases and $(Ba,Sr)CuO_2/(Sr,Ca)CuO_2$ artificially layered superlattices, have been grown as single-crystal thin films by means of MBE or PLD.[3-9]

In thin film growth, apart from the deposition parameters, the choice of substrate was shown to be of great importance. In order to stabilize metastable structures as thin films, the in plane lattice parameters of the substrate has to be compatible with the expected one of the film, while the substrate surface morphology has to be well defined. Therefore, $SrTiO_3$ was so far the substrate of choice for growing infinite layer phases and their superlattices. On the other hand, considering the value of the a-axis parameter[3] for the tetragonal $CuBa_2Ca_{n-1}Cu_nO_{2n+2+\delta}$ phases (a ~ 3.85-3.87 Å) a better lattice match is expected with, e.g., $NdGaO_3$ substrates. In Chapter 4 it was shown that vicinal $NdGaO_3$ substrates could be chemically or thermally treated to give a perfect template for thin film growth. One of the questions that arise from the use of this substrate is if $BaCuO_x$ phase can be stabilize in its tetragonal symmetry.

PLD has become one of the most versatile and useful thin-film growth techniques, particularly for multi-component materials, such as high-T_c cuprate superconductors. When growing artificially engineered layered structures based on infinite layer compounds, random thickness fluctuations may be present[6,10] and, therefore, must be controlled through a suitable deposition technique, such as pulsed laser deposition. Furthermore, an in situ surface diagnostic tool such as high-pressure RHEED can be used to monitor the growth at the high pressures (~ 10^{-2}-0.90 mbar O_2) required to stabilize these structures, when molecular oxygen is used as oxidant[4,9]

In this Chapter, the results of pulsed laser interval deposition (PLiD) and properties of infinite layers $ACuO_2$ (A = Ba, Sr, Ca) and $(Ba,Sr)CuO_2/(Ca,Sr)CuO_2$ superlattice thin films grown on (001) or (110) $NdGaO_3$ substrates will be presented. The questions that we will try to answer regard the stability of phases such as $BaCuO_x$ on $NdGaO_3$; if the expected increase of phase stability of the infinite layer compounds and $(Ba,Sr)CuO_2/(Ca,Sr)CuO_2$ superlattice takes place; what is the influence of the (increased) compressive strain (compared to the use of $SrTiO_3$ substrates) on the final electrical properties of the films. For $BaCuO_x$ grown on $SrTiO_3$ it was shown that the stable deposition block consists of two unit cells[9,11] Is this also valid when $NdGaO_3$ is used as atomic template? All these will be addressed in this chapter and, if possible, answered.

5.2 Structural properties

The possibility of tailoring artificial cuprate structures has allowed the study of the correlation between structural features and superconducting properties in these complex materials. Using deposition techniques such as PLD it is possible to realize artificial multilayered structures, whose growth is kinetically stabilized, since the constituents are supplied in sequence.[4,11] Such artificial materials can be a powerful means to investigate the conduction mechanisms in HTSc. The layered structure of these compounds, made of stacked CuO_2 planes, supplied by the IL blocks, and charge reservoir CR blocks, can be simulated by deposition of superlattices made by alternatively stacking different phases that can act as CR and IL, respectively.[2-4,6-9,11-19] The CR blocks, structurally compatible with the copper planes, should contain a large amount of charge and one of the most effective ways of introducing charge carriers is oxygen doping.[16] $BaCuO_2$, though being a very unstable IL structure,[7-9,11,17] can easily incorporate excess oxygen in the Ba-plane (forming $BaCuO_{2+\delta}$ blocks, see Fig. 5.1) and, therefore, can act as a CR block for the IL block(s) (here, $SrCuO_2$ and/or $CaCuO_2$) that supplies the CuO_2 planes.

Relatively high oxygen deposition pressures (0.2-0.9 mbar O_2)[4,7] are used in order to obtain the required concentration of excess oxygen for superconductivity in $ACuO_2$-based superlattices. The optimally doped $(BaCuO_x)_2/(CaCuO_2)_2$ superlattices grown on $SrTiO_3$ have a T_c onset of ~ 80 K. For the Ba and Sr-based structures, a maximum T_c onset of 70 K was obtained for $(BaCuO_x)_2/SrCuO_2$ superlattices by Norton *et al.*[4] These values are somewhat lower than what would be expected for a cuprate superconductor containing 3-4 CuO_2 planes.[1] Two possible reasons for a decreased value of T_c are generally considered:[18] a) a high degree of disorder and b) a not optimised structure of

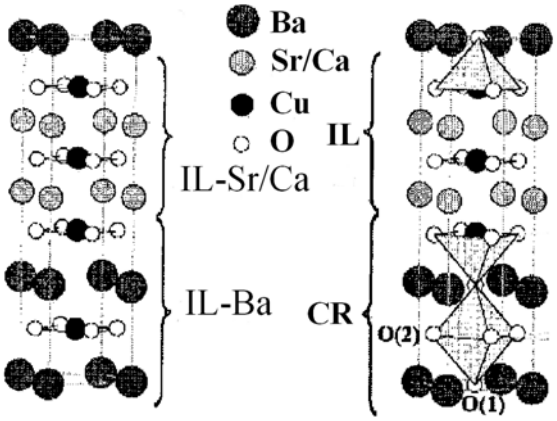

(a) *(b)*

Fig. 5.1 *Schematic representation of the 2×$(BaCuO_2)_2$/2×(Sr,Ca)CuO_2 unit cell for (a) nonsuperconducting and (b) superconducting superlattices. IL-Ba and IL-Sr/Ca indicate the Ba and Sr or Ca-based infinite layer blocks, respectively. CR indicates the charge reservoir block (from Ref. 4).*

the CR layer(s). The structural disorder is more effective for thin IL blocks (e.g., one or two $CaCuO_2$ layers), strongly reduced for superlattices with thick IL blocks, and negligible for the thickest ones.[18] A decrease of carrier concentration per CuO_2 plane is expected with increased thickness of IL block (the charge carriers are considered to be distributed homogeneously along the c-axis).[18] The decrease of T_c in superlattices with very thin constituent layers are generally ascribed to a decrease of the mean free path caused by the disorder at the interfaces between the CR and IL blocks. By decreasing the number of $CaCuO_2$ unit in the IL block to a minimum of one, the role of the disorder at the interface becomes dominant driving the system toward insulating regime.[19]

Different structural-defect models were studied by Balestrino *et al.*[20] for $[(BaCuO_{2+x})_m/(CaCuO_2)_n]_N$ or BCCO superlattices with n varied between 2 and 3 (the models are also valid for other superlattices, such as $[(BaCuO_{2+x})_m/(SrCuO_2)_n]_N$ or BSCO). By X-ray spectra simulations they have demonstrated that, for these superlattices, a 2D layer-by-layer growth can be achieved. During growth, in case of formation of a mixed composition layer, the 2D growth starts with the first constituent oxide and is completed, still in a 2D mode, by the second constituent. The mixed layers will consist, therefore, of small regions of different compositions. In situ RHEED measurements showed no sizeable deterioration of the surface during the deposition, while HRTEM analyses showed that the quality of the layers close to the physical surface of the film is comparable with the one of the first layer. They suggested that in each mixed composition block(s), the atomic layers are distorted to avoid sharp steps, however such distortion is not enough to establish a constant thickness throughout the deposited layer. Simulated spectra fitted the XRD experiments better if the structure of

the $BaCuO_{2+x}$ block was maintained during growth. Furthermore, an experimental dispersion in the amount of material deposited in each sequence was necessary to be taken in account in order for the simulated spectra to accurately reproduce the experimental peak widths.

The competition between the presence of random disorder and the decrease of the number of holes per CuO_2 plane was considered to be the reason for the experimental values of maximum T_c in samples with a number n of CuO_2 of $2 < n < 2.5$ (and not for samples with n integer number). Ordered superconducting CuO_2 planes are necessary to allow the development of the superconductivity in these artificial superlattices,[20] but coupling between successive IL conducting blocks was found *not* to be strictly necessary for superconductivity in these structures.[21] For example, T_c values as high as 55 K could be obtained in superlattices where successive $CaCuO_2$ bi-layers were separated by giant CR blocks (made of up to 11 layers of $BaCuO_x$). This result is expected in view of the interlayer spacing, which is much larger than that of the coherence length typical of HTS materials.[21] On the other hand, critical for appearance of superconductivity in these structures is the stoichiometry of the IL layers, which should not contain any cation mixing from the CR blocks.[21] A single (and complete) IL layer, sandwiched between two CR blocks, is considered to be the minimal structural requirement for superconductivity to occur in the $ACuO_2$-based superlattices.[14]

The presence of the excess oxygen in the Ba-planes (see Fig. 5.1) needed for superconductivity can cause instability due to the strong charge unbalance that cannot be tolerated by the structure, since superlattices tend to keep their charge neutrality.[4] Consequently, during growth the quantity of oxygen that can be introduced into the Ba layer will be limited by this structural consideration. One solution of decreasing this unbalance was found to be the partial doping (max. 10 %) of Ba sites with trivalent La or Nd ions, leaving unchanged the CuO_2 planes where the conduction occurs.[12,13] By using this substitution an increase of thermodynamic stability of the $BaCuO_x$ blocks was obtained; an increase of oxygen content in Ba-layers is also expected (due to a higher coordination number of La or Nd).[12,13] La-doped BCCO superlattices showed a maximum T_c of 70 K, comparing with the T_c of 80 K for the undoped BCCO structures. Hall measurements showed a carrier density of 0.18 holes per CuO_2 plane, which corresponds with optimum doping, the same value being found in the undoped superlattices. Since substitution of divalent Ba ions with trivalent ions decreases the total charge in the unit cell, the value of the carrier density indicates that more oxygen was introduced into the structure by this type of substitution. For higher La doping, even the concentration of the charge carriers was found the same,[12,13] structural disorder induced by difference in Ba and La size resulted in destroying the superconductivity.

When in situ diagnostic techniques, such as RHEED, cannot be used for monitoring the growth, one-dimensional kinematic XRD analysis based on the method developed by Fullerton *et al.*[22] was often used to analyse the structure. The model considers the fluctuations from the average structure, allowing a quantitative determination of disorder in superlattices. It has been successfully applied in the past to systems such as metals, semiconductors or high-T_c superconductors.[17,18,20,22,23] Several types of disorder

can be present in a superlattice, including discrete and continuous layer thickness fluctuations, amorphous layers at the interface, interlayer diffusion, strains, etc. The presence of amorphous layers at the interface is considered negligible and such disorder, in the case of IL-based structures, would lead to loss of any crystallographic order along the growth direction. Another possible origin of structural disorder is the interdiffusion of Ba-Sr or Ca-Sr that can lead to the formation of layers having mixed composition (such as $Ba_{1-x}Sr_xCuO_2$). However, for growth temperatures of about 600 °C the interdiffusion in these systems between adjacent layers was found to be negligible.[4,5] Therefore, the discrete random layer thickness fluctuations are considered as the main source of disorder in these superlattices. However, the random discrete thickness fluctuations affect essentially only one unit cell, and with a deposition technique such as PLD these types of structural defects can be avoided for optimum growth parameters. In next section, the influence of the random discrete thickness fluctuations on the final structural and electrical properties of (Ba,Sr)CuO_2/(Ca,Sr)CuO_2 artificially layered structures growth by pulsed laser interval deposition on $NdGaO_3$ substrates will be presented and discussed.

5.3 Experimental

The growth of superlattice structures by pulsed laser ablation requires a very good calibration of the growth rates of the constituent blocks. Therefore, at the start of this study we focused on the right deposition parameters for stabilizing the $ACuO_2$ (A = Ba, Sr, or Ca) phases on (001) or (110) vicinal $NdGaO_3$ substrates. A not well-defined substrate surface morphology has a significant impact on the microstructure and physical properties of the films,[11, 24] therefore the substrates were prepared prior deposition following the methods described in Chapter 4. During growth, the evolution of the film structure and surface morphology was monitored by means of in situ high-pressure RHEED. Film structure, growth orientation and lattice parameters were determined ex situ by X-ray diffraction, while films morphology was investigated by AFM, in air.

5.3.1 Infinite layers

5.3.1.1 Deposition and properties

The $ACuO_2$ infinite layers were deposited by pulsed laser interval using the settings given in Table 5.1. Typical substrate temperatures of 550-600 °C and deposition pressures varying in range of 5×10^{-2}-0.20 mbar O_2 were mainly used. Laser pulse energy in range of 30-35 mJ was used for all $ACuO_2$ compounds.

In order to be able to use PLiD, the number of pulses required for completion of one unit deposition block (typically one unit cell) had to be determined; therefore, conventional PLD was used at this stage. The growth behaviour strongly depended on the structural characteristics (e.g., in-plane cell parameters) of each deposited compound. At the initial growth stage, SCO has a 2D growth mode, with clear RHEED intensity oscillations (Fig. 5.2d). The morphology of a thin layer of SCO grown by PLD on annealed (001) $NdGaO_3$ (Fig. 5.2a) shows a terraced step structure, with the imprint

Table 5.1 *Typical deposition conditions* of the infinite layers grown by pulsed laser (interval) deposition on $NdGaO_3$ substrates.*

Compound	Target type	T_d (°C)	PO_2 (Pa)	Energy density (J/cm^2)
$CaCuO_2$ (CCO)	sintered pellet[a]	500 - 610	1 - 35	1.3 - 1.5
$SrCuO_2$ (SCO)	sintered pellet[a]	500 - 650	1 - 40	1.3 - 1.75
$BaCuO_x$ (BCO)	sintered pellet[b]	500 - 600	5 - 40	1.3 - 1.5

*for all films a substrate-target distance of d_{st} = 45 mm was used.
[a]polycrystalline, orthorhombic
[b]polycrystalline, cubic

of the substrate. At this stage the height of the terraces and of the islands formed due to incomplete coverage is about one unit cell of $NdGaO_3$. RHEED patterns recorded during the growth of the film (Fig. 5.2b and c) show the formation, for these deposition parameters, of an incommensurate structure most probably originating from cation-deficiency (probably Cu)[25] at the surface. Increasing the laser energy resulted in a decrease of the intensity or no formation of the incommensurate streaks. It is worth to mention that, while for low deposition pressures (10^{-2}-5×10^{-2} mbar O_2) PLD growth of SCO on (001) $SrTiO_3$ resulted in formation of the orthorhombic structure,[11] this behaviour was not observed when $NdGaO_3$ was used. In the deposition pressure range used for the experiments (i.e., 10^{-2}-0.40 mbar O_2), all SCO films showed a tetragonal symmetry. It can be concluded that, for SCO films, $NdGaO_3$ has a stronger stability effect than $SrTiO_3$.

For the other two $ACuO_2$ phases, the growth follows a typical Stransky-Krastanov mechanism. For CCO the transition from the layer-by-layer like to island growth takes place after some few layers (Fig. 5.3a). After this transition, RHEED patterns showed a constant decrease of the intensity with no recovery at the end of the deposition. For BCO, having the highest in plane cell parameters mismatch between film and substrate, the transition from 2D to 3D growth takes place earlier, typically after 1-3 layers, depending on the deposition pressure (a higher deposition pressure favours the transition, due to a decrease in mobility of the ad atoms). This behaviour can be explained by the existence of strain in the film that helps to stabilize the first few unit layers, followed by a relaxation of the stress, accompanied by a sharp decrease of the RHEED intensity. When an SCO buffer layer[i] is deposited prior to the growth of CCO or BCO, better-defined intensity oscillations were observed (Fig. 5.3b), similar with the behaviour of CCO or BCO on SCO/$SrTiO_3$.[11] $SrTiO_3$ can also be used as buffer layer

[i] The surface of the $SrCuO_2$ buffer layer acts as a chemical template for the nucleation and growth of $CaCuO_2$.[26]

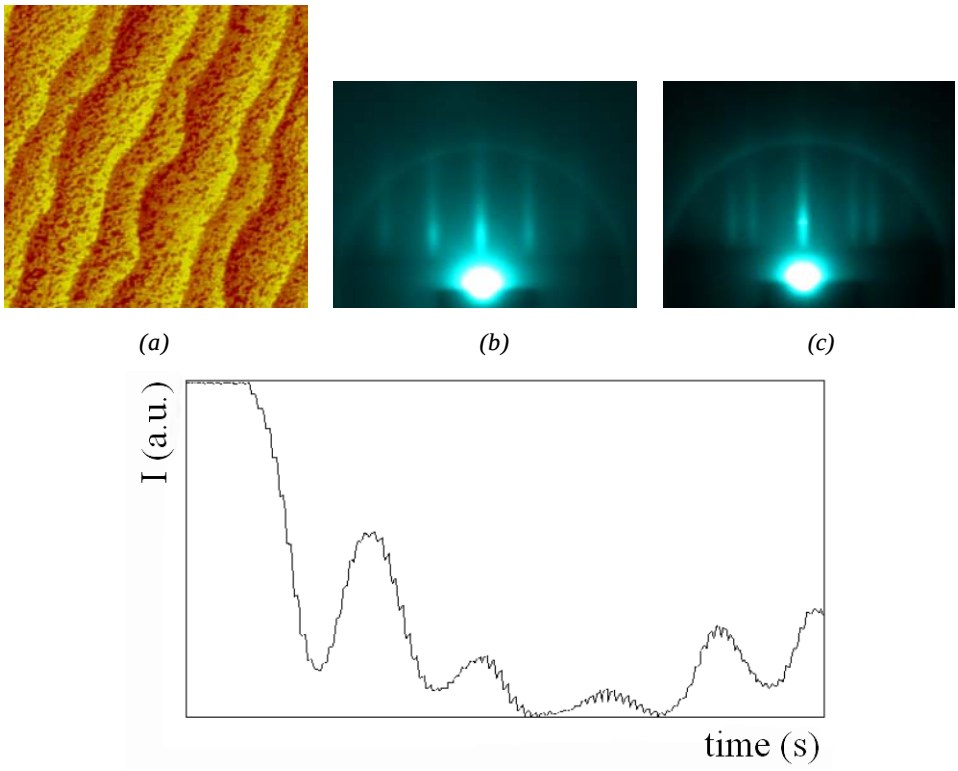

Fig. 5.2 *Surface morphology of ~ 5 unit cells $SrCuO_2$ grown by PLD on oxygen annealed (001) $NdGaO_3$ at 550 ^oC and 5×10^{-2} mbar O_2 at a deposition rate of 2Hz. (a) Topographic AFM (2×2 μm^2). RHEED patterns of the film recorded on (b) [100] and (c) [110] direction. (d) Evolution of the intensity of the RHEED specular spot.*

prior BCO deposition. Consequently, a better determination of the deposition rate could be made in this case.

The stability of $ACuO_2$ compounds grown by interval deposition was studied in order to determine the ability of forming superlattices using $NdGaO_3$ as substrates. In Fig. 5.4 and 5.5 the results of in situ RHEED and ex situ AFM analyses are depicted for very thin layers of two of the $ACuO_2$ compounds ($CaCuO_2$ and $BaCuO_2$) grown by PLiD. These data show the formation of only the tetragonal structure (RHEED data, see Fig. 5.4b and 5.5b), while AFM micrographs (Fig. 5.4a and 5.5a) indicate that by proper monitoring and controlling the growth a true layer-by-layer growth (see also Fig. 5.3c for CCO case) can be obtained for all $ACuO_2$ phases (including $BaCuO_x$).

As discussed before, tetragonal BCO is not a stable bulk phase and it can be grown only as thin films due to stabilizing effect caused by the substrate or by staking it between SCO layers.[4,7,11] When grown directly on the $NdGaO_3$ substrate by PLD, only a very thin layer of BCO could be stabilized. Using interval deposition and/or SCO as a

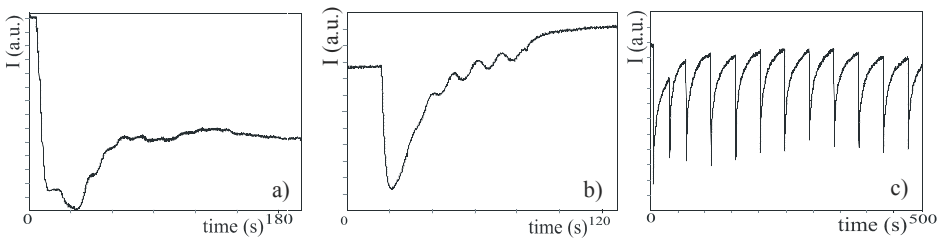

Fig. 5.3 *Intensity of the specular reflection recorded during deposition of (a) $CaCuO_2$ (f = 5Hz), (b) $CaCuO_2$ on $SrCuO_2$ buffered $NdGaO_3$ (f = 5Hz), and (c) $CaCuO_2$, all by interval deposition (f = 50 Hz). The films were deposited at 590 °C on annealed (001) $NdGaO_3$.*

buffer layer, BCO stability could be further increased. In this way, BCO thin films up to 20 nm could be grown. Nevertheless, as expected, the stability thickness of BCO on $NdGaO_3$ is smaller than when grown on $SrTiO_3$ substrate at similar deposition conditions,[11] due to somewhat better lattice match between BCO and $SrTiO_3$. When grown on $SrTiO_3$, the stability block of BCO is considered to correspond to two unit-cells.[7,11] Due to an increased compressive strain in BCO films grown on $NdGaO_3$, it may be expected that the stability unit block for very thin BCO layer to be one unit cell when PLiD is used. Indeed, when BCO was deposited by PLiD on $NdGaO_3$, the first ~ 10 uc showed the BCO unit cell as the stable deposition block. This result will be applied further to growth BCO-based superlattices with an odd number of BCO unit cells.

In Fig. 5.6 the results of surface morphology and microstructure (topographic AFM and corresponding RHEED patterns) for thick $ACuO_2$ layers (22 to 100 unit cells) grown by PLiD on (001) $NdGaO_3$ are given. As can be seen from these images, at optimum deposition parameters, thin films with smooth surface characterized by terraces step of one unit cell height can be obtained, as confirmed by AFM (Fig. 5.6a, c, and e) and RHEED data (Figs. 5.6b, d, and f). The corresponding θ - 2θ X–ray diffraction scans for $(Sr,Ca)CuO_2$ layers are given in Fig. 5.7. The XRD data showed that the films are epitaxial, with c-axis oriented perpendicular to the substrate surface. The c-axis parameters of the films were determined from the (00l) reflections and were found to be 3.196 Å, 3.449 Å, and 4.454 Å for CCO, SCO, and BCO, respectively. These values are similar with the results of the c-axis parameters for the corresponding films grown on $SrTiO_3$.[11]

All $ACuO_2$ films showed semiconducting behaviour with decreasing temperature, with high resistance at room temperature (see, e.g. Fig. 5.12a for RT curve of a $SrCuO_2$ film). The resistivity decreases from CCO to BCO, the BCO films showing the lowest values of resistivity most probably due to incorporation of extra oxygen in the Ba-plane. For all films the resistance could be decreased by increasing deposition pressure or by post-deposition annealing, in situ or ex situ, at temperatures in range of 350-500 °C, under high oxygen pressure. The semiconducting character remained; no trace of

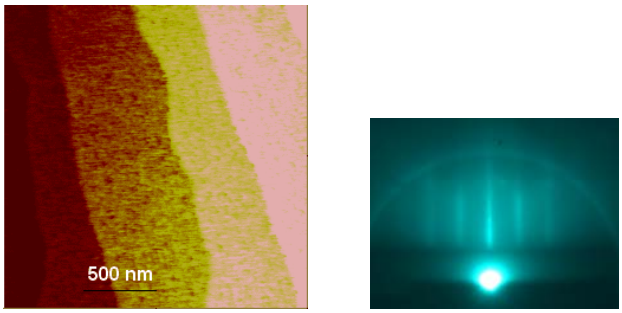

(a) *(b)*

Fig. 5.4 *Surface morphology of 12 unit cells $CaCuO_2$ grown by PLiD at 610 °C, 0.10 mbar O_2 at a deposition rate of 50 Hz on oxygen annealed (001) $NdGaO_3$. (a) Topographic AFM (2×2 μm^2). (b) RHEED pattern of the film (recorded on [100] direction).*

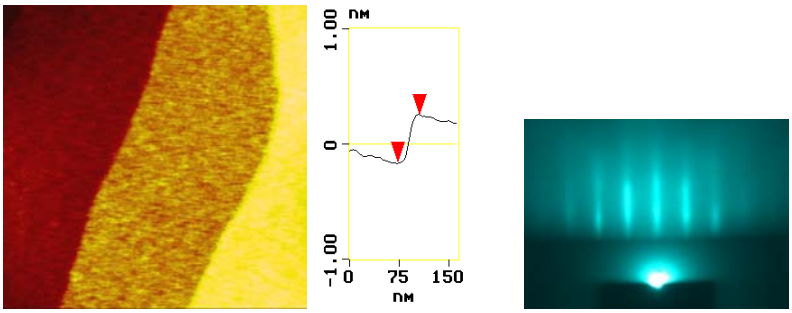

(a) *(b)*

Fig. 5.5 *Surface morphology of ~ 5 unit cells $BaCuO_x$ grown by PLiD at 590 °C, 0.10 mbar O_2 at a deposition rate of 50 Hz on BHF-etched (001) $NdGaO_3$. (a) Topographic AFM (0.7×0.7 μm^2) and the step height. (b) RHEED pattern of the film (recorded on [001] direction).*

superconductivity was observed in the $ACuO_2$ films before or after annealing. According to XRD measurements, the annealed samples showed a small decrease of the c-axis parameter, an indication of incorporation of extra oxygen in the structure. No other structural modifications were observed for the annealed samples.

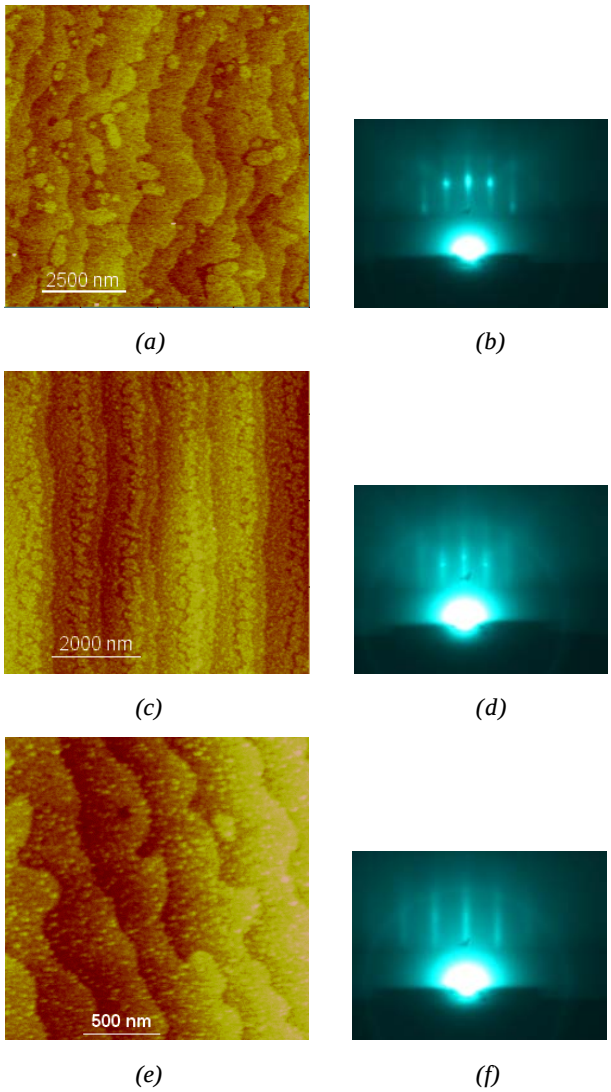

Fig. 5.6 *Surface morphology and corresponding RHEED patterns of (a) and (b) 50 unit cells $CaCuO_2$ grown by PLiD at 610 °C, 0.10 mbar O_2 and deposition rate of 50 Hz on BHF-etched (001) $NdGaO_3$ (2 nm $SrCuO_2$ as buffer layer). (c) and (d) 100 unit cells $SrCuO_2$ grown by PLiD at 550 °C, 0.10 mbar O_2 and deposition rate of 50 Hz on annealed (001) $NdGaO_3$. (e) and (f) 22 unit cells $BaCuO_x$ grown by PLiD at 610 °C, 0.10 mbar O_2 and deposition rate of 50 Hz on BHF-etched (001) $NdGaO_3$ (3.5 nm $SrCuO_2$ as buffer layer).*

5.3.2 (Ba,Sr,Ca)CuO_2 superlattices

5.3.2.1 Deposition

The growth of artificially layered superlattices is complicated by the fact that for each successive layer the underlayer changes every time, with implications for the sticking coefficient and growth. When the deposited material exhibits a true layer-by-layer growth every RHEED oscillation period corresponds to the deposition of one stable unit block (typically one unit cell). The required deposition conditions to achieve superconductivity in these structures by insertion of excess oxygen in the CR blocks (e.g., high deposition pressure associated with relatively low deposition temperatures) leads to a 3D growth. This hampers significantly monitoring and controlling the growth.[4,7,11] In the previous section it was shown that by means of PLiD a 2D growth mode can be imposed for all $ACuO_2$ compounds at certain deposition parameters, while high-pressure RHEED is a very efficient tool for monitoring the growth in situ at deposition pressures required for these artificial structures. Of course, the deposition parameters have to be selected according to the stability conditions (temperature, pressure, the choice of the substrate) of the deposited phases. Therefore, it is expected that the interval deposition give a tool for growth of the $ACuO_2$-based superlattices in a 2D fashion.

The number of pulses required to complete one unit-cell layer from each of the superlattice components was determined from growth experiments of individual $ACuO_2$ layers by counting the number of pulses corresponding to one oscillation period of the RHEED intensity. The $[(Ba,Sr)CuO_2]_m/[(Ca,Sr)CuO_2]_n$ films were then grown by sequential deposition of the constituent blocks. Further tuning of the deposition rate for the CR and IL blocks was made in situ during growth of the superlattices by continuum monitoring of the specular intensity and ex situ from XRD spectra of the resulted films.

5.3.2.2 Structural and morphological properties

Typical RHEED patterns for infinite layer superlattices with different deposition sequences are shown in Fig. 5.8 BCO shows always a decrease of the RHEED intensity; the intensity fully or partial recovers after subsequent deposition of the SCO or CCO block (see Fig. 5.8a and b). The specular reflection has a sharper profile, indication of a smoother surface, for BCO/SCO and SCO/CCO superlattices. For the BCO/SCO and SCO/CCO films the RHEED patters shows only a small decrease of the specular reflection intensity during deposition (Fig. 5.8b and c), in contrast with a larger decrease of the intensity for the BCO/CCO structures (Fig. 5.8a). The difference in behaviour can be explained by the larger in-plane lattice mismatch between the constituent infinite layer blocks and, possible, by slight errors in the growth rates of constituent layers of superlattices. The BCO/CCO superlattices are characterized by a higher level of internal stress due to larger difference between the constituent alkaline earth atoms, resulting in a higher strain on the superconductive (CCO) block from the part of charge reservoir (BCO) block.

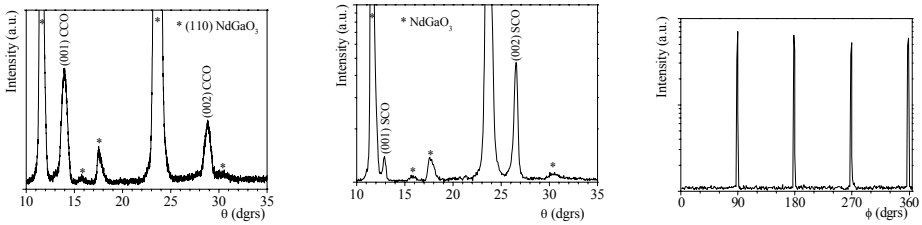

(a) *(b)* *(c)*

Fig. 5.7 *XRD θ-2θ scans of (a) 16 nm thick $CaCuO_2$ film and (b) 35 nm thick $SrCuO_2$ layer. (c) ϕ scan around {202} reflection of the $SrCuO_2$ film.*

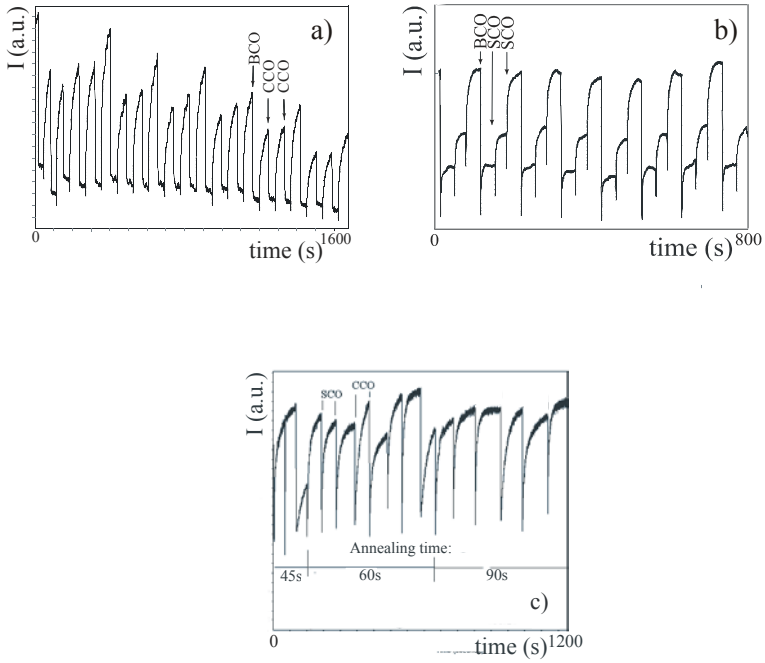

Fig. 5.8 *Evolution of the specular reflection intensity during deposition of (a) $[(BaCuO_x)_2/(CaCuO_2)_2]_{32}$, (b) $[(BaCuO_x)_2/(SrCuO_2)_2]_{40}$, (c) $[(SrCuO_2)_2/(CaCuO_2)_2]_{20}$.*

For BCO/SCO and SCO/CCO films ex-situ AFM micrographs (Fig. 5.9a, b and f) show that a true layer-by-layer growth could be obtained. As can be observed from Fig. 5.9a and b, the imprint of the substrate can still be seen even for thick films (40 layers of 2BCO/2SCO). The island-like morphology of the substrate is preserved after the deposition of the film, an indication that the RHEED oscillations from Fig. 5.8b are not due to a step flow growth mode, but due to true layer-by-layer. The

corresponding RHEED pattern shows streaks (Fig. 5.9c for the BCO/SCO superlattice) or 2D diffraction dots on a streaky background (Fig. 5.9g for the SCO/CCO superlattice), indication of a smooth surface. A slightly rougher surface morphology is characteristic for the BCO/CCO films (Fig. 5.9d), as expected from the recorded RHEED pattern (Fig. 5.9e), but anyway still reasonably smooth.

For all superlattices, the θ-2θ XRD scans shows the presence of satellite peaks originating from the artificial superstructures. The superlattice period Λ and the average lattice parameter were calculated from the position of these peaks and then used to further calibrate the deposition rate of each IL block. The period Λ was calculated by using the relation (5.1):

$$\Lambda = \lambda/2(\sin\theta_{(\pm1)} - \sin\theta_0) \qquad (5.1)$$

where λ is the x-ray wavelength, $\theta_{(\pm1)}$ and θ_0 are respectively the diffraction angles of the first order satellite peak and the 0^{th} order peak.[7,11] The average lattice parameter $\bar{c} = (m\cdot c_1+n\cdot c_2)/(m+n)$ was estimated from the angular position of the 0^{th} order peaks. When ratio $\Lambda/\bar{c}$ is an integer number, the superlattices consists of an integer number of individual layers. When this ratio is not an integer number, incommensurability between the chemical period and the crystallographic structure takes place[18]

The result of XRD scans for some of the $ACuO_2$ superlattices are given in Fig. 5.10. When the exact number of laser shots that correspond to each constituent layer deviates from an integer number of layers, due to small errors in the estimate of the deposition rate or intermixing, the satellite peaks shows broadening, splitting and lower intensity than the expected one from calculations for an ideal structure. These effects can be seen from the XRD scans given in Fig. 5.10b-d, with superstructure reflections of the films having weaker than expected intensities indicating the presence of Ba/Sr disorder that can be expected from inaccuracy in the deposition rate(s). In Fig. 5.10a is shown the XRD pattern for a $[(BaCuO_2)_2/SrCuO_2]_{25}$ superlattice (the $SrCuO_2$ reflection is due to the 4 nm buffer layer) with the determined deposition rates closed to the correct values. All films were single-phase c-oriented, with satellite reflection resulted from superlattice periodicity.

To determine if an odd number of BCO layers can be stabilized between SCO or CCO layers, BCO_m/SCO_n superlattices with m = 1 or 3 were grown and then analysed with X-ray diffraction. The resulted XRD patterns showed that these types of structures could be grown when $NdGaO_3$ was used as template and PLiD as deposition technique. In Fig. 5.11 the evolution of the intensity of the specular spot for a 3BCO/2SCO structure is shown. The BCO could be deposited as three different layers of one unit cell each or as one deposition block consisting of three BCO unit cells deposited once.

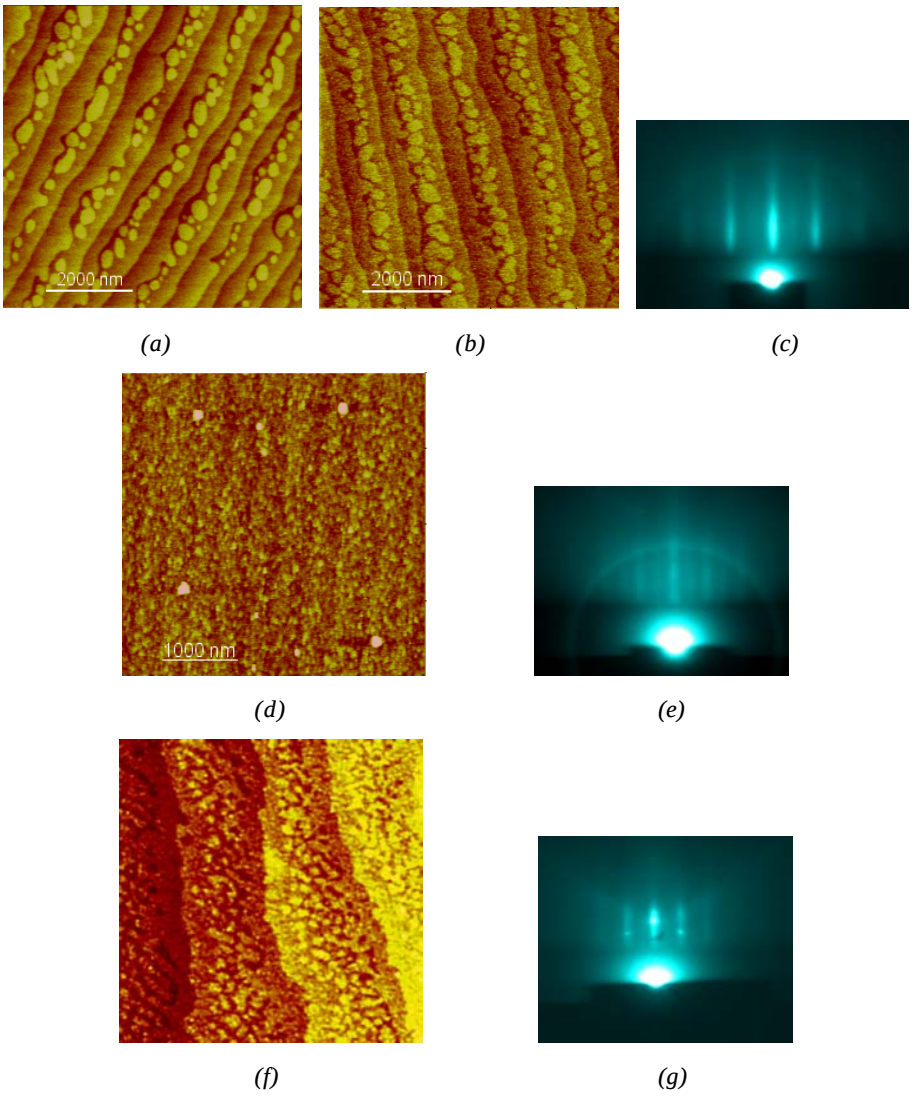

Fig. 5.9 *AFM micrographs and corresponding RHEED patterns of* $(2BCO/2SCO)_{40}$ *grown at 550 °C, 0.10 mbar* O_2 *(b and c).* $(2BCO/2CCO)_{32}$ *grown at 550 °C, 0.10 mbar* O_2 *(d and e).* $(2SCO/2CCO)_{20}$ *grown at 575 °C, 0.16 mbar* O_2 *(f and g). All films were grown on annealed (001)* $NdGaO_3$ *with a laser repetition rate of 50 Hz. The surface morphology of the substrate used for deposition of film (b) is depicted in (a).*

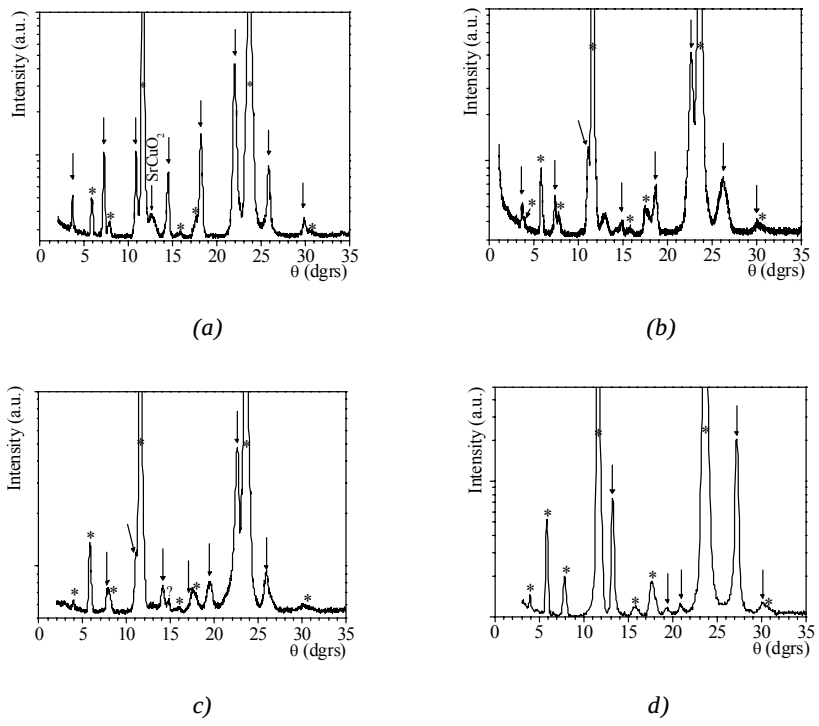

Fig. 5.10 *XRD θ-2θ scans for (a) $[(BaCuO_2)_2/SrCuO_2]_{25}$, (b) $[(BaCuO_2)_{2-x}/(SrCuO_2)_{1+x}]_{25}$, (c) $[(BaCuO_2)_{2-x}/(CaCuO_2)_{2+x}]_{32}$, and (d) $(SrCuO_2)_2/(CaCuO_2)_2]_{20}$. The arrows indicate the (00l) reflections of the films, while the peaks corresponding to the substrate are indicated with an asterix.*

5.3.2.3 Electrical properties

The electrical properties of the infinite layer superlattices were measured with the four-probe technique, inside a He cryostat. Al wires were used for better contact with the film. The electrical properties of the superlattice films depended on the cooling conditions. When the BCO/SCO films were cooled down under deposition pressure, the RT measurements shown high-resistance semiconductor behaviour that increases exponentially with decreasing temperature. The films annealed in situ or cooled down in a high pressure ambient (> 750 mbar) shown a significantly lower resistance, with semiconducting behaviour. Similar electrical properties showed the films cooled down under deposition pressure and subsequently annealed ex-situ, in a tube oven, at temperatures of 450-550 ^oC under oxygen flow (~ 400 l/h). No full superconducting transition was observed in BCO/SCO, BCO/CCO, or SCO/CCO superlattices. A higher resistance for all the temperature range used for measurement was always observed for SCO/CCO films, comparing with BCO/SCO or BCO/CCO ones. A possible explanation for this behaviour can be the lower oxygen content in the SCO/CCO superlattices than in the other $ACuO_2$-superlatices due to lower oxygen content in the CR blocks.

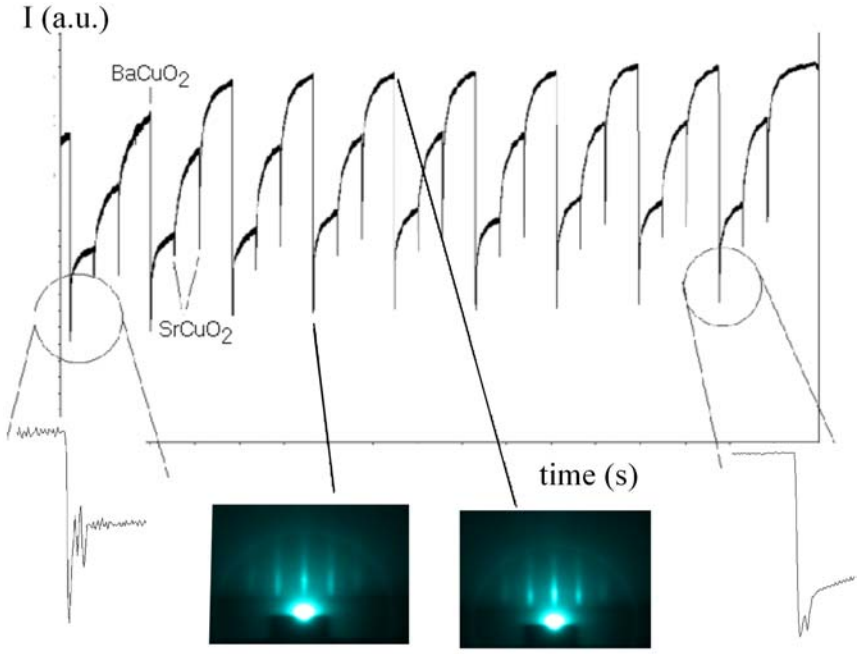

Fig. 5.11 *Evolution of the specular reflection intensity (recorded between the 12th and 21st blocks) during deposition of $(BaCuO_2)_3/(SrCuO_2)_2$ superlattices. RHEED patterns after deposition of the $BaCuO_2$ and $SrCuO_2$ blocks are also shown.*

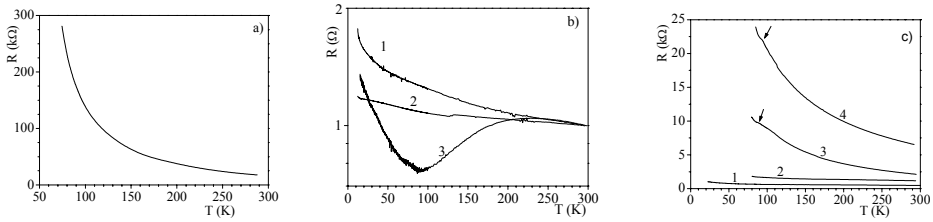

Fig. 5.12 *(a) Resistance versus temperature of a $SrCuO_2$ film (P_d = 5×10-2 mbar O_2, T_s = 550 °C). (b) Normalized resistance versus temperature of (1) $(BaCuO_2)_2/SrCuO_2$ (P_d=5×10-2 mbar O_2, T_s = 550 °C), (2) $(BaCuO_2)_{2-x}/SrCuO_{2+x}$, (3) $(BaCuO_2)_2/SrCuO_2$ (P_d = 0.30 mbar O_2, T_s = 550 °C). (c) Resistance versus temperature of (1) $(BaCuO_2)_2/(SrCuO_2)_2$, (2) $(BaCuO_2)_2/(Sr_{0.75}Ca_{0.25}CuO_2)_2$, (3) $(BaCuO_2)_2/(CaCuO_2)_2$, and (4) $(SrCuO_2)_2/(CaCuO_2)_2$.*

The possibility to control the oxygen content by tuning the structural disorder and, therefore, the electrical properties of the films, was used by growing films with different deposition rates for BCO block and modifying the corresponding deposition rates of the IL block to compensate. For example, structures of $[(BaCuO_2)_{2-x}/(SrCuO_2)_{1+x}]_m$ composition were deposited in these manner. The resistance of these films scales with

the concentration of structural disorder, but the general semiconductor character of the films remained (see Fig. 5.12b2 for RT data of a $(BaCuO_2)_{2-x}/(SrCuO_2)_{1+x}$ film deposited at 550 °C and 5×10^{-2} mbar O_2). Some of the films deposited at pressures of 0.30 mbar O_2 showed variations in the resistance curve with temperature, but without reaching zero resistance (see Fig. 5.12b3 for RT data of a $(BaCuO_2)_{2-x}/(SrCuO_2)_{1+x}$ film deposited at 550 °C and 0.30 mbar O_2). The lack of superconductivity is probably due to charge compensation, charge transfer of mobile charges across the layers and to the presence of crystalline defects at the interface between the constituent CR and IL blocks. The occurrence of interfacial defects, mainly oxygen losses and crystalline defects, at the substrate/film interface can also affect the functionality of the CR blocks.[12]

Fig. 5.12c shows resistance-temperature curves for films with a $[(Ba,Sr)CuO_2]_2/[(Ca,Sr)CuO_2]_2$ structure. Semiconducting behaviour with the resistance increasing with decreasing temperature can be observed. The resistance increases for films with $SrCuO_2$ as the CR block and/or $CaCuO_2$ as IL block. Small but distinct variations in the resistance-temperature curve could be seen for all superlattices. The temperature at which this variations of resistance appear is about 100 K, 90 K and 80 K for SCO/CCO, BCO/CCO and BCO/SCO, respectively. All the films showing this variation in the resistance curve were deposited at pressures higher than 0.20 mbar O_2 and their XRD patterns were characterized by structural and, possible, chemical modulations. These observations suggest possible onset of superconductivity in small regions in these films, embedded in the matrix of the majority semiconducting material.

5.4 Conclusions

In this chapter it was demonstrated that pulsed laser deposition could be used to grow single-phase thin films of $ACuO_2$ phases and artificially layered structures of these copper oxides. By using (001) or (110) $NdGaO_3$ as atomic template these metastable phases could be stabilized in their tetragonal symmetry. It was shown that by growth monitoring and manipulation all $ACuO_2$ phases can be grown, with different critical thickness, on bare $NdGaO_3$ substrates without using a buffer layer. According to AFM micrographs, the use of single-terminated $NdGaO_3$ substrates played a critical role in yielding films with smooth surface morphology. The XRD data showed that the films are epitaxial, with complete in-plane crystalline alignment with the substrate. The artificially layered superlattices showed a dependence of their structural and electrical properties on the growth conditions (deposition pressure and temperature, as well as on the deposition rate for each infinite layer constituent block).

There are two critical factors that determined the final properties of the studied superlatices: the correct determination of the deposition rate, which can be accurately determined by means of in situ high-pressure RHEED, and the quality of the interface between the constituent blocks, which can be controlled by growth manipulation, in this case by means of interval deposition. These aspects determined the final structure, defects network, and morphology of the films. The structure, determined also by the deposition pressure, leads to the final transport properties. A high oxygen pressure (> 0.30 mbar O_2) is required for these superlattices to show superconductivity. The use of $NdGaO_3$ helps stabilizing the right tetragonal $ACuO_2$ phases and their superlattices

by the induced compressive strain, but the desired superconducting properties require deposition conditions that can assure incorporation of enough excess oxygen to reach the charge carries density needed to dope the CuO_2 planes from the IL blocks. The results presented in this chapter showed that there is a potential for $NdGaO_3$ as template for $ACuO_2$ films and heterostructures and, probably, under optimum deposition conditions (e.g., deposition pressure, growth monitoring and manipulation) superconductivity can be observed in these structures.

References

1 H. Ihara, K. Tokiwa, H. Ozawa, M. Hirabayashi, A. Negishi, H. Matuhata and Y.S. Song, *Jpn. J. Appl. Phys.* **33**, L503 (1994)

2 J.N. Eckstein, I. Bozovic, K.E. von Dessonneck, D.G. Schlom, J.S. Harris Jr. and S.M. Baumann, *Appl. Phys. Lett.* **57**, 931 (1990)

3 D.P. Norton, B.C. Chakoumakos, J.D. Budai and D.H. Lowndes, *Appl. Phys. Lett.* **62**, 1679 (1993)

4 D.P. Norton, B.C. Chakoumakos, J.D. Budai, D.H. Lowndes, B.C. Sales, J.R. Thompson and D. K. Kristen, *Science* **265**, 2074 (1994)

5 X. Li, T. Kawai and S. Kawai, *Jpn. J. Appl. Phys.* **33**, L18 (1994)

6 D.P. Norton, J.D. Budai, D.H. Lowndes and B.C. Chakoumakos, *Appl. Phys. Lett.* **65**, 2869 (1994)

7 C. Aruta, G. Balestrino, R. Desfeux, S. Martellucci, A. Paoletti and G. Petrocelli, *Appl. Phys. Lett.* **68**, 926 (1996)

8 D.P. Norton, D.H. Lowndes, J.D. Budai, B.C. Chakoumakos, *Mater. Sci. Eng.* **B41**, 374 (1996)

9 G. Balestrino, S. Martellucci, P.G. Medaglia, A. Paoletti, G. Petrocelli and A.A. Varlamov, *Phys. Rev. B* **58**, R8925 (1998)

10 I.K. Schuller, M. Grimsditch, F. Chambers, G. Devane, H. Vanderstraeten, D. Neerinck, J.P. Locquet and Y. Bruynseraede, *Phys. Rev. Lett.* **65**, 1235 (1990)

11 G. Koster, *Artificially layered oxides by pulsed laser deposition*, PhD thesis ISBN 9036513367, University of Twente, The Netherlands (1999)

12 S. Lavanga, G. Balestrino, P. G. Medaglia, P. Orgiani and A. Tebano, *Physica C* **372 – 376**, 590 (2002)

13 V. Braccini, D. Marre, A. Malagoli, A. Mollica, M. Putti, G. Balestrino, S. Lavanga, P. B. Medaglia and A. S. Siri, *Physica C* **372-376**, 616 (2002)

14 G. Balestrino, S. Lavanga, P.G. Medaglia, P. Orgiani, A. Paoletti, G. Pasquini, A. Tebano and A. Tucciarone, *Appl. Phys. Lett.* **79**, 99 (2001)

15 F. Arciprete, G. Balestrino, S. Martellucci, P.G. Medaglia, A. Paoletti and G. Petrocelli, *Appl. Phys. Lett.* **71**, 959 (1997)

16 G. Balestrino, C. Ferdeghini, S. Gariglio, D. Marre, P.G. Medaglia, G. Petrocelli and A.S. Siri, *Solid State Commun.* **108**, 499 (1998)

17 G. Balestrino, S. Martellucci, P.G. Medaglia, A. Paoletti and G. Petrocelli, *Physica C* **302**, 78 (1998)

18 G. Balestrino, S. Lavanga, P.G. Medaglia, S. Martellucci, A. Paoletti, G. Pasquini, G. Petrocelli, A. Tebano, A.A. Varlamov, L. Maritato and M. Salvato, *Phys. Rev. B* **62**, 9835 (2000)

19 A. Tebano, G. Balestrino, S. Lavanga, S. martelluci, P.G. Medaglia, A. Paoletti, G. Pasquini, G. Petrocelli and A. Tucciarone, *Physica C* **355**, 335 (2001)

20 G. Balestrino, G. Pasquini and A. Tebano, *Phys. Rev. B* **62**, 1421 (2000)

21 S. Lavanga, G. Balestrino, P.G. Medaglia, P. Orgiani and A. Tebano, *Physica C* **372 – 376**, 590 (2002)

22 E.E. Fullerton, I.K. Schuller, H. Vanderstraeten and Y. Bruynseraede, *Phys. Rev. B* **45**, 9292 (1992)

23 E.E. Fullerton, J. Guimpel, O. Nakamura and I.K. Schuller, *Phys. Rev. Lett.* **69**, 2859 (1992)
24 A.J.H.M. Rijnders, *The initial growth of complex oxides: study and manipulation*, PhD thesis ISBN 9036516579, University of Twente, The Netherlands (2001)
25 M. Kawai, Z.-Y. Liu, T. Hanada, M. Katayama, A. Aono and C.F. McConville, *Appl. Surf. Sci.* **82/83**, 487 (1994)
26 A. Gupta, B.W. Hussey, T.M. Shaw, A.M. Guloy, M.Y. Chern, R.F. Saraf and B.A. Scott, *J. Solid State Chem.* **112**, 113 (1994)

Chapter 6

$Sr_{1-x}La_xCuO_2$, an n-type infinite layer compound

6.1 Introduction

To this date, there are two known systems of electron doped superconducting cuprates (HTSc): the *T'–phase* compounds, $Ln_{2-x}Ce_xCuO_4$ (Ln = La, Pr, Nd, Sm, or Eu),[1-3] with a maximum T_c of ~ 30 K, and the *infinite-layer* (IL) compounds, $Sr_{1-x}Ln_xCuO_2$ (Ln = La, Pr, Nd, Sm, or Gd), with a maximum T_c ~ 43 K.[4-6] The studies of fundamental physical properties and applications of n-type HTSc are hampered by the difficulty in yielding single-phase samples. Epitaxial stabilization of these metastable phases is successfully used as an alternative synthesis method. However, the superconducting properties of $Sr_{1-x}Ln_xCuO_2$ thin films are still far from that obtained for bulk samples. For example, the highest T_c of 39 K for an n-type IL film, i.e., $Sr_{1-x}La_xCuO_2$ grown by MBE on $KTaO_3$,[5] was obtained after more than 10 years from first bulk synthesis of this compound. As discussed in Chapter 2, the physical properties of the $Sr_{1-x}Ln_xCuO_2$ IL compounds are affected by the preparation conditions. The inhomogeneous distribution of doping element, the oxygen network (mainly the presence of the apex oxygen) as well as the inter-granular links can lead to suppression of superconductivity in the high-pressure high-temperature samples.[6,7]

Thin film growth enabled the preparation of these metastable phases by considering the epitaxial strain effect of the substrate.[4,8-10] Pulsed laser deposition (PLD) is one of the techniques suitable for the preparation of tetragonal $Sr_{1-x}Ln_xCuO_2$ phases.[10-13] In this chapter, the properties of PLD grown $Sr_{1-x}La_xCuO_{(2+x/2)\pm\delta}$[i] (SLCO) thin films will be presented and discussed for $0.1 \le x \le 0.2$. The influence of the morphology and chemistry of the substrate surface, deposition parameters (deposition

[i] δ corresponds to the excess (removed) oxygen resulting from oxidation (reduction) of Cu above (below) formal valence 2+.

technique, i.e., PLD or PLiD[ii], deposition pressure and temperature, and type of gas used during growth), and cooling procedure is studied with respect to morphological, structural, and physical properties of the films. The type of doping in these compounds requires that the CuO_2 plane to be under tensile strain. Therefore, two types of substrates (i.e., $SrTiO_3$ and $KTaO_3$) were used that gave the possibility of controlling the type of strain (compressive or tensile) in the films by tuning the cell parameters. The experimental conditions required for yielding single crystal like SLCO phases will be presented in the last part of the chapter.

6.2 Experimental results

6.2.1 Growth conditions

The SLCO films, with a thickness in range of 50-250 nm, were grown by means of standard PLD or PLiD techniques. The computer controlled PLD system, equipped with in situ high-pressure RHEED, used for these experiments was described in Chapter 3. The growth and film thickness were controlled in situ by monitoring the RHEED intensity oscillations of the specular spot. The RHEED gun was operated at 20 KeV with the electron beam focused to the surface at a glazing incidence angle of 1-1.5° along [100] or [110] directions of the substrates. $SrTiO_3$ and $KTaO_3$ single crystal substrates, both (001) oriented, with miscut angle in range of 0.05-0.2° were used. Prior to the deposition each wafer was cleaned in organic solvents (chloroform, acetone, and ethanol) and, when needed, subsequently chemically and/or thermally treated following the procedures described in Chapter 4. The substrates were thermally attached to the heater block (substrate holder) using Ag paste.

Prior to the film deposition, in order to eliminate the possible surface contamination during sample handling, the substrates were annealed in situ at a base pressure of $0.5\text{-}1\times10^{-6}$ mbar for 0.5 h at 700 °C, for $SrTiO_3$, and 0.5 h at 550 °C and then 15-20 min at 700 °C, for $KTaO_3$ substrates, respectively. As discussed in Chapter 4, a 3D

Table 6.1 *Deposition parameters for $Sr_{1-x}La_xCuO_2$ grown on (001) $SrTiO_3$.*

Target composition	$Sr_{1-x}La_xCuO_2$ ($0.10 \le x \le 0.20$)
Substrate	(100) $SrTiO_3$
	$5\times5\times1$ mm^3
Substrate temperature	500-600°C
Deposition pressure	$10^{-3}\text{-}4\times10^{-1}$ mbar
Laser repetition rate	1-50 Hz
Deposition gas	O_2, O_2/N_2, or N_2
Distance target-substrate	40-50 mm
Energy density at target	1.30-2.50 J/cm^2
Laser energy behind mask	30-40 mJ

[ii] Pulsed Laser interval Deposition.

Table 6.2 *Deposition parameters for $Sr_{1-x}La_xCuO_2$ grown on (001) $KTaO_3$.*

Targets composition	$Sr_{1-x}La_xCuO_2$ ($0.10 \le x \le 0.20$)
	$Sr_{(1-x)+\delta}La_xCuO_2$ ($0.10 \le x \le 0.15$; $\delta = 0.10$) or
	$Sr_{1-x}La_xCu_{1+\delta}O_2$ ($x = 0.15$, $\delta = 0.10$)
Substrate	(100) $KTaO_3$
	$5\times5\times0.5$ mm^3
Laser repetition rate	1-5 Hz
Substrate temperature	500-550 °C
Deposition pressure	5×10^{-4}-10^{-2} mbar
Deposition gas	O_2 or O_2/O_3
Distance target-substrate	40-50 mm
Energy density at target	1.75-2.50 J/cm^2
Laser energy behind mask	30-45 mJ

pattern corresponding to a phase with in-plane cell parameters of about 4.2 Å could sometimes be observed in RHEED patterns of the as-received $KTaO_3$ substrates after the 700 °C annealing step. Therefore, annealing at this temperature was avoided for the as-received $KTaO_3$ substrates. For some runs, a $BaTiO_3$ buffer layer with thickness of 2-20 nm was deposited at temperatures of 700-800 °C and background pressure of 0.1 mbar O_2. When deposited on $SrTiO_3$, the $BaTiO_3$ layer was used with the aim of inducing tensile strain in the SLCO films. When deposited on $KTaO_3$, $BaTiO_3$ layer helped to improve the morphology of the as-received or treated (chemically and/or thermally) substrates and, after a certain critical thickness[iii], to further increase the tensile strain induced in the SLCO films by the film-substrate lattice mismatch[iv]. $BaTiO_3$ provides also a chemically and structurally compatible template for subsequent growth of the IL.[15,16] A post-deposition annealing step (~ 0.25-0.5 h) at 750-900 °C and 0.1 mbar O_2 was applied for all $BaTiO_3$ layers prior deposition of the SLCO films. Some of the $BaTiO_3$ films deposited on $SrTiO_3$ were annealed in vacuum (0.5-1 h at $0.5\text{-}1\times10^{-6}$ mbar) at 900 °C in order to obtain a defect free, relaxed buffer layer[v].[14,17] For ablation of the $BaTiO_3$ target, an energy density of 1.75 J/cm^2 and a spot size of 1.60 mm^2 were used.

The main deposition parameters for SLCO grown on $SrTiO_3$ and $KTaO_3$ are given in Tables 6.1 and 6.2, respectively. A continuous flux of molecular oxygen or a mixture

[iii] The first few monolayers of the buffer layer are coherent with the substrate and, therefore, fully strained. The cell parameters of the buffer layer depend on its thickness and deposition parameters, such as background gas pressure and growth rate.[14]

[iv] The in-plane cell parameters are 3.989 Å and ~ 4.02 Å for bulk $KTaO_3$ and $BaTiO_3$, respectively.

[v] Terai *et al.*[14] have shown that a fully relaxed tetragonal $BaTiO_3$ film (grown on $SrTiO_3$) could be obtained by annealing it at 1100 °C under 10^{-6} mbar of oxygen (the time scale was not specified). After annealing the strain was completely accommodated by the first unit cell layers of the $BaTiO_3$ film, all dislocations been localized at the $BaTiO_3/SrTiO_3$ interface.

of O_2/O_3 (max. 10% O_3) was used as oxidant. The molecular oxygen and the O_2/O_3 mixture are supplied through different inlets. A mixture of O_2/N_2 (21 vol.% O_2/ 79 vol.% N_2, if otherwise specified) was also used[vi] as deposition gas for some of the runs on $SrTiO_3$. The value for the lowest deposition pressure was chosen so that the oxygen activity requirements for kinetic and thermodynamic stability of the IL phase are satisfied. The O_2/O_3[vii] mixture was used to increase the oxidation power and, therefore, to increase the thermodynamic stability of the infinite layer phase when deposited at low pressures. The distance between the end of the O_3 inlet and substrate is about 4 cm and the O_3 flow is directed parallel to the substrate surface. The majority of the films have been grown at a substrate temperature of 550 °C. After growth, the films were cooled down to 400 °C inside the deposition chamber and then placed in the loadlock for faster cooling down to room temperature. Some films were placed in loadlock immediately after deposition, without preliminary cooling in the deposition chamber. After the films were placed in loadlock, different cooling procedures have been used:

1. the pressure was kept at the same value as the background pressure used during deposition,
2. the pressure was slowly increased (in ~ 0.5 h) to 20-10^3 mbar[viii], or
3. the loadlock was flooded with N_2 or O_2 (immediately after the film was placed in loadlock) up to pressures of 20-10^3 mbar.

In situ post-deposition annealing for 0.25-1 h at 450-550 °C and pressures of 10-35 mbar or in vacuum (5×10^{-6} mbar) was also applied to some of the SLCO films.

Commercial high-density sintered targets[ix] (HITEC Materials, Germany, target density higher than 95%) were used for deposition of the x = 0.1 and 0.15 SLCO films. For the other compositions, the targets[x] were prepared by sintering in air the required stoichiometric mixtures of high-purity $SrCO_3$, La_2O_3, and CuO powders. The mixtures were pressed uniaxialy in pellets of about 15mm in diameter and 5 mm thickness and then fired at 950 °C for 48 h in air with three intermediate grindings for better homogeneity. Before the final thermal treatment at 950 °C for 12 h in air, the powders were uniaxialy pressed at pressures of 100 MPa to obtain a high-density target. Anyway, the density of these "home-made" targets was lower than that of the commercial ones.

As described in Chapter 3, X-ray diffraction (Cu Kα radiation) in the normal Bragg-reflection geometry and HRTEM were used for structural characterization of the SLCO films. The lattice parameters of the films were calculated from XRD data employing 18-25 reflections by a least square fitting technique for an ideal tetragonal unit cell.

[vi] The selection of the O_2/N_2 mixture was motivated by the synthesis conditions of the bulk n-type IL (see Chapter 2) which is done under high-pressure and high-temperature conditions in air, with subsequent reduction in nitrogen during cooling in order to induce superconductivity.

[vii] O_3 was produced by pulse injection corona discharge in a generator (Azcozon HTU 500GE, Azco Industries Ltd.)[18] placed outside the deposition chamber.

[viii] The pressure increases continuously during cooling until it reaches the desired pressure (with a maximum of 1 bar) and then the gas flow is stopped.

[ix] Pellets of ~ 30 mm in diameter and ~ 10 mm thickness.

[x] Pellets of ~ 20 mm in diameter and ~ 5 mm thickness.

Standard four probe dc transport measurements have been used for electrical characterization of the films. The results of structural and electrical properties for SLCO films grown on $SrTiO_3$ and $KTaO_3$, respectively, will be presented separately in next sections.

6.2.2 $Sr_{1-x}La_xCuO_2$ on $SrTiO_3$

6.2.2.1 Initial growth and surface morphology

As discussed in Chapters 2 and 3, the basic growth mode of an epitaxial thin film on a given substrate depends on the balance between various thermodynamic and kinetic factors related to the phase formation and the surface properties at the growth front. Certain growth modes of cuprates can be induced by properly selecting the parameters controlling the growth: oxygen partial pressure, oxygen potency, substrate temperature, miscut angle, surface chemistry and morphology, substrate-film lattice mismatch, and growth rate.[19] The surface mobility of the ad atoms during deposition also plays an important role in determining the growth mode. The difference in mobility of the ad atoms can be seen from, e.g., the RHEED oscillation intensity recoveries during and after interrupting the growth.

The growth of atomically smooth epitaxial films requires the control of the substrate-film interface properties. Furthermore, growth kinetics at this stage of growth can have a large influence on the final film properties. Understanding of the basic processes taking place at this stage of the growth enables adjusting of the deposition parameters in order to eliminate or control the presence of structural defects. Studies of the initial growth mechanism and the formation and evolution of surface defects at the growth front can provide useful information relevant to the final film microstructure.

The initial nucleation and growth stages of the heteroepitaxial SLCO thin films grown on $SrTiO_3$, as investigated in situ by high pressure RHEED and ex situ by AFM, will be discussed next. The RHEED pattern and the intensity of the specular spot were constantly monitored during growth in order to determine the film thickness in situ, as well as to control the evolution of the films surface structure and morphology at the growth front. It will be shown that n-type IL films with desired structural and physical properties can be obtained using techniques such as PLD (or PLiD) and in situ high-pressure RHEED.

Standard PLD technique (laser repetition rate of 1-5 Hz) was initially used for deposition of the $Sr_{1-x}La_xCuO_{2\pm\delta}$ (x = 0.1-0.2) films on $SrTiO_3$. The in-plane cell parameter of SLCO varies[xi] with La doping level, x. From this a dependence of the evolution of the growth front with x is expected, caused by different level of strain. Indeed, RHEED data showed that, although all films undergo a transition from a layer-by-layer like (2D) to island (3D) growth mode at the initial stage of the growth, this conversion take place faster for an increased level of doping. For example, in Fig. 6.1 the RHEED patterns and time evolution scans of the specular beam intensity for heteroepitaxial growth of two SLCO films (x = 0.1 and 0.15) on SrO terminated $SrTiO_3$

[xi] i.e., a increases for $0.1 \leq x < 0.15$ and then decreases with x.[20]

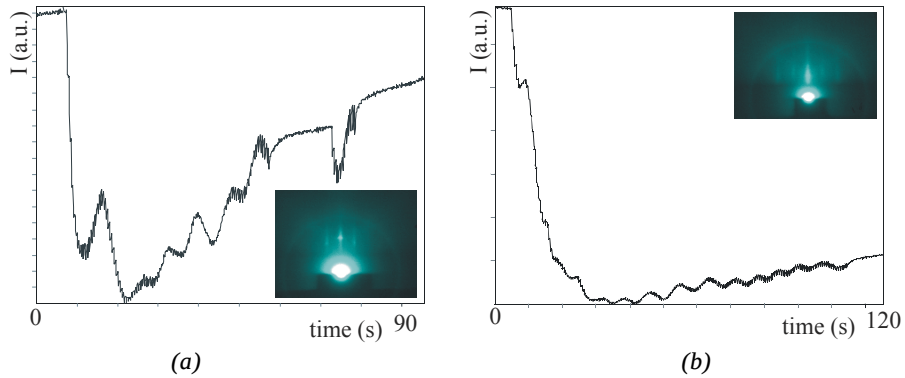

Fig. 6.1 *RHEED patterns and specular beam intensity oscillations during heteroepitaxial growth of $Sr_{0.90}La_{0.10}CuO_2$ (a) and $Sr_{0.85}La_{0.15}CuO_2$ (b) on (001) $SrTiO_3$ taken along the (100) substrate azimuth. Both films were grown at a substrate temperature of 550 °C, deposition pressure of 0.10 mbar O_2 and a pulse rate of 3 Hz.*

substrates at 550 °C and 0.1 mbar O_2 (or O_2/N_2) are given[xii]. The scans show a strong decrease of intensity of the specular spot after the first unit cell with subsequent recovery at levels determined by the surface mobility. From the beginning of deposition, the sharp 2 D spots, originating from the $SrTiO_3$ substrate, are blurred into streaks originating from the unit cell of SLCO. This decrease[xiii] of the RHEED intensity can be correlated with the film-substrate interface properties. The formation of streaks in the RHEED pattern is an indication of somewhat roughened surface, i.e., the step density at the surface is increased.

At this stage of deposition, the growth mode of the films depends upon the relative strengths of adatom-substrate and adatom-adatom bonding, and on lattice matching. If the adatom-substrate bond is strong, then layer-by-layer growth may take place initially. Otherwise, the film grows in the island mode.[21,22] As showed in Chapters 2 and

[xii] When SCLO films are deposited on TiO_2 terminated $SrTiO_3$ substrates, RHEED patterns showed clear 3D spots besides the streaks corresponding to the IL phase. Stronger 3D patterns form when O_2/N_2 mixture is used as deposition gas. From the horizontal and vertical distances between the spots a lattice parameter of ~ 4.3 Å was determined. By considering the applied constituents (i.e., Sr, La, Cu, and O), Cu_2O was identified to be responsible for these 3D patterns. Therefore, to avoid the formation of Cu_2O precipitates, one monolayer SrO was deposited on $SrTiO_3$ prior growing the SLCO films. SrO terminated $SrTiO_3$ obtained by ex-situ oxygen annealing (see Chapter 4) were also used.

Deposition parameters for SrO on $SrTiO_3$: T_s = 800 °C, P_d = 0.1 mbar O_2, a deposition rate of ~ 0.05 nm per laser pulse; the laser was operated at a pulse rate of 50 Hz.

[xiii] Before deposition, at the glazing incident angle used for measurements, the specular RHEED intensity is selected to be maximal for $SrTiO_3$. After deposition, because of the difference in the lattice parameters of the substrate and film, the conditions for diffraction are modified. Therefore, a small increase of the specular RHEED intensity is observed after a small change of the angle of incidence of the electron beam.[22]

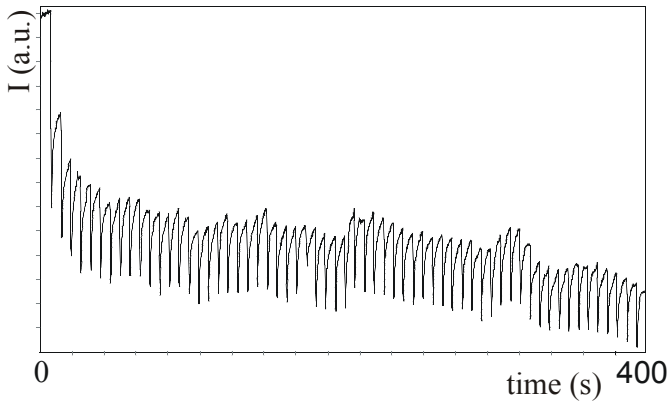

Fig. 6.2 *Intensity of the RHEED specular beam during heteroepitaxial growth of $Sr_{0.90}La_{0.10}CuO_2$ on SrO terminated $SrTiO_3$. The film was deposited at a substrate temperature of 550 °C, deposition pressure of 0.10 mbar O_2 (or O_2/N_2) and a laser repetition rate of 25 Hz.*

4, the in-plane cell parameter *a* of SLCO compounds is in the order of 3.95-4 Å, while for $SrTiO_3$ this value is 3.905 Å. Therefore, the heteropitaxial growth of SLCO on $SrTiO_3$ results in a compressive strain in the film due to substrate-film lattice-constant mismatch. After the initial decrease of the RHEED intensity, the film shows a layer-by-layer like growth, with intensity of the specular spot slightly increasing during subsequent deposition (Fig. 6.1). The higher amplitude of the oscillations for $x = 0.1$ films (Fig. 6.1a) is an indication of a decreased step density at the surface for films with $x > 0.1$. This is confirmed by the RHEED patterns of the films that show a smoother surface for $x = 0.1$ film characterized by a sharp and streaky RHEED pattern, with 2D dots (the insert in Fig. 6.1a), comparing with broader streaks for the $x = 0.15$ film (see the inset in Fig. 6.1b). When the surface mobility is no longer high enough to support 2D growth, a crossover to island growth takes place. This transition is driven by strain relaxation.

In conclusion, for the selected deposition conditions a true layer-by-layer growth of SLCO on $SrTiO_3$ was not possible by PLD.

To avoid the formation of 3D islands, PLiD was used. The required number of pulses to complete one deposition block (e.g., one-unit cell layers) was determined from continuous deposition runs. Different growth behaviours were observed depending on the level of La doping, deposition pressure and type of gas used. For films with doping level close to $x = 0.1$ a 2D growth could be sustained when interval deposition was used. For example, a time-scan of the RHEED pattern recorded during deposition of $Sr_{0.9}La_{0.1}CuO_2$ films on (001) $SrTiO_3$ at 550 °C and 5×10^{-2}-0.10 mbar O_2 (or O_2/N_2) is shown in Fig. 6.2. The RHEED pattern of the films showed only streaks, an indication of a smooth surface. For increased La concentration, a significant dependence of the film microstructure on deposition parameters (mainly oxygen partial pressure) was observed. A time scan of the intensity of the specular beam during heteroepitaxial

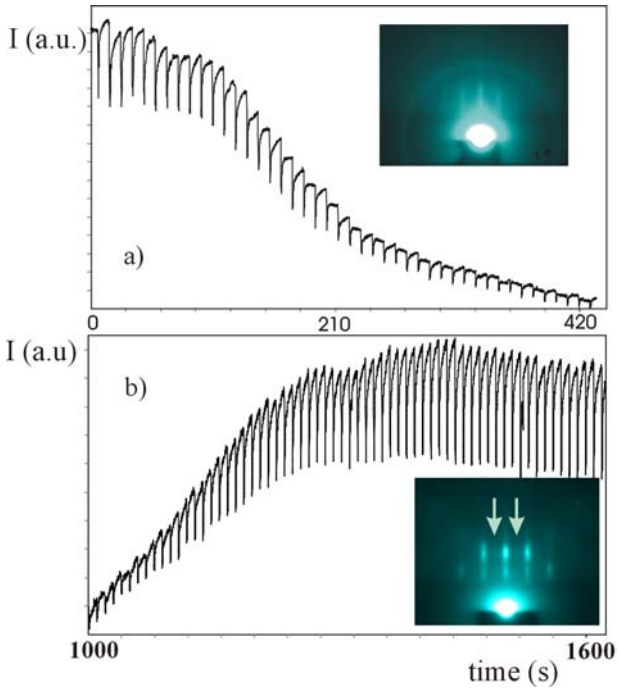

Fig. 6.3 *Evolution of the RHEED specular beam intensity oscillations [along (100) azimuth] during heteroepitaxial growth of $Sr_{0.85}La_{0.15}CuO_2$ film on SrO terminated $SrTiO_3$ and corresponding RHEED patterns before (a) and after strain relaxation (b).*

growth of $Sr_{0.85}La_{0.15}CuO_{2\pm\delta}$ on (100) $SrTiO_3$ by means of PLiD is given in Fig. 6.3. The film was deposited at a substrate temperature of 550 °C under a pressure of 0.10 mbar O_2/N_2. According to the variations of the RHEED oscillations, the strain relaxes after about 40 nm, followed by a significant RHEED signal recovery. In the first stage of growth, before relaxation, the intensity of the specular spot decreases continuously (see Fig. 6.3a).

After relaxation, the RHEED intensity increases constantly, during subsequent deposition, until it reaches a certain level. At this stage, the film growth follows a 2D growth mode. Before relaxation the RHEED patterns are characterized by streaks with low intensity due to an increased surface roughness with film thickness. The final RHEED pattern (Fig. 6.3b) showed only the formation of 2D diffraction dots on a streaky background, an indication of a flat surface. The RHEED data is confirmed by AFM analysis of the film surface (Fig. 6.4). The film is characterized by a smooth surface, with typical peak-to-valley values of ~ 1-2 nm. In conclusion, the presence of compressive strain, due to the lattice mismatch, results in formation of structural defects as a way for strain relaxation. The film relaxes after a critical thickness of about 100 unit-cells and surface morphology continuously improves during subsequent growth. When deposited under an oxygen atmosphere, the $x \geq 0.15$ SLCO films showed no relaxation (for thickness smaller than 50 nm). The RHEED signal decreases

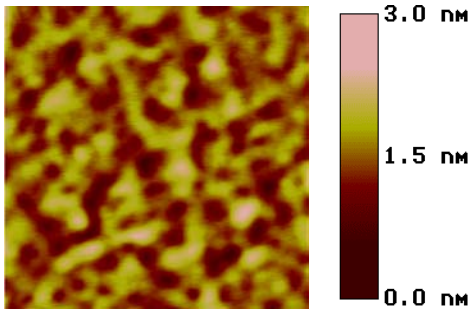

Fig. 6.4 *Topographic AFM image (0.5×0.5 μm²) of a ~ 90 nm thick $Sr_{0.85}La_{0.15}CuO_2$ film grown on SrO terminated $SrTiO_3$. Deposition parameters: T_s = 550 °C, P_d = 0.10 mbar O_2/N_2, f = 20 Hz.*

continuously, with no recovery at the end of deposition. In this case, the growth mode is dominated by island growth and coalescence.

The n-type IL phases are very difficult to be doped when grown under compressive strain conditions.[5,20,23,24] Therefore, $BaTiO_3$ was used as buffer layer in order to induce tensile strain in these SLCO films. Consequently, the CuO_2 planes are stretched and can be easier doped with electrons. The properties of SLCO thin films grown on $BaTiO_3$ buffered $SrTiO_3$ will be presented in section 6.2.3.

6.2.2.2 Structural analysis

Structural properties of the IL phases are strongly dependent on the actual oxygen content from the structure. The ideal (p- or n-type) $ACuO_2$ IL structure lacks oxygen in the A-cation(s) containing planes. The oxygen affinity of the A cations is higher than that of Cu or, in other words, the A-O bond forms easier that Cu-O one. In the same time, Ln cations used for substitution of Sr in the $Sr_{1-x}Ln_xCuO_2$ structure have a higher coordination number with oxygen than Sr. Therefore, it is expected that at the oxidation conditions used during deposition ($P_d = 10^{-2}$-0.40 mbar O_2 or O_2/N_2) the oxygen network to vary from the ideal case. For n-type IL a reduction step is generally used to eliminate the oxygen from apex positions in order to induce superconductivity. Concluding, deposition conditions as well as cooling procedure is expected to determine the final structural properties of the SLCO films.

6.2.2.2.i XRD

As was presented in the above section, deposition of the SLCO films was first performed in O_2/N_2 mixture[xiv] with cooling in N_2. For these films XRD, HREM and electron diffraction data showed that the IL phase in not stable. Instead, all films contained an ordered structure with unit cell $2\sqrt{2}a_p \times 2\sqrt{2}a_p \times c_p$ (a_p, b_p, and c_p represent the unit cell parameters of the film's perovskite subcell). As discussed in Chapter 2, the

[xiv] $Sr_{0.85}La_{0.15}CuO_2$ phase could not be stabilized when grown in a nitrogen atmosphere. XRD data showed that at these conditions the growth resulted in formation of a phase closed compositional to Sr_2CuO_3.

Table 6.3 *Phase composition of $Sr_{0.85}La_{0.15}CuO_2$ films versus deposition and cooling conditions.*

Deposition ambient	P_c	Annealing	Phase composition	Example
O_2/N_2	0.10-1 bar N_2	-	IL-r	Fig. 6.5a
O_2	~1 bar N_2	-	IL-r	Fig. 6.5a
O_2	< 20 mbar O_2, 0.10-1 bar N_2	for 1 h at 450-550 °C in air or N_2 (1 bar)	IL-r	Fig. 6.5b
O_2/N_2 (1:1)	0.10-1 bar N_2	-	IL + IL-r	Fig. 6.5c
O_2	< 4×10^{-1} mbar O_2	-	IL (+ IL-r)	Fig. 6.5c,d
O_2	< 20 mbar O_2	-	IL	Fig. 6.5e
O_2	< 20 mbar O_2	- less than 0.5 h at 450 °C and pressures less than 20 mbar O_2 - 0.25 h at 450 °C in air or N_2 (1 bar)	IL-r + IL	Fig. 6.5f

P_c = background pressure during sample cooling, IL = SLCO infinite layer, IL-r = the $2\sqrt{2}a_p \times 2\sqrt{2}b_p \times c_p$ superstructure phase.

formation of this superstructure[xv] is due to ordering of the oxygen vacancies in the CuO_2 planes. The composition of these oxygen-deficient SLCO films can be better expressed as $Sr_{1-x}La_xCuO_{(2+x/2)-\delta}$. The films are epitaxialy grown, with c-axis perpendicular to the surface of the substrate. For example, in Fig. 6.5a a θ-2θ scan of an $Sr_{0.85}La_{0.15}CuO_2$ film deposited at 550 °C and 7.5×10^{-2} mbar O_2/N_2 with subsequent cooling under 1 bar of N_2 is depicted. Under these conditions, the superstructure is readily formed for La concentration $x \geq 0.15$. The films are single phase. An increase of the value of the c-axis parameter was observed with La doping; it varied from c ~ 3.63 Å, for x = 0.15, to c ~ 3.715 Å, for x = 0.2. If these films are annealed ex-situ in air at 450-550 °C for 0.25-1 h the c-axis parameter increases further, while the a-axis parameter decreased to ~ 3.905 Å (the value of the in-plane axes of $SrTiO_3$), see Fig. 6.5b. After annealing the films are well crystallized, with c-axis length of ~ 3.7 Å. An increase of the (00l) SLCO peaks intensity was always observed after annealing due to improved crystallinity that can be explained by partial or complete strain release.

If the O_2/N_2 deposited films are cooled down in oxygen (at pressures < 20 mbar) partial formation of the IL was observed due to partial filling of the oxygen vacancies from the CuO_x planes (Fig. 6.5e). The value for the c-axis of the IL phase (c ~ 3.49 Å) is intermediate that of the tetragonal $SrCuO_2$ (3.45 Å) and that of a stoichiometric perovskite (3.8-3.9 Å).[25] Therefore, it is expected that excess oxygen is included in the Sr(La) planes during cooling in oxygen.

The structural properties of the SLCO films grown under oxygen atmosphere were studied further. The XRD data showed that the composition of the films depended on the oxygen pressure and the cooling procedure. Fig. 6.7 shows the c-axis lattice constant as a function of La content (x) and O_2 deposition pressure (P_d), as determined from θ-2θ

[xv] This superstructure is also known in literature as the infinite layer-related phase (IL-r).

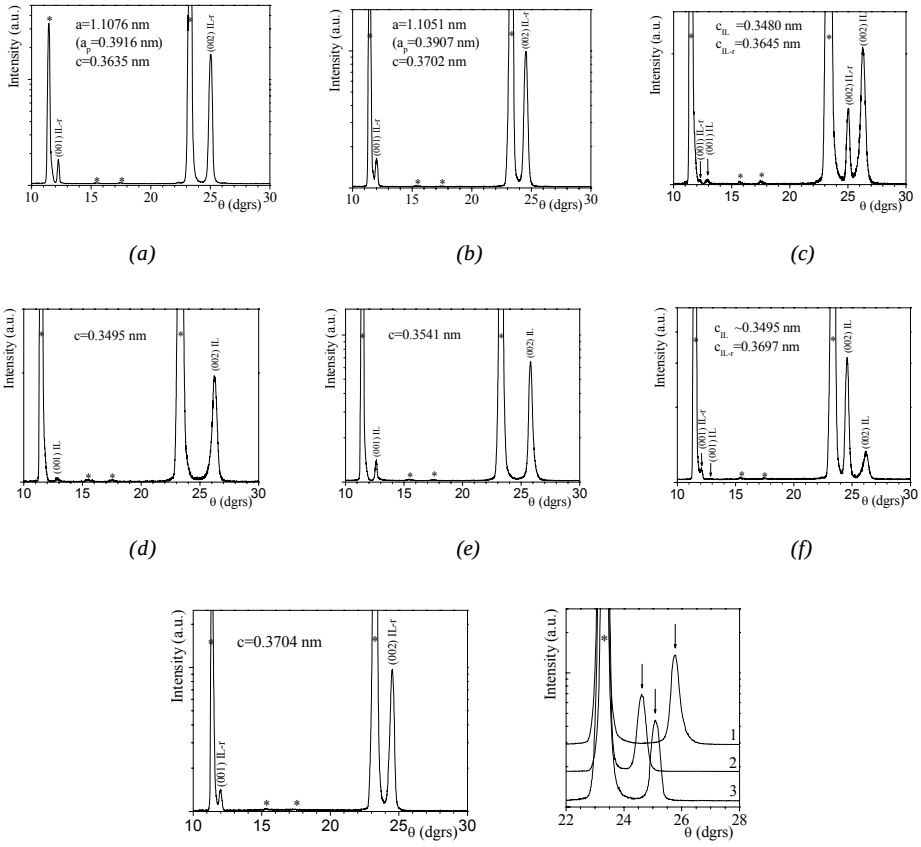

Fig. 6.5 *XRD θ-2θ patterns of $Sr_{0.85}La_{0.15}CuO_{2\pm\delta}$ thin films grown on (001) $SrTiO_3$ at 550 °C and (a) P_d= 0.75 mbar O_2/N_2, P_c=1 bar N_2; similar XRD patterns were observed for P_d = (1-5)×10^{-2} mbar O_2, P_c = 1 bar N_2. (b) P_d = P_c= 10^{-2}-0.40 mbar, and ex-situ annealed in N_2 or air at 550 °C for 1 h or longer. Films (a) and (b) showed metallic behaviour (see text). (c) P_d = 0.75 mbar O_2/N_2 (1:1), P_c = 0.2-1 bar N_2; similar mixed phase (IL and IL-r) patterns resulted for the films deposited in oxygen (P_d = 0.75-0.20 mbar) and cooled down under deposition pressure, with the concentration of the IL phase increasing with oxygen partial pressure. (d) P_d = P_c = 0.10 mbar O_2. (e) P_d = 5×10^{-2} mbar O_2; P_c = 10 mbar O_2. (f) P_d = 5×10^{-2} mbar O_2; mixed composition films (IL + IL-r). The film was annealed in situ for 0.5 h at 450 °C and 15 mbar O_2 and subsequently cooled down under the same pressure; the concentration of the IL phase increasing for higher partial oxygen pressure during deposition. Ex situ annealing of the as-deposited films at 450 °C in N_2 or air for short time period (~ 0.25 h) gave similar results. (g) P_d = 0.10 mbar O_2, cooled down in deposition pressure and ex-situ annealed 1 h at 450 °C in O_2 (400 l/h). These films showed high resistance after annealing (see text). Reflections corresponding to the (001) $SrTiO_3$ are marked with an asterix.*

P_d – deposition pressure; P_c – the pressure used during cooling of the films; IL – the infinite layer phase; IL-r – the $2\sqrt{2}a_p \times 2\sqrt{2}a_p \times c_p$ superstructure, with a_p, b_p, and c_p representing film's subcell parameters.

XRD scans. All films were grown on (001) $SrTiO_3$ at 550 °C and cooled down under deposition pressure. The values for the in plane cell parameters of SLCO films varied in the range of a ~ 3.92-3.95 Å, the highest values been observed for both low La doping (x closed to 0.1) and low oxygen deposition pressures. The smallest c-axis values were obtained for x = 0.1 and for lowest partial oxygen pressure during deposition. The films are single phase IL (see Fig. 6.5d and 6.6a), but the c-axis values[xvi] suggest the presence of excess oxygen in the Sr(La) planes. Further increase of the concentration on the apex oxygen was observed when the SLCO films are cooled under increased oxygen pressure (10-20 mbar, Fig. 6.5e), or if the as-deposited films are ex-situ annealed under oxygen (Fig. 6.5g). The composition of the oxygen annealed SLCO films can be better expressed as $Sr_{1-x}La_xCuO_{3-\delta}$; the oxygen positions in the CuO_2 planes are fully occupied in this case.

The phase composition of $Sr_{0.85}La_{0.15}CuO_2$ films grown on $SrTiO_3$ is given in Table 6.3 as function of deposition and cooling conditions, as well as of post-deposition annealing procedures. Deposition, cooling and/or annealing in an ambient containing N_2 resulted in formation of the $2\sqrt{2}a_p \times 2\sqrt{2}a_p \times c_p$ superstructure, as the primary or secondary phase. The IL phase forms readily under relatively low O_2 pressure (10^{-2}-0.10 mbar), with c-axis value decreasing with decreasing deposition pressure. The air or N_2 annealed x = 0.15-0.20 films contained only the superstructure phase (Fig. 6.5b), while for lower La doping (i.e., closed to x = 0.10) a longer annealing time (i.e., more than 1 h) and a higher annealing temperature (i.e., 550 °C) was required for complete conversion of the infinite layers structure to the superstructure phase.

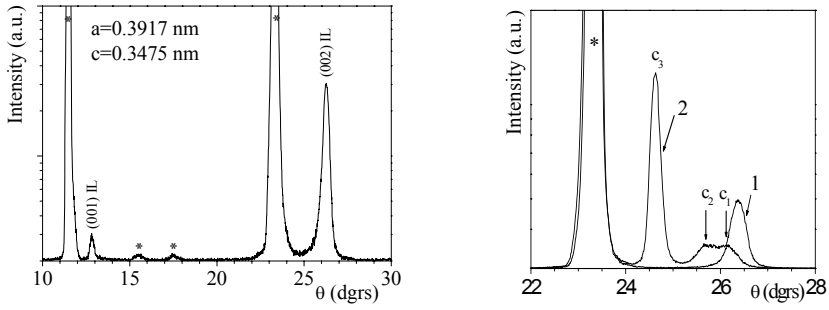

(a) *(b)*

Fig. 6.6 *$Sr_{0.9}La_{0.1}CuO_{2\pm\delta}$ thin films grown on (001) $SrTiO_3$ at 550 °C. (a) XRD θ-2θ pattern ($P_d = P_c = 0.20$ mbar O_2). (b) Evolution of the (002) reflections ($P_d = P_c = 0.10$ mbar O_2): (1) the as-deposited film (c = 3.455 Å) and (2) after annealing in air for 1 h at 550 °C. Three different phases (c_1 = 3.49 Å, c_2 = 3.53 Å, and c_3 = 3.69 Å), characterized by different concentration of the interstitial oxygen and vacancies in the CuO_2 plane, resulted after annealing. The reflections of the substrate are marked with asterix.*
P_d – deposition pressure; P_c – the pressure used during cooling of the films.

[xvi] These values are higher than that of the bulk samples with the same level of doping.

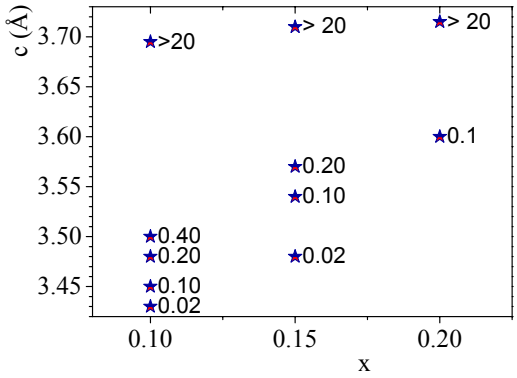

Fig. 6.7 *Evolution of the c-axis of $Sr_{1-x}La_xCuO_2$ films, grown on $SrTiO_3$ substrates, as a function of the oxygen deposition pressure (in mbar) and La content (x).*

Incomplete annealing resulted in formation of mixed-phase samples (infinite layer phase with different concentration of interstitial oxygen and superstructure phases), as can be seen for example in Fig. 6.6b for an x = 0.1 film.

It can be concluded that the formation of the $2\sqrt{2}a_p \times 2\sqrt{2}a_p \times c_p$ superstructure or IL phase depends on the partial oxygen pressure during deposition and subsequent annealing, as well as on the concentration of La. The c-axis parameter of both the superstructure and IL increases with La concentration and partial oxygen pressure during deposition. A. Gupta *et al.*[15] observed a similar increase of the c-axis with decrease of Sr concentration in PLD grown $Sr_{1-x}Sm_xCuO_y$ films on $SrTiO_3$. This evolution of the c-axis values with x cannot be explained based on ionic size alone since the ionic size of La is smaller than that of Sr; it is related to a systematic increase of oxygen content with increasing La content, as will be shown next by HREM data.

6.2.2.2.ii HREM

For films deposited under low oxygen partial pressure and either cooled down under N_2 or post-deposition annealed in O_2/N_2 (in situ) or air (ex situ) the HREM and ED images revealed the presence of an ordered structure. The cross-section HREM (Fig. 6.8a) and the [010]* ED (Fig. 6.8b) showed doubling of the unit cell along $[100]_{SLCO}$ (indicated by a white rectangle in Fig. 6.8a). The ED reflections of the $2a_p$ modulation are indicated by a filled arrowhead in Fig. 6.8b, while the patterns corresponding to the c-axis of the film (c_p) are indicated by an open arrowhead in the same figure. Planview ED patterns from Fig. 6.8d reveal a $2\sqrt{2}a_p \times 2\sqrt{2}a_p$ superstructure. Combining cross section and planview ED data, the superstructure unit cell was determined to be $2\sqrt{2}a_p \times 2\sqrt{2}a_p \times c_p$, with a_p, b_p, and c_p being the subcell parameters of the film. The superstructure unit cell and the perovskite mesh are indicated in Fig. 6.8c by white circles and black dots, respectively. This superstructure was absent in the x = 0.1 films deposited and/or annealed in oxygen.

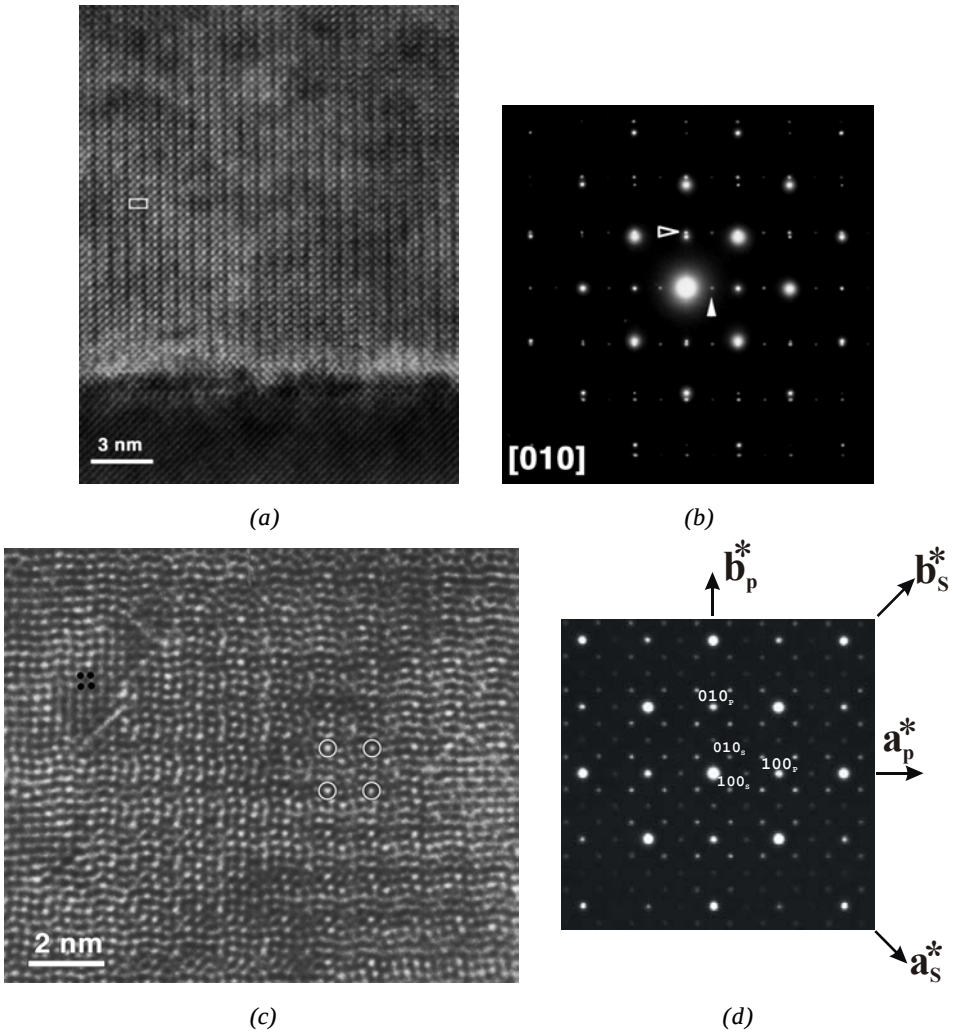

Fig. 6.8 *$Sr_{0.85}La_{0.15}CuO_2$ grown on SrO-terminated (001) $SrTiO_3$ (P_d = 0.75 mbar O_2/N_2, T_S = 550 ^oC, cooled down under 1 bar N_2). Cross-section HREM (a) and ED (b) showing the formation of a double cell ($2\times a_p$) superstructure. (c) Planview HREM (the perovskite cell of the infinite layer phase is indicated by black dots) and (d) [001] ED pattern of the $2\sqrt{2}a_p \times \sqrt{2}b_p$ superstructure. The $2\sqrt{2}a_p \times \sqrt{2}b_p$ superstructure is indicated by white circles in (c). Combining cross-section and planview ED data, the superstructure cell was determined to be $2\sqrt{2}a_p \times \sqrt{2}b_p \times c_p$ (p refers to the perovskite subcell and s to the supercell with a = $2\sqrt{2}a_p$ and c = c_p).*

At certain deposition conditions extended defects were observed, besides the $2\sqrt{2}a_p \times 2\sqrt{2}a_p \times c_p$ structure, as small domains in HREM images. This is illustrated in Fig. 6.9b-c where two kinds of defects can be observed. For example, the planview HREM image from Fig. 6.9c shows the presence of loops, which can be characterized as

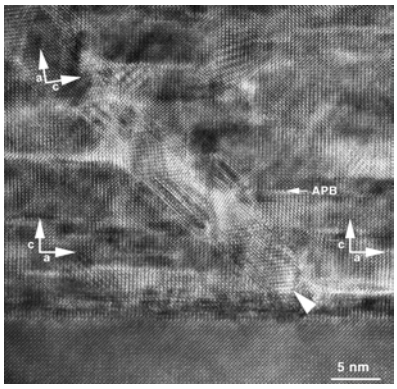

(a)

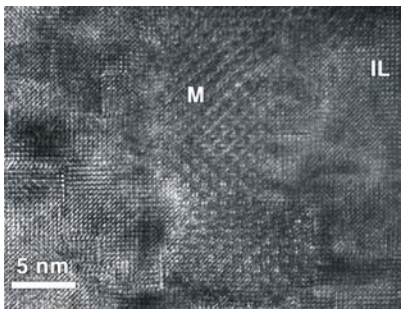

(b)

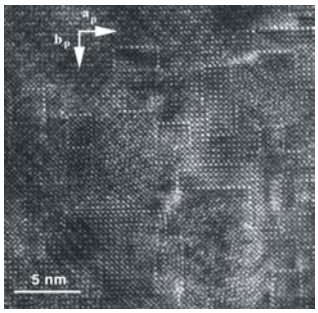

(c)

Fig. 6.9 *(a) Cross-section HREM of a $Sr_{0.9}La_{0.1}CuO_2$ film grown on $SrTiO_3$ (T_s = 550 °C, P_d = 0.20 mbar O_2, P_c = 20 mbar O_2). A twinning domain is indicated with an arrow head, while APB marks an antiphase boundary. (b) Plan view HREM of a $Sr_{0.85}La_{0.15}CuO_2$ film grown on $SrTiO_3$ (T_s = 550 °C, P_d = 7×10^{-2} mbar O_2/N_2 (1:1), P_c = 1 bar N_2).*

double Cu-layers from image simulations. The loops have their edges parallel to the perovskite direction. The superstructure modulation is not present within the loops. This type of defect was also observed by Mercey *et al.*[25] in $Sr_{1-x}Sm_xCuO_2$ infinite layers for $x = 0.25$. The domains within the loops correspond to the column observed in cross section. These domains are associated with the antiphase boundaries observed at the edge of the columnar defects in cross section.

The cationic array in the defect structure marked *M* in Fig. 6.9b can be described[25] by the stacking along $[100]_p$ of identical $[La\text{-}Sr\text{-}Sr\text{-}Sr]_\infty$ rows; two successive double rows are shifted by $2b_p$ with respect to each other, leading to the stacking sequence $[La\text{-}La\text{-}Sr\text{-}Sr]_\infty$. Besides these rows, pure $[Sr]_\infty$ exists in the structure. The idealized model for this defect structure, proposed by Mercey *et al.*[25] for $Sm_2Sr_6Cu_8O_{17}$, is shown in Fig. 6.10. With respect to $SrCuO_2$ structure, excess oxygen is introduced between the $(001)_p$ layers by Ln ions, because of its higher valence as compared to Sr. Consequently, Ln (here La) ions form pairs, located in sites of six-sided tunnels build up from two

CuO_5 piramids and four CuO_4 square planar groups (Fig. 6.10a). In this configuration, Sr ions exhibit either a pseudo-cubic eightfold-coordination similar to that observed in $SrCuO_2$, or a ninefold-coordination. The structure of this defect phase, shown in Fig. 6.10b, was deduced from the $SrCuO_2$ structure by replacing one $[CuO_2]_\infty$ row of CuO_4 group out of two by one $[Cu_4O_9]_\infty$ row built up from strings of four polyhedra (two CuO_4 square groups and two CuO_5 groups).[25] In the recorded HREM images, this idealized framework is slightly distorted due to ordering of La and Sr atoms and, also, of the oxygen atoms and vacancies.[25] The entire structure can be represented by the formulation $[Sr_3La]_2[CuO_2]_4[Cu_4O_9]$, i.e., $La_2Sr_6Cu_8O_{17}$ characterized by a mixed Cu^{2+}/Cu^{3+} valence. This structure is made from the intergrowth along $[010]_p$ of two kinds of chains, $[CuO_2]_\infty$ and $[Cu_4O_9]_\infty$, with two successive $[CuO_9]_\infty$ chains shifted by $2b_p$ with respect to each other.[25]

Low magnification cross-section overview of an $Sr_{0.85}La_{0.15}CuO_2$ film grown in O_2/N_2 and cooled down under a pressure of 1 bar N_2 is shown in Fig. 6.11a. Structural defects, like twinning, were observed after a layer thickness of ~ 10-20 nm. After the film relaxes, confirming the RHEED observations (see Fig. 6.3), a layer free of structural defects is formed, as can be observed in Fig. 6.11a. For $x \geq 0.15$ films deposited under oxygen or O_2/N_2 and post-deposition annealed in situ in a mixture of O_2/N_2 at relatively low pressures (~ 10 mbar) HREM micrographs revealed a mixed composition (infinite layer and superlattice phase, see Fig. 6.11d). These annealed films were characterized by a lower concentration of defects compared with the non-annealed ones (deposited under similar conditions). For the $x = 0.15$ films deposited in oxygen TEM data showed the formation of columnar defects (Fig. 6.11b and d). These structural defects formed after a film thickness of about 10 - 20 nm. RHEED data of the as-deposited film (Fig. 6.11c) show only the formation of the perovskite structure, with no presence of the $2\sqrt{2}a_p \times 2\sqrt{2}a_p \times c_p$ superstructure. Formation of twinning was the preferred stress release mechanism observed in $x = 0.1$ films deposited under oxygen pressure (Fig. 6.11e and Fig. 6.9a).

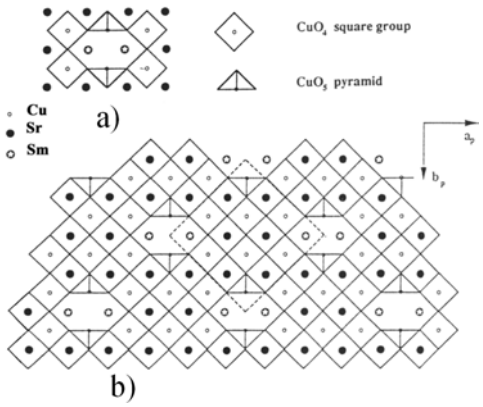

Fig. 6.10 *Structural model for "$La_2Sr_6Cu_8O_{17}$" defects. (a) Formation of a six-sided tunnel through the presence of additional oxygens in the infinite layer structure. (b) Idealized model viewed along [001]; the supercell is drawn with doted lines (Ref. 25).*

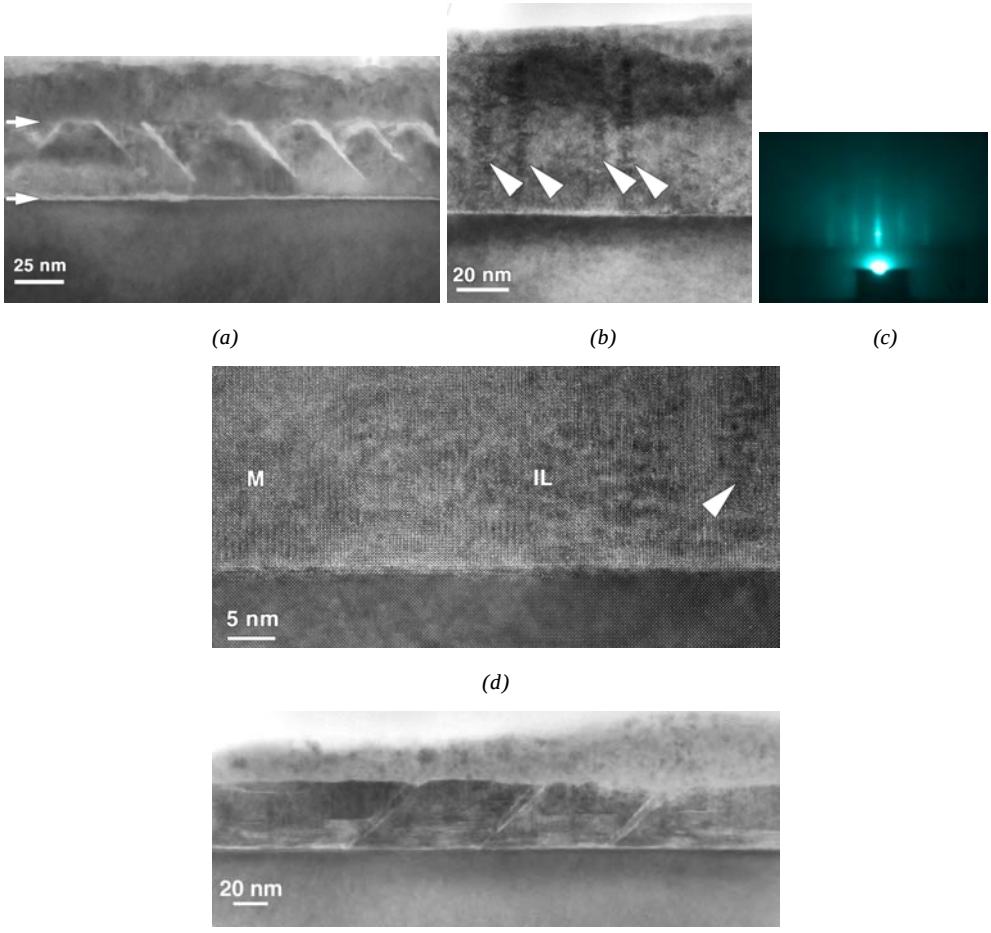

Fig. 6.11 *Structural data of $Sr_{1-x}La_xCuO_2$ films. (a) Low magnification cross-section electron microscopy showing the formation of pyramidal-shaped defects for $Sr_{0.85}La_{0.15}CuO_2$ (P_d = 0.75 mbar O_2/N_2, cooled down under 1 bar N_2). (b) Low magnification cross-section electron microscopy showing the formation of columnar-type defects marked with arrowheads. (c) RHEED pattern of a $Sr_{0.85}La_{0.15}CuO_2$ film before cooling ($P_d = 2\times10^{-2}$ mbar O_2, cooled down under 1 bar N_2). (d) cross-section HREM indicating a mixed phase sample (the infinite layer phase, marked IL, and the $2\sqrt{2}a_p \times 2\sqrt{2}b_p \times c_p$ modulated structure, marked M, where a_p, b_p, and c_p are the subcell parameters) and the presence of columnar-type defects, marked with an arrowhead for $Sr_{0.85}La_{0.15}CuO_2$ (P_d = 0.75 mbar O_2; the film was annealed in situ for 1 h at 450 °C and 15 mbar O_2/N_2 and subsequently cooled down under the same pressure). (e) Low magnification cross-section electron microscopy showing the formation of twinning domains for $Sr_{0.9}La_{0.1}CuO_2$ (P_d = 0.20 mbar O_2, cooled down under 25 mbar O_2).*
The (a) and (b) films were grown on SrO-terminated (001) $SrTiO_3$, while the (d) and (e) films were deposited on vacuum annealed (001) $SrTiO_3$, all at T_s = 550 °C.

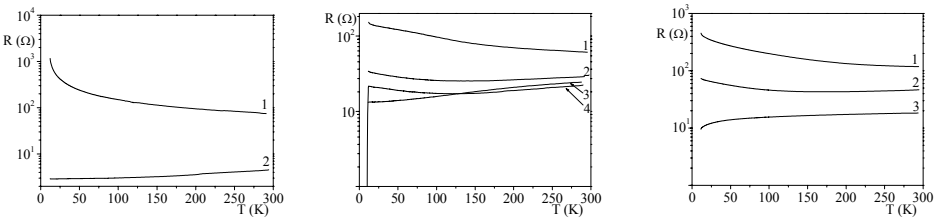

Fig. 6.12 *Temperature dependence of resistance of (a) $Sr_{0.85}La_{0.15}CuO_2$ deposited on $SrTiO_3$ (T_s = 550 °C, P_d = P_c = 0.10 mbar O_2); the as-deposited film (1), after post-deposition annealing for 0.5 h at 450 °C, in air or in 1 bar N_2 (2). (b) $Sr_{1-x}La_xCuO_2$ with different La content (x = 0.1-0.2) grown on $BaTiO_3/SrTiO_3$ (T_s = 550 °C, P_d = 10^{-3} mbar O_2). x = 0.10 (1), x = 0.15 (2) and (4), x = 0.20 (3). Cooling pressure was 10^{-3} mbar O_2 for films 1-3 and 5×10^{-4} mbar O_2 for (4). For films (1-3) the thickness of the $BaTiO_3$ layer was ~ 7 nm, with no post-deposition annealing. A $BaTiO_3$ layer with thickness of ~ 25 nm was used for film (4). The $BaTiO_3$ layer was annealed 1 h at 900 °C in vacuum prior deposition of SLCO film. (c) $Sr_{0.85}La_{0.15}CuO_2$ deposited on $BaTiO_3/SrTiO_3$ (T_s = 550 °C, P_d = 5×10^{-3} mbar O_2 + 10% O_3; the thickness of the $BaTiO_3$ layer was ~ 7 nm; no post-deposition annealing of $BaTiO_3$). The SLCO films were cooled down in 1.2×10^{-2} mbar O_2 (1), 2×10^{-3} mbar O_2 (2), and 5×10^{-4} mbar O_2 (3).*

6.2.2.3 Electrical properties

Electrical resistance of the films was measured by a conventional dc four-probe method. A He cryostat was used for transport measurements at temperatures down to 10 K. The measurements showed a progressive reduction of resistance with increasing La concentration. The films with x = 0.20 showed metallic behaviour, while the as-deposited films with x = 0.1-0.15 showed semiconducting properties (see Fig. 6.12a1), the resistance increasing with decreasing La concentration. The semiconducting films become metallic after annealing in N_2, air or O_2/N_2, as shown in Fig. 6.12a2. The variation of the resistance with La doping suggests electron doping through the substitution of La^{3+} for Sr^{2+}. The electrical resistance decreased with increasing of the a-axis and decreasing of c-axis values, which can be explained by an increased concentration of the charge carrier (electrons) in CuO_2 planes. This dependence is different from the evolution of T_c in bulk samples for which the Ln content does not significantly affect T_c.

There are several possible reasons for the lack of superconductivity in the SLCO (x = 0.1-0.2) films grown by PLD on $SrTiO_3$. First, as resulted from structural data, the $Sr_{1-x}La_xCuO_{2\pm\delta}$ films on $SrTiO_3$ are epitaxially strained, and have a smaller in-plane lattice constant and a larger c-axis lattice constant than the bulk values. The relaxation of the lattice mismatch between the film and substrate is insufficient and makes difficult electron doping of the CuO_2 planes. Second, the presence of impurity phases, such as the $2\sqrt{2}a_p \times 2\sqrt{2}a_p \times c_p$ superstructure (characterized by oxygen deficiency) and the other defect structures (characterized by cation deficiency) observed by HREM can

suppress superconductivity. The cation deficiency at the A site cause a decrease in the carrier concentration leading to suppression of the a-axis expansion.

It can be concluded that $Sr_{1-x}La_xCuO_{2\pm\delta}$ (x = 0.1-0.2) thin films grown on (100) $SrTiO_3$ by PLD are epitaxially strained. Electrical resistance of the x < 0.2 SLCO IL films showed a semiconductive behaviour, with the resistance decreasing with La doping. The x = 0.2 films were metallic. Impurity phases formed due to oxygen vacancies, cation deficiency, as well as excess oxygen in the Sr(La) planes all resulted in suppression of superconductivity. No superconductivity was observed for these films.

6.2.3 $Sr_{1-x}La_xCuO_2$ on $BaTiO_3$-buffered $SrTiO_3$

Markert *et al.*[26] predicted that substrates with in-plane cell parameters of ~ 3.99 Å are required in order to provide sufficient extension of the Cu-O-Cu bond to promote adequate electron doping of the $Sr_{1-x}Ln_xCuO_2$ compounds. Therefore, $BaTiO_3$ was selected as buffer layer for PLD grown SLCO films on $SrTiO_3$ substrates. $BaTiO_3$ satisfies the cell parameter requirement (it has a~4.02 Å, in bulk) and it is chemically compatible with SLCO. The results on the structural and electrical properties of the SLCO films grown on $BaTiO_3/SrTiO_3$ will be presented and discussed in this section.

The typical deposition parameters of $BaTiO_3$ were presented in section 6.2.1. After growth, the $BaTiO_3$ layers were annealed in situ. As a result, c-axis oriented $BaTiO_3$ films, with tetragonal[xvii] symmetry, were obtained. The evolution of the intensity of the specular beam recorded during heteroepitaxial growth of $BaTiO_3$ on (001) $SrTiO_3$ substrate is shown in Fig. 6.13. The layer was deposited at 700 °C and 0.10 mbar O_2 using a laser repetition rate of 3 Hz. A transition from 2D to 3D (island) growth can be observed after ~ 10 unit cells. At the point of transition, the film relaxes and RHEED pattern shows the formation of a superstructure. An increase of the film roughness is observed after relaxation, probably due to the formation of structural defects such as dislocations. A better morphology for the $BaTiO_3$ layers was observed with increasing deposition temperature (up to 825 °C) and lower laser repetition rates (1 Hz), as shown by the RHEED data (Fig. 6.14a). A higher surface mobility is expected in this case, associated with a longer time available for the deposited material to diffuse. However, independent on the deposition conditions, after a certain critical thickness the film relaxes, the roughness increases with thickness due to formation of precipitates. The RHEED pattern of such surface shows the formation of 3D dots with cell parameters that do not correspond to the $BaTiO_3$ phase (Fig. 6.14b). Improvement of the film quality was observed after an annealing step in vacuum for 0.5-1 h at temperatures in range of 900-950 °C, as can be seen from the RHEED pattern (Fig. 6.14c). However, thick $BaTiO_3$ layers free of defects were difficult to be obtained even after vacuum annealing.

After deposition of the buffer layer, the $Sr_{1-x}La_xCuO_2$ thin films were grown by standard PLD at a laser repetition rate of 5 Hz. The deposition pressure was varied in the range 10^{-3}-0.4 mbar O_2 or O_2/O_3 (max. 10% O_3), while the substrate temperature was

[xvii] The bulk $BaTiO_3$ has a cubic symmetry with a ~ 4.02 Å. However, due to the presence of compressive strain the $BaTiO_3$ films grown on $SrTiO_3$ show a tetragonal symmetry with unit cell parameters dependent on the layer thickness.

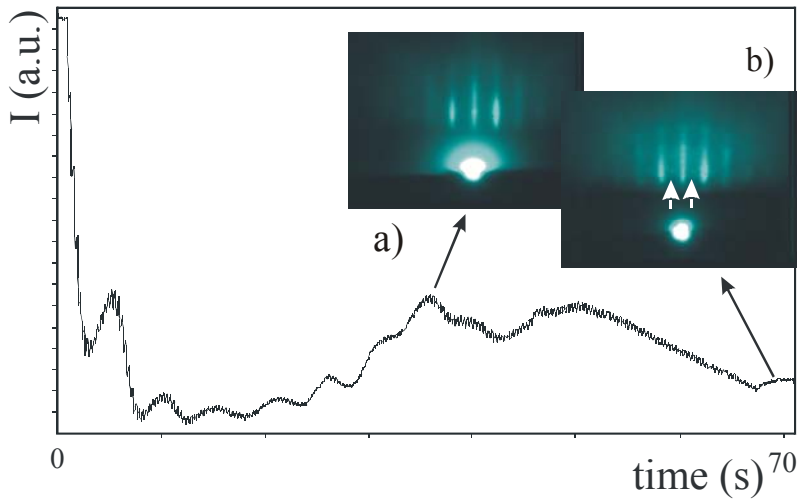

Fig. 6.13 *Evolution of the specular spot intensity during deposition of ~ 7 nm $BaTiO_3$ on $SrTiO_3$ and the RHEED patterns before film's relaxation (a) and at the end of deposition (b). The layer was grown at 0.10 mbar O_2 and 700 °C with a laser repetition rate of 3 Hz. The reflections coming from a superstructure are marked with white arrows.*

set at 550 °C. The use of a larger deposition range was motivated by the fact that, as resulted from section 6.2.2.3, the SLCO phase with lowest c-axis could be stabilized at lowest partial oxygen pressures. The rest of the deposition parameters were the same as those given in Table 6.1.

According to RHEED data, at initial growth stage the SLCO films deposited on $BaTiO_3$-buffered $SrTiO_3$ show a switch in the growth mode, from a layer-by-layer like to island growth. This transition, however, takes place after a larger critical thickness than in case of deposition on non-buffered $SrTiO_3$. The increased critical thickness can be explained by a higher SLCO phase stability when deposited on $BaTiO_3/SrTiO_3$ due to a reduced lattice mismatch induced by the buffer layer. As a result, the films contain less defects and the final surface morphology is improved.

6.2.3.1 Structural properties

Fig. 6.15a shows θ-2θ XRD scans for SLCO films with different La content (x = 0.1-0.2) grown on $BaTiO_3$-buffered $SrTiO_3$ at 550 °C under 10^{-3} mbar O_2. After deposition, the films were cooled down inside the deposition chamber down to 450 °C and then placed in loadlock. The cooling pressure was the same as during deposition. Single-phase IL structure was obtained applying these conditions for $0.1 \leq x < 0.2$, as can be seen in Fig. 6.15a. By contrast, on $SrTiO_3$ single-phase IL films was obtained for x close to 0.15. The difference in stability of the IL structure in terms of La doping on $BaTiO_3/SrTiO_3$ and $SrTiO_3$ can be explained by the difference in lattice parameters. For increased La concentration, the (00l) diffraction lines of the IL phase become slightly broader. The cell parameters for the IL phase at the deposition conditions presented in Fig. 6.14a were a ~ 3.955 Å and c ~ 3.41 Å, respectively, with c-axis increasing

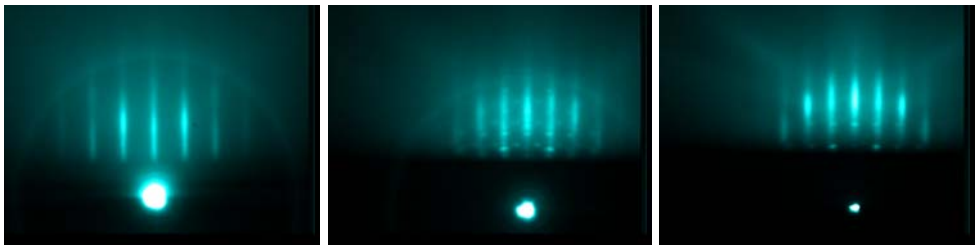

(a) *(b)* *(c)*

Fig. 6.14 *RHEED patterns of $BaTiO_3$. (a) 8 nm layer (T_s = 750 °C). (b) 20 nm layer - as deposited (T_s = 850 °C). (c) Film (b) after annealing for 0.5 h at 925 °C, 5×10^{-6} mbar. All films were deposited on as-received (001) $SrTiO_3$, P_d = 0.10 mbar O_2, f = 1 Hz.*

monotonically with La concentration. These values are close to the cell parameters of the bulk SLCO.

The films become mixed phase for x close to 0.2, a secondary phase (the so-called the long c-axis phase)[5] with c ~ 3.6-3.7 Å being formed, as can be seen in Fig. 6.15a. The composition of the SLCO films grown on $BaTiO_3/SrTiO_3$ was strongly dependent not only on the deposition conditions (substrate temperature, oxygen partial pressure), but also on the cooling procedure. The oxygen pressure used during cooling and the temperature at which the samples were placed in loadlock[xviii] were important conditions for yielding single-phase infinite-layer SLCO films. As will be shown in next section (SLCO on $KTaO_3$), the as-deposited films contain only the long c-axis phase, characterized by the presence of oxygen vacancies in the CuO_x planes[xix]. During cooling, these vacancies have to be filled with oxygen in order to obtain the infinite layer phase. Therefore, the cooling pressure and temperature are critical parameters during this step. As an example, in Fig. 6.15b are shown the XRD patterns of two $Sr_{0.85}La_{0.15}CuO_2$ films not optimally cooled down. Due to the incomplete oxidation of the CuO_x planes (short cooling time), a film with mixed composition resulted (Fig. 6.15b1). Furthermore, a too low cooling pressure associated with an annealing step leads to formation of the long c-axis phase (Fig. 6.15b2). In conclusion, a high deposition pressure (P_d > 2×10^{-3} mbar O_2) associated with wrong cooling procedure (temperature, pressure) lead to formation of impurity phases.

[xviii] Faster cooling was achieved by placing the samples in loadlock in order to avoid incorporation of excess oxygen. Consequently, it was possible to quench the structure of the films after the cooling step inside the chamber.

[xix] The long c-axis phase has an ordered-oxygen vacancies structure similar with that of the $2\sqrt{2}a_p \times 2\sqrt{2}a_p \times c_p$ superstructure observed for SLCO films grown on $SrTiO_3$ under O_2/N_2. The difference between these structures is given by the in-plane cell parameters of the subcell, a_p > 3.95 Å, for the long c-axis structure, and a_p ~ 3.905 Å, for the $2\sqrt{2}a_p \times 2\sqrt{2}a_p \times c_p$ superstructure, respectively. Their electrical properties are also different (see further).

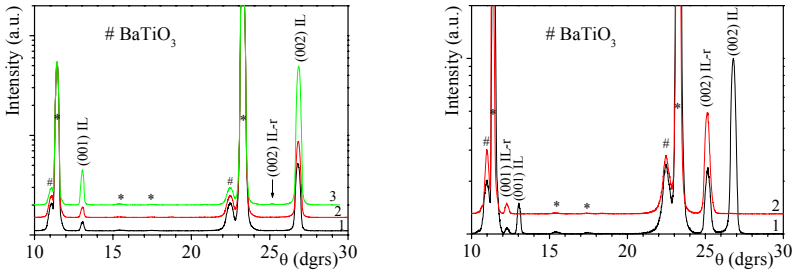

(a) *(b)*

Fig. 6.15 *XRD patterns of $Sr_{1-x}La_xCuO_2$ thin films with different La content (x = 0.1-0.2) grown on $BaTiO_3$-buffered $SrTiO_3$. (a) x = 0.1 (1), x = 0.15 (2), and x=0.2 (3). All films were deposited at T_s = 550 °C and $P_d = P_c = 10^{-3}$ mbar O_2, with cooling inside deposition chamber. The samples were moved in loadlock at 450 °C. b) x = 0.15, T_s = 550 °C, $P_d = 2.5\times10^{-3}$ mbar O_2, and (1) $P_c = 10^{-4}$ mbar O_2. The sample was moved in loadlock at 525 °C; (2) $P_c = 10^{-4}$ mbar O_2 and 10 min annealing under cooling pressure. The sample was moved in loadlock at 400 °C.*
P_c represents the pressure used during cooling down. The diffraction peaks coming from the $SrTiO_3$ are marked with an asterix. Il-r represents the long c-axis phase (see text).

6.2.3.2 Electrical properties

Fig. 6.12b shows the temperature dependence of resistance for SLCO films with different La content grown on $BaTiO_3/SrTiO_3$. The resistance decreases monotonically with doping level. When deposited on not-annealed $BaTiO_3$ layers, the SLCO films show a semiconductor like behaviour[xx], except for La concentration close to 0.2. In this case, the films showed metallic behaviour. Superconductivity ($T_{c,zero} \sim 10$ K) was observed in $Sr_{0.85}La_{0.15}CuO_2$ films grown on vacuum annealed $BaTiO_3$ layers[xxi]. The thickness and quality of the buffer layer were important parameters for obtaining superconductivity in the SLCO films.

A dependence of the electrical properties on the cooling procedure was observed, as was expected from the dependence of the phase composition with cooling procedure. The resistance of the films decreased with decreasing the oxygen partial pressure during cooling down. As can be observed in Fig. 6.12c for $Sr_{0.85}La_{0.15}CuO_2$ films grown at 5×10^{-3} mbar O_2/O_3, their resistance decreased with decreasing the cooling pressure from 1.2×10^{-2} mbar to 5×10^{-4} mbar O_2. This can be explained by the concentration of the apex-oxygen, the lower the pressure during cooling, the less probable these oxygen positions to be filled. However, vacuum cooling or annealing of the SLCO films resulted in semiconducting properties, with no traces of superconductivity. The orthorhombic deformation of the tetragonal SLCO unit cell resulted after this vacuum annealing or

[xx] This behaviour was obtained independent on the $BaTiO_3$ layer thickness.

[xxi] The thickness of the buffer layer was of ~ 25 nm. The annealing was performed at a substrate temperature of 900 °C and a pressure of ~ 10^{-6} mbar, with a minimum annealing time of 1 h.

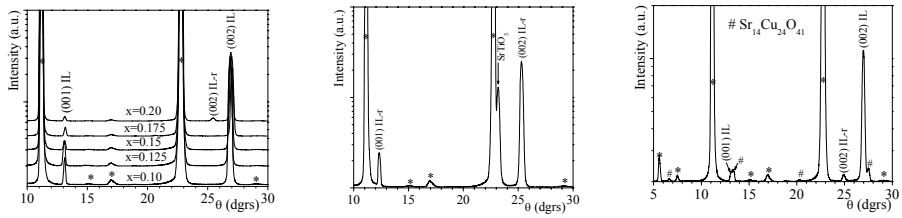

(a) *(b)* *(c)*

Fig. 6.16 *θ-2θ XRD patterns of (a) $Sr_{1-x}La_xCuO_2$ thin films with different La content (x = 0.1-0.2), (b) $Sr_{0.85}La_{0.15}CuO_2$ with $SrTiO_3$ top layer (the long c-axis phase marked with IL-r, with a ~ 3.990 Å, and c ~ 3.620 Å), and (c) $Sr_{0.85}La_{0.15}CuO_2$, showing the formation of two secondary phases: the long c-axis phase (IL-r) and $Sr_{14}Cu_{24}O_{41}$. The cell-parameters of the IL phase are: a = 3.971 Å, and c = 3.402 Å.*
The films were grown on (001) $KTaO_3$. Deposition conditions: (a) and (b) T_s = 550 °C, P_d = 10^{-3} mbar O_2, cooled down under deposition pressure and placed in loadlock at 425 °C. (c) T_s = 550 °C, P_d = 5×10^{-3} mbar (O_2+10%O_3), cooled down under 10^{-3} mbar O_2 and placed in loadlock at 400 °C. The reflection peaks corresponding to the substrate are marked with an asterix.

cooling step suggests formation of oxygen vacancies in the CuO_x planes. This in return will destroy superconductivity.

In conclusion, for SLCO films deposited on $BaTiO_3$ buffered $SrTiO_3$ the CuO_2 planes are under tensile stress, which makes more amenable the electron doping. The *a*-axis length, which is strongly related to the Cu-O bond length in the basal plane, was easily expanded with La substitution. Superconductivity was observed for x = 0.15 films, when grown on vacuum annealed $BaTiO_3$ buffer layers. Metallic behaviour was observed for a La concentration x close to 0.2, while the $x < 0.15$ films showed semiconducting behaviour.

6.2.4 $Sr_{1-x}La_xCuO_{2\pm\delta}$ on $KTaO_3$

In previous section of this chapter, it was shown that the $Sr_{1-x}La_xCuO_2$ films grown on (100) $SrTiO_3$ are under epitaxial compressive strain. Partial relief of the compressive strain was obtained by optimising the deposition parameters while $BaTiO_3$ buffer layer was used, with partial success, to induce tensile stress. To induce growth under tensile strain $KTaO_3$ was used as substrate. In this section, the results of SLCO deposited on $KTaO_3$ substrates (with or without a $BaTiO_3$ as buffer layer) will be presented, with accent on the role of the substrate characteristics on the morphological, structural, and electrical properties of the film.

6.2.4.1 Structural properties

The XRD, HREM and electron diffraction data for the $Sr_{1-x}La_xCuO_2$ films grown on $BaTiO_3$ buffered (100) $KTaO_3$ at optimum conditions showed the formation of single-phase IL films for $0.1 \le x < 0.2$. As was discussed in section 6.2.3.1, the increased

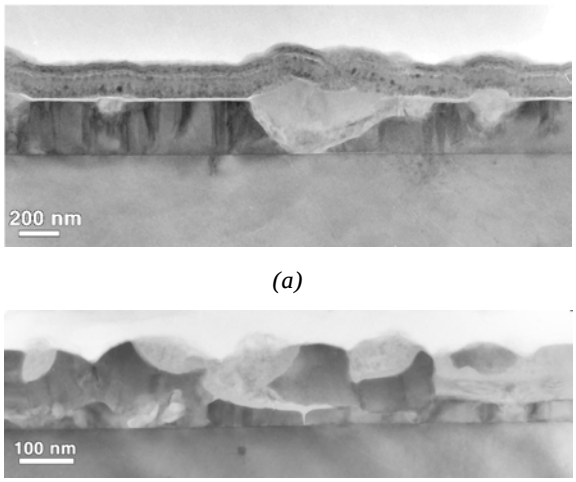

Fig. 6.17 *Low magnification cross-section electron microscopy of $Sr_{0.85}La_{0.15}CuO_2$ grown on vacuum annealed (001) $KTaO_3$. (a) T_S = 550 °C, P_d = 10^{-3} mbar O_2, cooling pressure 2×10^{-3} mbar O_2. (b) T_S = 550 °C, P_d = 10^{-3} mbar O_2+2% O_3, cooling pressure 10^{-3} mbar O_2.*

stability of $Sr_{1-x}La_xCuO_2$ infinite-layer phases for doping levels closed to 0.2[xxii] can be explained by the stability effect induced by the $KTaO_3$ substrate. The films are under tensile strain in the in-plane direction and compressed in the c-axis direction due to lattice mismatch.

The structural properties of the films were strongly dependent on the KTO surface morphology, the oxygen partial pressure during deposition and subsequent cooling. The as-deposited films consist of a long c-axis phase, considered a superstructure resulted from ordered oxygen vacancies in the CuO_x planes. This phase could be 'quenched' by deposition on top of the as deposited SLCO film of an $SrTiO_3$ layer (see Fig. 6.16b). At optimum deposition and cooling conditions single-phases IL SLCO films can be obtained for $x < 0.2$ (see Fig. 6.16a). Besides the infinite layer, the longer c-axis phase[xxiii] and $Sr_{14}Cu_{24}O_4$ or $(Sr,La)_{14}Cu_{24}O_{41}$ were present in some of the films (see, e.g., Fig. 6.16c). The formation of the latter secondary phases[xxiv] is related with Sr deficiency due to not optimum deposition conditions - the energy of the ablated species and the activity of the oxygen during deposition are too low to form the IL phase, the $(Sr,La)_{14}Cu_{24}O_{41}$[xxv] phase being more stable than IL.[23] The $Sr_{14}Cu_{24}O_{41}$ phase, first synthesized by Siegrist *et al.*,[27] was observed before in other $SrLnCuO_2$ films.[23] The b-axis of the $(Sr,La)_{14}Cu_{24}O_{41}$ is perpendicular to the substrate surface, while either a- and c-axes parallel to one of the

[xxii] Compared to a maximum solubility limit lower than 0.15 for bulk samples.

[xxiii] This is the same secondary phase observed in the SLCO films grown on $BaTiO_3/SrTiO_3$. It has both *a*- and *c*-axes larger than that of the SLCO IL phase.

[xxiv] These secondary phases were observed mainly observed in x = 0.15 SLCO films.

[xxv] $Sr_{14}Cu_{24}O_{41}$ has a face-centered-orthorombic symmetry (space group Fmmm) with cell parameters a = 11.459 Å, b = 13.368 Å, and c = 3.931 Å.[27,28]

in-plane crystal axes of the (001) $KTaO_3$ substrate. An increased of the concentration of the secondary phases was observed for films deposited in a mixture of oxygen and ozone (see Fig. 6.17b, 6.18a and b). These films showed a rough surface morphology, as confirmed by the AFM and RHEED data. Some of the films deposited under O_2/O_3 mixture also contained small amounts of $Sr_{2-x}La_xCuO_{3\pm\delta}$ (Fig. 6.18b)[xxv]. Except these secondary phases, CuO_x precipitates were also observed in RHEED patterns.

When the $KTaO_3$ substrate were chemically or thermally treated before deposition, the θ-2θ XRD scans showed the formation of the infinite layer phase for $0.1 \leq x < 0.2$ (Fig. 6.16). Similar with the results of SLCO grown on $BaTiO_3/SrTiO_3$, when La content is closed to 0.20 the long c-axis phase was present in the films. Its formation and concentration depends on the deposition pressure and cooling procedure, similar with the case of SLCO grown on $BaTiO_3/SrTiO_3$.

6.2.4.2 Electrical properties

The electrical measurements showed that the room temperature resistance of $Sr_{1-x}La_xCuO_{2\pm\delta}$ films deposited on $KTaO_3$ decreases monotonically with doping level. Semiconducting behaviour was observed for x = 0.10 films, while x ~ 0.20 films showed a metallic behaviour. The x = 0.15 films deposited and cooled down under 10^{-3} mbar O_2 (T_s = 550 °C) showed superconductivity with $T_{c,zero}$ of ~ 13 K. A small increase of T_c was observed after these films were reduced for 10 min at 550 °C and 3×10^{-4} mbar O_2, as shown in Fig. 6.23a. These films have a $T_{c,onset}$ ~ 18 K and $T_{c,zero}$ ~ 16 K. However, the

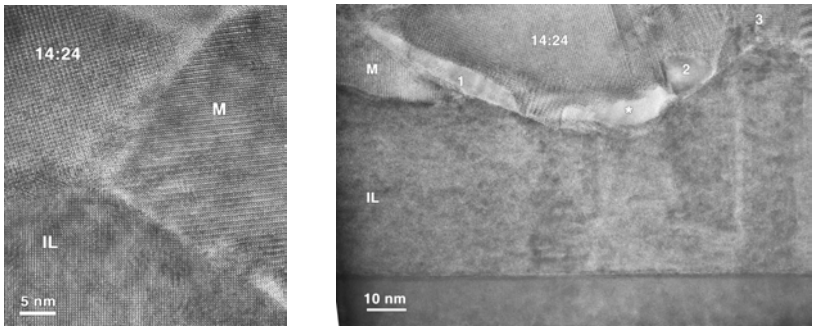

(a) *(b)*

Fig. 6.18 *Cross section HREM of $Sr_{0.85}La_{0.15}CuO_2$ grown on vacuum annealed (001) $KTaO_3$ ($P_d = 10^{-3}$ mbar O_2, T_S = 550 °C, cooling pressure 2×10^{-3} mbar O_2) showing (a) a multiphase film: infinite-layer IL, the modulated structure M, and $Sr_{14}Cu_{24}O_{41}$, marked as 14:24, and (b) T_S = 550 °C, $P_d = 10^{-3}$ mbar O_2 + 2% O_3, cooling pressure 10^{-3} mbar O_2. The film contains the infinite-layer (IL), the superstructure (M), and the $Sr_{14}Cu_{24}O_{41}$ (14:24) phases. With 3 is marked the $Sr_{2-x}La_xCuO_{3\pm\delta}$ phases, with * an amorphous region, while 1 and 2 mark unknown phases.*

[xxv] The formation of $Sr_{14}Cu_{24}O_4$ and $Sr_{2-x}La_xCuO_{3\pm\delta}$ phases was related not only with the quality of the substrate-film interface, but also with wrong settings for laser energy (i.e., a too low laser energy), which resulted in non-stoichiometric deposition.

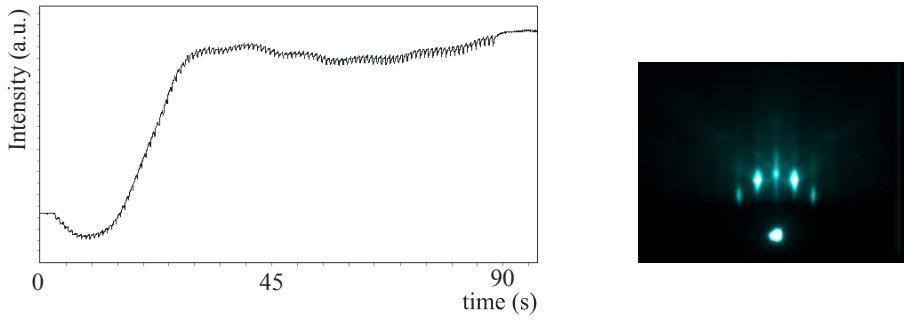

(a) *(b)*

Fig. 6.19 *(a) Evolution of the intensity of the specular spot during deposition of a ~ 4 nm $BaTiO_3$ layer on $KTaO_3$ (T_s = 800 °C, P_d = 0.10 mbar O_2), and (b) the resulted RHEED pattern after the $BaTiO_3$ layer was annealed 0.25 h at 900 °C, 2×10^{-6} mbar.*

XRD data showed that these reduced films were not single phase, the long c-axis phase being also present in the structure.

It can be concluded that the in-plane tensile strain of SLCO films on $KTaO_3$ favours electron doping of the CuO_2 planes. However, the films have a rough surface morphology and are, often, not single phase. In order to improve the substrate-film interface, $BaTiO_3$ was used as buffer layer for $KTaO_3$ substrates. The results on structural and electrical properties of the SLCO films are presented in next section.

6.2.5 $Sr_{1-x}La_xCuO_2$ on $BaTiO_3$-buffered $KTaO_3$

6.2.5.1 Structural properties

In order to improve the surface morphology of the $KTaO_3$ substrates a $BaTiO_3$ buffer layer was used. The RHEED data showed that the intensity of the specular beam after film's deposition is higher than the starting value (see Fig. 6.19a), suggesting that the surface smoothness has been improved by heteroepitaxial growth of $BaTiO_3$. The $BaTiO_3$ layer shows a clear 2D RHEED pattern with Kikuchi lines (Fig. 6.19b). This demonstrates an improvement of the substrate surface morphology after deposition of the $BaTiO_3$ buffer layer.

When $Sr_{1-x}La_xCuO_2$ films where grown using a mixture of O_2/O_3, the RHEED pattern showed the formation of a spotty pattern with diffraction spots characteristic of a triple unit cell in the c-axis. The XRD data showed that this phase is $Sr_{14}Cu_{24}O_{41}$. Its formation could be avoided by using for ablation targets with excess of Sr (e.g., $SrLa_{0.15}CuO_{2+\delta}$) and by increasing the target-substrate distance (from 45 mm to 50 mm). In this new configuration, the $Sr_{1-x}La_xCuO_2$ films could be grown in O_2 or O_2/O_3 without the formation of secondary phases (if an optimum cooling down procedure is followed). The films showed a smooth surface morphology, with typical values for peak-to-valley distances of few unit cells.

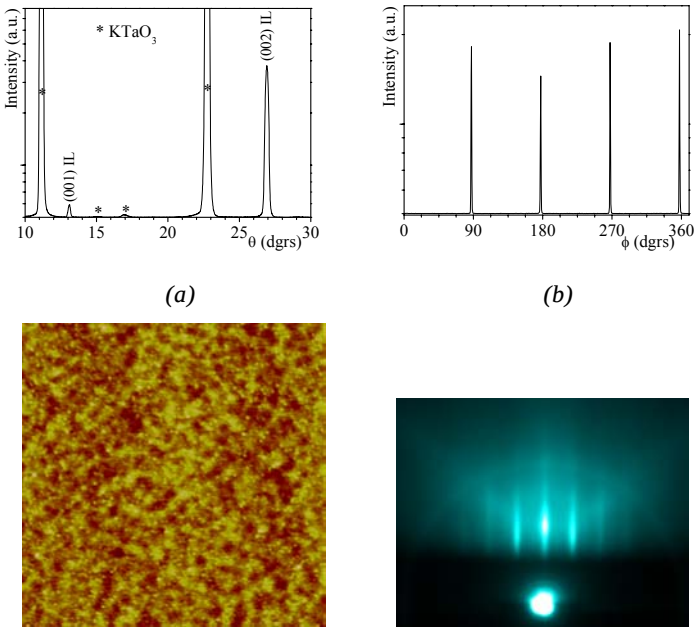

(a) *(b)*

(c) *(d)*

Fig. 6.20 *Properties of a $Sr_{0.85+\delta}La_{0.15}CuO_2$ film deposited at 550 °C and 10^{-3} mbar O_2 on $BaTiO_3$ buffered $KTaO_3$. The film was cooled down under 10^{-3} mbar O_2 and places in loadlock at 425 °C. (a) θ-2θ XRD scan, (b) ϕ scan around {202} reflection of SLCO, (c) topographic AFM, and (d) RHEED pattern of the film.*

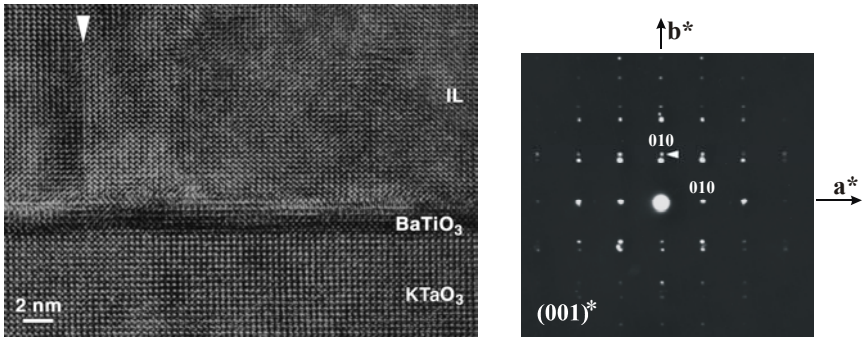

(a) *(b)*

Fig. 6.21 *HREM (a) and ED (b) of a $Sr_{0.85}La_{0.15}CuO_2$ film grown on $BaTiO_3$ buffered $KTaO_3$ (P_d = 10^{-3} mbar O_2, T_S = 550 °C, oxygen pressure during cooling of 10^{-3} mbar)*

In Fig. 6.20a-d the structural and morphological properties of an optimally deposited $Sr_{0.85+\delta}La_{0.15}CuO_2$ film are depicted. The film was deposited at 550 °C and 10^{-3} mbar O_2. After deposition the films was cooled down to 425 °C inside the deposition

chamber under 10^{-3} mbar O_2 than placed in the loadlock. The XRD data showed a single-phase IL film (Fig. 6.20a), with c-axis oriented perpendicular to the substrate surface (Fig. 6.20b, ϕ scan around {202} reflection of the film). The topographic AFM image (Fig. 6.20c) and the RHEED pattern from Fig. 6.20d indicate a film with smooth surface morphology. The cross section HREM (Fig. 6.21a) and the (001)* electron diffraction (Fig. 6.21b) analyses of this film confirmed that the film is single phase with a tetragonal IL structure.

The phase composition of SLCO films showed a strong dependence not only on deposition conditions, but also on cooling procedure. The oxygen partial pressure and the temperature at which the samples were placed in loadlock for cooling are the main parameters that have to be controlled in order to yield single-phase IL-SLCO films. In Fig. 6.23 is shown the θ-2θ scans of three SLCO (x = 0.15) films grown under the same conditions, but cooled down in different oxygen pressure. The long c-axis phase is predominant when cooling at pressures lower than 10^{-4} mbar O_2 (see Fig. 6.22a), its composition decreasing with increasing O_2 pressure (up to 10^{-3} mbar, see Fig. 6.22b and c). It can be concluded that the IL phase forms during cooling from the superstructure phase by filling the oxygen vacancies from the CuO_x planes. The drawback of this

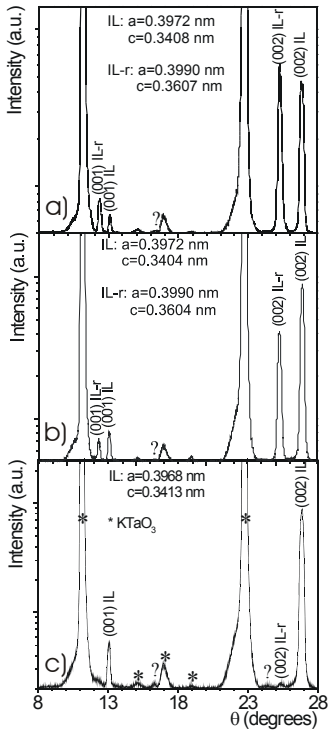

Fig. 6.22 *XRD θ-2θ scans of $Sr_{0.85}La_{0.15}CuO_2$ films deposited on ~ 2 nm $BaTiO_3$ on (001) $KTaO_3$ and cooled down under different pressure: (a) 10^{-4} mbar O_2, (b) 5×10^{-4} mbar O_2, and (c) 10^{-3} mbar O_2. Deposition conditions for $Sr_{0.85}La_{0.15}CuO_2$ films: $P_d = 10^{-3}$ mbar O_2, $T_s = 550$ °C, $E_d = 2.35$ J/cm², $E_m = 35$ mJ. The films were placed in loadlock at 500 °C.*

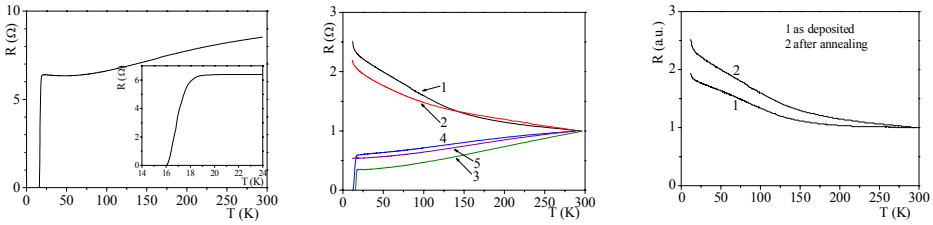

a) *b)* *c)*

Fig. 6.23 *(a) Temperature dependence of resistance for $Sr_{0.85}La_{0.15}CuO_2$ thin film grown on $KTaO_3$ (T_s = 550 °C, P_d =10^{-3} mbar O_2). The film was annealed for 10 min at 550 °C and 3×10^{-4} mbar O_2. (b) Normalized resistance for $Sr_{1-x}La_xCuO_2$ thin films (T_s = 550 °C, P_d = 10^{-3} Pa O_2), with different La contents, grown on $BaTiO_3/KTaO_3$: (1) x = 0.10, (2) x = 0.125, (3) x = 0.15, (4) x = 0.175, and (5) x = 0.20. (c) Normalized resistance for a $Sr_{0.9}La_{0.1}CuO_2$ thin film grown on $BaTiO_3/KTaO_3$ (T_s = 550 °C, P_d = 10^{-3} mbar O_2): (1) the as-deposited film, and (2) same film after annealing for 0.5 h at 300 °C and 10^{-6} mbar.*

cooling procedure is the difficulty in controlling the actual oxygen content (in CuO_x planes and Sr-planes, as well), with negative influence on the superconductive properties of the films (see next).

6.2.5.2 Electrical properties

Fig. 6.23a shows the temperature dependence of resistance for SLCO thin films with different La content, grown on $BaTiO_3/KTaO_3$. The $0.10 \le x < 0.15$ films showed semiconducting behaviour, while $x = 0.20$ films were metallic. Superconductivity was observed for $0.15 \le x \le 0.175$ films, with the highest T_c values for $x = 0.15$ films. These latter films showed the highest T_c values, with $T_{c,zero}$ = 16K and $T_{c,onset}$ = 21 K.

As was discussed in Chapter 2, vacuum annealing is used in order to induce superconductivity in the electron-doped $Sr_{1-x}Ln_xCuO_2$ thin films. Therefore, annealing experiments in vacuum, at temperatures in range of 300-550 °C, were performed in order to determine the evolution of the electrical properties. In all cases, independent of the annealing pressure and temperature, an increase of the electrical resistivity was observed. This is exemplified in Fig. 6.23b for an $Sr_{0.9}La_{0.1}CuO_2$ film annealed for 0.5 h at 300 °C at 10^{-6} mbar. After annealing, the film showed an increased value of the resistance.

6.3 Conclusions

$Sr_{1-x}La_xCuO_{2\pm\delta}$ (x = 0.1-0.2) thin films were epitaxially grown on (001)-oriented $SrTiO_3$ and $KTaO_3$ substrates (with and without a $BaTiO_3$ buffer layer) by means of PLD with in situ monitoring using high-pressure RHEED. X-ray diffraction in the normal Bragg-reflection geometry, HREM and ED were used for structural characterization of the films. The results show that high-quality epitaxial $Sr_{1-x}La_xCuO_{2\pm\delta}$ ($0.1 \le x \le 0.2$) thin films can be fabricated by PLD on $SrTiO_3$ and $KTaO_3$

templates. $BaTiO_3$ was used as buffer layer with the aim of: i) reducing the epitaxial compressive strain in films grown on $SrTiO_3$, and ii) improving the surface morphology of the $KTaO_3$ substrates. The deposition parameters for the films were optimized for the La concentration in the doping range (x = 0.1-0.2) used for this study. The films grown on vacuum annealed $BaTiO_3$ buffered $SrTiO_3$ or on $KTaO_3$ under optimum deposition parameters (deposition pressure and temperature, as well as cooling pressure) showed sharp superconductive transition in electrical resistance measurements.

Formation of the SLCO phases, with infinite layer structure, was found to be dependent on the deposition conditions (deposition pressure and ambient gas) and cooling procedure. For deposition pressures in range of 10^{-2}-0.40 mbar O_2/N_2 a secondary phase (an $2\sqrt{2}a_p \times 2\sqrt{2}a_p \times c_p$ superstructure with mixed copper valence and ordered oxygen vacancies in the CuO_x plane) is formed. Its concentration increases with La concentration, x, and N_2 partial pressure. Another secondary phase was observed for deposition pressure of about 0.5-10^{-2} mbar O_2 with cell parameters bigger than that of the infinite layer phase and semiconducting behaviour. Its formation and concentration are highly dependent on the cooling procedure and deposition pressure and it can coexist with the infinite layer phase for $x \geq 0.1$. Single-phase films containing this compound could be obtained by quenching the as-deposited films by covering it with an $SrTiO_3$ cap layer. In the films with the infinite-layer phase, T_c became higher with the decrease of cooling pressure; the highest values were observed for films with 15% La doping. This result is different from the bulk SLCO where the La content does not significantly affect T_c[xxvii]. The highest superconducting transition of 21 K (onset) was observed in $Sr_{0.85}La_{0.15}CuO_2$ film. The observed T_c for $Sr_{1-x}La_xCuO_2$ thin films was lower than that in the high-pressure-synthesized ceramic samples. This difference may be due to the difficulty of completely removing the excess oxygen from the Sr planes. Phase segregation into infinite-layer related phase might be another reason for low T_c observed in thin films.

Cooling procedure was found to be one of the critical factors for yielding n-type superconductivity in $Sr_{1-x}La_xCuO_2$ films. Annealing in an oxygen atmosphere degraded or suppressed superconductivity, as well as cooling and annealing in vacuum. An increase of T_c was observed for decreasing cooling oxygen pressure, down to certain values (about 10^{-5} mbar), an indication of electron-doped type in $Sr_{1-x}La_xCuO_2$. Annealing in vacuum resulted in a slightly orthorhombic distortion, most probably due to partial removal of oxygen from CuO_x planes at the annealing temperatures (400-550 ^oC). The time scale for cooling procedure was also found to be crucial for presence of superconductivity.

The synthesis of infinite layer $Sr_{1-x}La_xCuO_{2\pm\delta}$ (x = 0.1-0.2) thin films demonstrates the capacity of the laser ablation method in stabilizing these metastable phases. New ordered structures may be stabilized in the Sr-La-Cu-O system by varying the Sr/La ratio and deposition conditions.

[xxvii] This T_c dependence on Ln doping level was observed in all $Sr_{1-x}Ln_xCuO_2$ thin films (see, e.g., Ref. 5)

References

1 Y. Tokura, H. Tagaki and S. Uchida, *Nature* **337**, 345 (1989)
2 C. Huang, E. Moran, A.I. Nazzal and J.B. Torrance, *Physica C* **158**, 148 (1989)
3 J.T. Market, E.A. Early, T. Bjørnholm, S. Ghamaty, B.W. Lee, J.J. Neumeier, R.D. Price, C.L. Seaman and M.B. Maple, *Physica C* **158**, 178 (1989)
4 T. Siegrist, S.M. Zahurac, D.W. Murphy and R.S. Roth, *Nature* **334**, 231 (1988)
5 S. Karimoto, K. Ueda, M. Naito and T. Imai, *Appl. Phys. Lett.* **79**, 2767 (2001)
6 S.J. Pennycook, M.F. Chisholm, D.E. Jesson, R. Feenstra, S. Zhu, X.Y. Zheng and D.J. Lowndes, *Physica C* **202**, 1 (1992)
7 J. Choi, C.B. Eom, G. Rijnders, H. Rogalla and D.H.A. Blank, *Appl. Phys. Lett.* **79**, 1447 (2001)
8 N. Sugii, K. Matsuura, K. Kubo, K. Yamamoto, M. Ichikawa and H. Yamauchi, *J. Appl. Phys.* **74**, 4047 (1993)
9 C. Niu and C.M. Lieber, *Appl. Phys. Lett.* **61**, 1712 (1992)
10 E.C. Jones, D.P. Norton, D.K. Christen and D.H. Lowndes, *Phys. Rev. Lett.* **73**, 166 (1994)
11 N. Sugii, H. Yamauchi and M. Izumi, *Phys. Rev. B* **50**, 9503 (1994)
12 V. Leca, G. Rijnders, D.H.A. Blank, H. Rogalla, S. Bals, and G. van Tendeloo, E-MRS Conference, Strasbourg, France (2002);
13 S. Bals, G. Van Tendeloo, G. Rijnders, M. Huijben, V. Leca and D.H.A. Blank, to be published in *IEEE Trans. Appl. Supercond.* (2003)
14 K. Terai, M. Lippmaa, P. Ahmet, T. Chikyow, T. Fujii, H. Koinuma and M. Kawasaki, *Appl. Phys. Lett.* **80**, 4437 (2002)
15 A. Gupta, B. Mercey, H. Hervieu and B. Raveau, *Chem. Mater.* **6**, 1011 (1994)
16 A. Gupta, B.W. Hussey, T.M. Shaw, A.M. Guloy, M.Y. Chern, R.F. Saraf and B.A. Scott, *J. Solid. State Chem.* **112**, 113 (1994)
17 M. Fujimoto, *J. Crystal Growth* **237 - 239**, 430 (2002)
18 Azco Industries Limited, Canada (http://www.azcozon.com)
19 T. Frey, C.C. Chi, C.C. Tsuei, T. Shaw and F. Bozso, *Phys. Rev. B* **49**, 3483 (1994)
20 S.Tao, H.-U. Nissen, C. Beeli, M. Cantoni, M.G. Smith, J. Zhou and J.B. Goodenough, *Physica C* **204**, 117 (1992)
21 X.–Y. Zheng, D.H. Lowndes, S. Zhu, J.D. Budai and R.J. Warmack, *Phys. Rev. B* **45**, 7584 (1992)
22 A.J.H.M. Rijnders, *The initial growth of complex oxides: study and manipulation*, PhD thesis ISBN 9036516579, University of Twente, The Netherlands (2001)
23 N. Sugii, M. Ichikawa, K. Kubo, T. Sakurai, K. Yamamoto and H. Yamauchi, *Physica C* **196**, 129 (1992)
24 H. Adachi, T. Satoh, Y. Ichikawa, K. Setsune and K. Wasa, *Physica C* **196**, 14 (1992)
25 B. Mercey, A. Gupta, M. Hervieu and B. Raveau, *J. Solid State Chem.* **116**, 300 (1995)
26 J.T. Markert, T.C. Messina, B. Dam, J. Huibregste, J.H. Rector and R. Griessen, *Proc. SPIE* **4058**, 141 (2000)
27 T. Siegrist, L.F. Schneemeyer, S.A. Sunshine, J.V. Waszczak and R.S. Roth, *Mat. Res. Bull.* **23**, 1429 (1988)

28 E.M. McCarron, M.A. Subramanian, J.C. Calabrese and R.L. Harlow, *Mater. Res. Bull.* **23**, 1355 (1988)

Summary

In this thesis, a systematic study of thin film preparation of p- and n-type infinite layer (IL) compounds and artificially layered structures, as well as their properties (e.g., structural and electrical) are presented. Pulsed laser deposition (PLD) was effectively used for the epitaxial growth of these oxides. Different substrates (e.g., $NdGaO_3$, $SrTiO_3$ or $KTaO_3$) were used to epitaxially stabilize these metastable structures. The role of the compressive or tensile strain in stabilization of p- or n-type IL phase is also discussed. The IL compounds are ideal candidates for studies of the formation of artificially layered structures. Pulsed laser interval deposition (PLiD) growth and properties of such artificially layered structures on $NdGaO_3$ substrates, constructed by sequentially ablating IL targets, is also presented and discussed. A critical parameter in the film growth process is the substrate-film interface, determining the morphology and structural properties of the film. To improve the substrate surface morphology different chemical or thermal treatment are developed for $NdGaO_3$, $SrTiO_3$, LSAT, $SrLaAlO_4$, and $KTaO_3$ substrates and described here.

The infinite layer (IL) compounds $ACuO_2$ (A is an alkaline earth metal) have the simplest structure among the HTSc materials. It consists of corner-shared CuO_2 layers and A-metal(s) planes, alternately stacked along the c-axis. With the exception of $Ca_{0.85}Sr_{0.15}CuO_2$, the IL compounds are metastable phases that require high-pressure (2-6 GPa) and high-temperature ($\leq 1400\ ^oC$) conditions for their synthesis. Superconductivity can be induced in these compounds by electron or hole doping. Hole doping (p-type) can be obtained by introduction of excess oxygen in the A-plane, creating alkaline earth deficient defect layers in the structure, or by monovalent ion (e.g., Na^+, Li^+) substitution. Electron doping (n-type) of IL phases is obtained by partial substitution of alkaline earth atoms with lanthanide Ln^{3+} (Ln = La, Pr, Nd, Sm, Gd) atoms. Since the need of very high external pressures impedes technological applications, simulating such effects by the use of internal strain in thin films offers an alternative way. The stability effect of the substrate can be used to grow metastable phases with structural characteristics similar with that of the bulk samples, but with no impurity phases. Using substrates with different in plane cell parameters (e.g., $SrTiO_3$ and $KTaO_3$) the misfit between the substrate and film is used here to induce the desired p- or n-type doping.

The high deposition rates attained in PLD during the deposition pulse and the variable range of the kinetic energy of the deposited particles is exploited to improve the

film properties (e.g., crystallinity and surface smoothness). Taking advantage of the growth kinetics at the high supersaturation reached during the deposition pulses, a new approach is used, called pulsed laser interval deposition (PLiD). This method enables 2-dimensional (2-D) growth and, therefore, a smooth film surface. It is used in imposing a layer-by-layer growth of $ACuO_2$ phases and artificially layered structures (build by sequential deposition of different IL blocks).

Control of the oxygen content is one of the requirements for tuning the valence of copper that can result in superconductivity in the IL materials. The oxygen pressure used during deposition of the IL films results in structural modifications that have substantial influence on the electrical transport properties. The oxidation power during growth should be sufficiently high to enable growth of stable phases. This is achieved using relatively high oxygen pressures (i.e., 10^{-3}-0.4 mbar). High-pressure RHEED is used for growth control and monitoring.

Besides the control of the deposition conditions, the fabrication of artificially structured films using layer-by-layer growth requires optimal surface smoothness of the substrate. The chemistry and morphology of the terminating atomic layer(s) influences the interface properties and, consequently, the structural and physical properties of the film. Therefore, a substrate with good lattice matching and an atomically smooth surface with a known composition are essential. In order to control the chemistry and morphology of the surface terminating layer(s), different chemical and thermal treatment methods were developed for (001) and (110) $NdGaO_3$, (001) $SrTiO_3$, (001) LSAT, (001) $SrLaAlO_4$ and (001) $KTaO_3$ single-crystal substrates. They were selected for their chemical and structural compatibility with the phases under investigation in this thesis. For $KTaO_3$ substrates, a $BaTiO_3$ buffer-layer is also used in order to improve the surface crystallinity. These substrates have a perovskite or related structure, consisting of alternating layers of $AO_{1+\delta}$ (A = Sr, La or Nd) and $BO_{2-\delta}$ (B = Ti, Al, Ta or Ga) in the c direction. By considering their layered structure and reactivity with mineral acids, selective removal of one of the surface oxides was achieved by a thermal treatment or though chemical etching, followed by annealing. The resulting surface morphology was studied by AFM and high-pressure RHEED. A-site single terminated surface is obtained after annealing at optimum conditions (i.e., annealing temperature, time, and ambient gas). Chemical etching in solutions with different reactivity (i.e., NH_4F + HF + H_2O, NH_4Cl + HCl, HCl + HNO_3, and HCl), followed by thermal treatment is used to obtain a B-site single terminated surface, free of etch pits. There is a strong dependence of the final surface morphology on the properties of the substrate (e.g., surface chemistry, vicinal angle and its orientation), on the characteristics of the etching solution, and on the annealing conditions.

One possible solution for modifying the carrier density concentration is to apply a different level of strain on the CuO_2 planes. $NdGaO_3$ single-crystal substrate is used as template layer in order to study the role of the compressive strain and of the deposition conditions on the structural and electrical properties of these structures. Pulsed laser deposition was used to grow single-phase thin films of $ACuO_2$ phases and artificially layered structures of these copper oxides. Using (001) or (110) $NdGaO_3$ as atomic template these metastable phases can be stabilized in their tetragonal symmetry. It is shown that by growth manipulation all $ACuO_2$ phases can be grown with different

critical thickness on bare $NdGaO_3$ substrates without using a buffer layer. The use of single-terminated $NdGaO_3$ substrates plays a crucial role in yielding films with smooth surface morphology. The films are epitaxial, with complete in-plane crystalline alignment with the substrate. The artificially layered superlattices showed a dependence of their structural and electrical properties on the growth conditions (deposition pressure and temperature, as well as on the deposition rate for each infinite layer constituent block).

Growth manipulation by means of pulsed laser interval deposition relies on the correct determination of the deposition rate, which can be accurately determined by means of in situ high-pressure RHEED, as well as the properties of the interface between the constituent blocks. These aspects determined the final structure, defects network, and the morphology of the films and, therefore the final transport properties. The use of $NdGaO_3$ helps stabilizing the right tetragonal $ACuO_2$ phases and their superlattices by the induced compressive strain. The desired superconducting properties of these structures require deposition conditions that can assure incorporation of enough excess oxygen to reach the charge carrier density needed to dope the CuO_2 planes from the IL blocks.

$Sr_{1-x}La_xCuO_{2\pm\delta}$ (x = 0.1-0.2) thin films are epitaxially grown on (001) $SrTiO_3$ and $KTaO_3$ substrates (with and without a $BaTiO_3$ buffer layer) by means of PLD with *in situ* monitoring using high-pressure RHEED. $BaTiO_3$ is used as buffer layer with the aim of i) reducing the epitaxial compressive strain in films grown on $SrTiO_3$ and ii) to improve the surface morphology of the $KTaO_3$ substrates. The deposition parameters for the films were optimised for the La concentration. For the compressively strained n-type IL films, T_c is reduced due to difficulty in removing the excess oxygen from the Sr(Ln) planes. Improved T_c values can be obtained by inducing tensile strain in the CuO_2 planes. Here, the role of the substrate-film misfit on the structural and electrical properties of $Sr_{1-x}La_xCuO_2$ films is studied for $SrTiO_3$ and $KTaO_3$ cases.

Cooling procedure was found to be one of the critical factors for yielding superconductivity. Annealing in an oxygen atmosphere degraded or suppressed superconductivity, as well as cooling and annealing in vacuum. An increase of T_c was observed for decreasing oxygen partial pressure during cooling, down to certain values (about 10^{-5} mbar), an indication of n-type doping in $Sr_{1-x}La_xCuO_2$. Annealing in vacuum resulted in a slightly orthorhombic distortion, most probably due to partial removal of oxygen from CuO_x planes at the annealing temperatures (400-550°C). The time scale for cooling procedure was also found to be crucial for presence of superconductivity.

In this thesis, PLD (or PLiD) is used for epitaxial growth of p- and n-type infinite layer thin films and of artificially layered structures. The combination of PLD (or PLiD) with *in situ* monitoring of the growth front with high-pressure RHEED enabled accurate control of the growth. Chemical and thermal treatments were developed and used in order to improve the surface morphology of the substrate materials used for the epitaxial growth of these structures.

Samenvatting (Summary in Dutch)

Dit proefschrift bevat een systematische studie over de preparatie en eigenschappen (structureel en elektrisch) van dunne lagen van p- en n-type "infinite layer" (IL) verbindingen en kunstmatige gelaagde structuren. Deze oxides zijn succesvol epitaxiaal gegroeid met behulp van pulsed laser depositie (PLD). Verschillende substraten (zoals $NdGaO_3$, $SrTiO_3$ en $KTaO_3$) zijn toegepast om deze metastabiele structuren te stabiliseren. Ook de rol van kompressieve en tensiele spanning voor het stabiliseren van p- of n-type IL fases is onderzocht. De IL complexen zijn ideale kandidaten voor het bestuderen van de vorming van kunstmatig gelaagde structuren. Deze structuren, opgebouwd door de ablatie van IL targets, zijn gerealiseerd door gebruik te maken van pulsed laser interval depositie (PLiD). Een kritische parameter tijdens de groei van een dunne laag is het grensvlak dat die zich vormt tussen het substraat en de aangroeiende dunne laag. Dit grensvlak bepaalt de morfologie en structuur van de laag. Voor het verbeteren van de dunne laag morfologie zijn in dit proefschrift verschillende chemische en thermische behandelingen ontwikkeld voor $NdGaO_3$, $SrTiO_3$, LSAT, $SrLaAlO_4$, en $KTaO_3$ substraten.

De $ACuO_2$ IL complexen (met "A" een zeldzaam aardmetaal) hebben de eenvoudigste structuur onder de hoog-temperatuur supergeleidende (HTSc) materialen, bestaande uit CuO_2 lagen en A-metaal vlakken met gemeenschappelijke hoekpunten die om-en-om gestapeld zijn langs de c-as. Met uitzondering van $Ca_{0.85}Sr_{0.15}CuO_2$ hebben de IL verbindingen een metastabiele fase die een hoge druk (2-6 GPa) en hoge temperatuur ($\leq 1400\ ^oC$) nodig hebben om zich te kunnen vormen. Deze complexen verkrijgen supergeleidende eigenschappen door middel van het doteren met elektronen of gaten. Het doteren met gaten (p-type) wordt verkregen door het introduceren van een overmaat aan zuurstof in het A-vlak, wat een alkalisch verarmde laag in de structuur veroorzaakt, of door een substitutie van monovalente ionen (zoals Na^+ en Li^+). Het doteren met elektronen (n-type) is mogelijk door het gedeeltelijk vervangen van de aard-alkali atomen door lanthanide Ln^{3+} (Ln = La, Pr, Nd, Sm, Gd) atomen. Aangezien de benodigde extreem hoge externe druk een technologische belemmering vormt, is het gebruik van interne spanning een alternatieve manier om de gezochte effecten te realiseren. De stabiliserende invloed van het substraat kan worden gebruikt om metastabiele lagen te groeien met structurele eigenschappen gelijk aan het bulkmateriaal, maar dan zonder secundaire fasen. Door gebruik te maken van substraten met verschillende roosterparameters (zoals $SrTiO_3$ en $KTaO_3$) wordt de gewenste p- of n-type dotering geïntroduceerd.

De hoge depositiesnelheid tijdens een PLD depositiepuls en de instelbaarheid van de kinetische energie van de deponerende deeltjes worden in dit proefschrift uitgebuit om de laageigenschappen, zoals kristalliniteit en gladheid van het oppervlak, te optimaliseren. Door voordeel te halen uit de groeikinetiek tijdens de hoge oververzadiging, dat bereikt wordt gedurende de depositiepuls, is er een nieuwe aanpak voor PLD ontwikkeld die PLiD wordt genoemd. Deze methode maakt 2-dimensionale (2-D) groei mogelijk met als resultaat een glad oppervlak en is gebruikt om laag-voor-laag groei van $ACuO_2$ te forceren. Door middel van het afwisselend deponeren van verschillende IL lagen (of blokken) zijn kunstmatige gelaagde structuren gerealiseerd.

Het controleren van de zuurstofconcentratie is één van de vereisten voor het afstemmen van de valentie van de ingebouwde koperatomen hetgeen kan resulteren in supergeleiding in IL materialen. De zuurstof achtergronddruk gedurende de depositie resulteert in structurele modificaties die van wezenlijke invloed zijn op het elektrische transport. Het oxidatievermogen gedurende het groeien moet voldoende hoog zijn om de groei van stabiele fasen mogelijk te maken. Dit wordt bereikt bij relatief hoge zuurstofdruk (tussen 10^{-3} en 0.40 mbar). Voor het *in situ* controleren van het groeiproces en het realiseren van kunstmatige gelaagde structuren bij deze zuurstofdrukken is gebruik gemaakt van hoge druk reflectie hoge energie elektronen diffractie (RHEED).

Naast het controleren van de depositiecondities, is het voor het maken van laag-voor-laag gegroeide kunstmatige structuren nodig om een zeer vlak substraat te hebben. De chemie en morfologie van het substraatoppervlak beïnvloeden de grensvlakeigenschappen tussen substraat en dunne laag en daarmee de structuur en fysische eigenschappen van de laag. Een substraat met een goed aangepast kristalrooster en een vlakheid op atoomniveau is daarom noodzakelijk. Voor het controleren van de chemie en morfologie van de oppervlaktelaag zijn verschillende chemische en thermische methoden ontwikkeld voor (001) en (110) $NdGaO_3$, (001) $SrTiO_3$, (001) LSAT, (001) $SrLaAlO_4$ and (001) $KTaO_3$ éénkristallijne substraten. Deze substraten zijn geselecteerd vanwege hun chemische en structurele compatibiliteit met de onderzochte IL fasen. Voor de $KTaO_3$ substraten is een $BaTiO_3$ bufferlaag gebruikt om de crystalliniteit aan het oppervlak te verbeteren. Deze substraten hebben een perovskiet of gerelateerde structuur, bestaande uit alternerende lagen van $AO_{1+\delta}$ (A = Sr, La of Nd) en $BO_{2-\delta}$ (B = Ti, Al, Ta of Ga). Door gebruik te maken van selectief etsen is het mogelijk om één van de oxides aan het oppervlak te verwijderen. Door een thermische behandeling wordt vervolgens een atomair vlak en kristallijn oppervlak verkregen. Een enkelvoudig $AO_{1+\delta}$-oppervlak wordt verkregen na enkel een thermische behandeling. Om een enkelvoudig $BO_{2-\delta}$-oppervlak te verkrijgen is chemisch etsen noodzakelijk. Hiervoor zijn oplossingen met verschillende reactiviteit toegepast (zoals NH_4F + HF + H_2O, NH_4Cl + HCl, HCl + HNO_3, en HCl). De resulterende oppervlaktemorfologie is bestudeerd met behulp van atomaire krachtmicroscopie (AFM) en RHEED. De uiteindelijke morfologie is sterk afhankelijk van de eigenschappen van het substraat (zoals oppervlak chemie, de vicinale hoek en zijn oriëntatie), van de karakteristieken van het etsmiddel, en van de anneal condities.

Een mogelijke oplossing voor het modificeren van de ladingsdragerconcentratie is het toepassen van een verschillend niveau in spanning in de CuO_2 vlakken. $NdGaO_3$ mono-crystallijne substraten zijn gebruikt voor het bestuderen van de rol van

kompressieve spanning en depositie condities op de structurele en elektrische eigenschappen van de lagen. Door gebruik te maken van (001) of (110) $NdGaO_3$ zijn $ACuO_2$ metastabiele fases gestabiliseerd in hun tetragonale symmetrie. Er is gedemonstreerd dat door groeimanipulatie $ACuO_2$ fases kunnen worden gegroeid met verschillende kritische diktes op $NdGaO_3$ substraten zonder gebruik te moeten maken van een bufferlaag. De dunne lagen zijn epitaxiaal met complete kristallijne uitrichting met het substraatrooster. De kunstmatig gelaagde structuren laten een afhankelijkheid van hun structurele en elektrische eigenschappen zien met de groeicondities (depositie druk en temperatuur, en de depositiesnelheid van elk IL blok).

Groeimanipulatie door middel van PLiD is afhankelijk van de exacte controle van de depositie, wat mogelijk is met *in situ* hoge-druk RHEED, en de eigenschappen van de grensvlakken tussen de verschillende IL blokken. Deze aspecten bepalen de uiteindelijke structuur, ingebouwde defecten en de morfologie van de dunne laag, en daarmee de uiteindelijke transporteigenschappen. De opgelegde kompressieve spanning bij gebruik van $NdGaO_3$ maakt het stabiliseren van de correcte tetragonale $ACuO_2$ fases en hun kunstmatige structuren mogelijk. Echter, de gewenste supergeleidende eigenschappen eisen depositiecondities die voldoende zuurstofinbouw mogelijk maken om de ladingsdrager dichtheid te vergroten. Dit kan gerealiseerd worden door de CuO_2 vlakken van de IL blokken te doteren.

In dit proefschrift wordt de rol van de epitaxiale spanning op de structurele en elektrische eigenschappen van $Sr_{1-x}La_xCuO_2$ lagen bestudeerd. $Sr_{1-x}La_xCuO_{2\pm\delta}$ (x = 0.1-0.2) dunne lagen zijn epitaxiaal gegroeid op (001) $SrTiO_3$ en $KTaO_3$ substraten (met en zonder een $BaTiO_3$ bufferlaag). $BaTiO_3$ is gebruikt als bufferlaag voor het reduceren van de epitaxiale kompressieve spanning in dunne lagen gegroeid op $SrTiO_3$, en het verbeteren van de oppervlakte morfologie van de $KTaO_3$ substraten. De depositie parameters van de lagen zijn geoptimaliseerd afhankelijk van de La concentratie. In de n-type IL dunne lagen onder compressieve spanning is de T_c verlaagd omdat de overmaat aan zuurstof moeilijk te verwijderen is uit de Sr(Ln) vlakken. Dit kan worden verbeterd door een tensiele spanning in de CuO_2 vlakken te introduceren. De afkoelprocedure is een belangrijke factor voor het verkrijgen van supergeleiding. Het annealen in een zuurstof omgeving alsook het afkoelen en annealen in een vacuum omgeving onderdrukt supergeleiding. De afkoeltijd bleek van cruciaal belang voor de aanwezigheid van supergeleiding. Een toename van T_c is waargenomen tijdens het koelen bij afnemende zuurstof achtergronddruk tot ongeveer 10^{-5} mbar. Dit is een indicatie voor n-type dotering in $Sr_{1-x}La_xCuO_2$. Het annealen in een vacuüm resulteerde in een lichtelijke orthorhombische vervorming, waarschijnlijk veroorzaakt door het een gedeeltelijke verwijdering van zuurstof uit het CuO_x vlak bij de hoge anneal temperatuur (400-550°C).

Dit proefschrift beschrijft de epitaxiale groei van p- en n-type IL dunne lagen en kunstmatig gelaagde structuren met behulp van PLD. De combinatie van PLD (of PLiD) met *in situ* monitoring van het groeifront (gebruik makende van hoge-druk RHEED) maakt het mogelijk om deze groei accuraat te controleren. Chemische en thermische behandelmethoden zijn ontwikkeld om de oppervlaktemorfologie van de substraat-materialen te verbeteren. Hierdoor is het mogelijk om epitaxiale spanning toe te passen in de dunne lagen en daarmee hun eigenschappen te manipuleren.

List of publications

"Transmission electron microscopy on interface engineered superconducting thin films" S. Bals, G. van Tendeloo, G. Rijnders, M. Huijben, **V. Leca** and D.H.A. Blank, *IEEE Trans. Appl. Supercond.* **13**, 2834 (2003)

"Structural and optical characterisation of porous anodic aluminum oxide" A.C. Galca, E.S. Kooij, H. Wormeester, C. Salm, **V. Leca**, J.H. Rector and B. Poelsema, *J. Appl. Phys.* **94**, 4296 (2003)

"New low-stress PECVD poly-SiGe layers for MEMS" C. Rusu, S. Sedky, B. Parmentier, A. Verbist, O. Richard, B. Brijs, L. Geenen, A. Witvrouw, F. Lärmer, F. Fischer, S. Kronmüller, **V. Leca**, B. Otter, approved for publication in *J. Microelectromech. Syst.* (2003)

"Optimization of superconducting thin films by TEM" S. Bals, G. van Tendeloo, G. Rijnders, D.H.A. Blank, **V. Leca** and M. Salluzzo, *Physica C* **372-376**, 711 (2002)

"Superconducting thin films of MgB_2 on Si by pulsed laser deposition" A. Brinkman, D. Mijatovic, G. Rijnders, **V. Leca**, H.J.H. Smilde, I. Oomen, A.A. Golubov, F. Roesthuis, S. Harkema, H. Hilgenkamp, D.H.A. Blank and H. Rogalla, *Physica C* **353**, 1 (2001)

"Imposed layer-by-layer growth with pulsed laser interval deposition" G. Rijnders, G. Koster, **V. Leca**, D.H.A. Blank and H. Rogalla, *Appl. Surf. Sci.* **168**, 223 (2000)

"Wet etching methods for perovskite substrates" **V. Leca**, G. Rijnders, G. Koster, D.H.A. Blank and H. Rogalla, *MRS Symp.* **587**, O3.6.1 (2000)

"$GaO_{2-\delta}$ single terminated (001) and (110) oriented $NdGaO_3$ substrates for thin film growth" **V. Leca**, G. Rijnders, D.H.A. Blank and H. Rogalla (preprint, 2003)

"New approach to induce superconductivity in PLD grown $Sr_{1-x}La_xCuO_2$ thin films" **V. Leca**, G. Rijnders, D.H.A. Blank and H. Rogalla (preprint, 2003)

"Surface morphology of chemically and thermally treated $SrTiO_3$, LSAT, $SrLaAlO_4$ and $KTaO_3$ substrates" **V. Leca**, G. Rijnders, M. Huijbens, D.H.A. Blank and H. Rogalla (preprint, 2003)

"Properties of $Sr_{1-x}La_xCuO_2$ (x = 0.1-0.2) thin films grown by PLD on $SrTiO_3$ and $KTaO_3$" **V. Leca**, G. Rijnders, D.H.A. Blank and H. Rogalla (preprint)

"Structure and properties of $(Ba,Sr,Ca)CuO_2$ superlattices grown by PLD on $NdGaO_3$" **V. Leca**, G. Rijnders, D. H. A. Blank and H. Rogalla (preprint)

Contribution to scientific meetings

Oral presentations

"PLD growth and properties of $Sr_{1-x}La_xCuO_2$ (x = 0.1-0.2) thin films" V. Leca, G. Rijnders, D.H.A. Blank, H. Rogalla, S. Bals and G. van Tendeloo, *E-MRS Conference*, Strasbourg, France (2002)

"Properties of $Sr_{1-x}La_xCuO_2$ thin films grown by PLD" V. Leca, G. Rijnders, D.H.A. Blank, H. Rogalla, S. Bals and G. van Tendeloo, *3rd European Conference on Advanced Materials and Technologies*, Bucharest, Romania (2002)

"Imposed layer-by-layer growth of epitaxial $ReBa_2Cu_3O_{7-x}$ thin films with pulsed laser interval deposition" V. Leca, G. Rijnders, M. Huijben, D.H.A. Blank, H. Rogalla, S. Bals and G. van Tendeloo, *2nd European Conference on Advanced Materials and Technologies*, Bucharest, Romania (2001)

"Imposed layer-by-layer growth of high temperature superconductors with pulsed laser interval deposition" D.H.A. Blank, G. Rijnders, G. Koster, V. Leca and H. Rogalla, *Superconductivity Group Annual Conference*, Birmingham, UK (2001)

"Structure and properties of (Sr,Ca)CuO_2-$BaCuO_2$ superlattices grown by PLD" V. Leca, D.H.A. Blank, G. Rijnders and H. Rogalla, *E-MRS Conference*, Strasbourg, France (2000)

"Deposition, structure and electrical properties of superlattices from Ba-Sr-Ca-Cu-O system" V. Leca, D.H.A. Blank, G. Rijnders and H. Rogalla, *10th CONSILOX Conference*, Alba Iulia, Romania (2000)

"Etching methods for perovskite substrates" V. Leca, D.H.A. Blank, G. Rijnders and H. Rogalla, *10th CONSILOX Conference*, Alba Iulia, Romania (2000)

"Imposed layer-by-layer growth with pulsed laser interval deposition" G. Rijnders, D.H.A. Blank, G. Koster, V. Leca and H. Rogalla, *E-MRS Conference*, Strasbourg, France (2000)

"Initial growth of $SrRuO_3$ on vicinal $SrTiO_3$ substrates using pulsed laser deposition" G. Rijnders, D.H.A. Blank, G. Koster, V. Leca and H. Rogalla, *7th International Workshop on Oxide Electronics, Les Diablerets*, Switzerland (2000)

"Manipulating the nucleation and growth of ReBaCuO" G. Rijnders, D.H.A. Blank, G. Koster, V. Leca and H. Rogalla, *MRS Fall Meeting*, Boston, USA (2000)

"Wet etching methods for perovskite substrates" D.H.A. Blank, V. Leca, G. Rijnders, G. Koster and H. Rogalla, *12th American Conference on Crystal Growth and Epitaxy*, Colorado, SUA (2000)

Poster presentations

"Control of the termination layer of $SrTiO_3$, $NdGaO_3$, LSAT and $SrLaAlO_4$ substrates for thin film growth" V. Leca, G. Rijnders, M. Huijbens, D.H.A. Blank and H. Rogalla, *9th International Workshop on Oxide Electronics*, St. Petersburg, USA (2002)

"Properties of $Sr_{1-x}La_xCuO_2$ (x = 0.1-0.2) thin films grown by PLD" V. Leca, G. Rijnders, D.H.A. Blank and H. Rogalla, *9th International Workshop on Oxide Electronics*, St. Petersburg, USA (2002)

"Initial growth modes of $ACuO_2$ thin films deposited on $NdGaO_3$" V. Leca, G. Rijnders, D.H.A. Blank and H. Rogalla, 5th European Conference on Applied Superconductivity, Copenhagen, Denmark (2001)

"Influence of the structural disorder on the electrical properties of $(Ba,Sr)CuO_2/(Sr,Ca)CuO_2$ superlattices" V. Leca, G. Rijnders, M. Huijbens, D.H.A. Blank and H. Rogalla, *2nd European Conference on Advanced Materials and Technologies*, Bucharest, Romania (2001)

"Surface morphology of annealed and chemically etched perovskite substrates" V. Leca, G. Rijnders, D.H.A. Blank and H. Rogalla, *E-MRS Conference*, Strasbourg, France (2001)

"Wet etching methods for perovskite substrates" V. Leca, G. Rijnders, G. Koster, D.H.A. Blank and H. Rogalla, *7th International Workshop on Oxide Electronics*, Les Diablerets, Switzerland (2000)

"Deposition, morphology and properties of atomically engineered superlattices by PLD" V. Leca, G. Rijnders, G. Koster, D.H.A. Blank and H. Rogalla, *7th International Workshop on Oxide Electronics*, Les Diablerets, Switzerland (2000)

"Growth studies of perovskite heterostructures using in-situ high pressure RHEED" G. Rijnders, V. Leca, D. Mijatovic, D.H.A. Blank and H. Rogalla, *FOM Meeting*, Veldhoven, The Netherlands (2000)

"Wet etching methods for perovskite substrates" V. Leca, G. Rijnders, G. Koster, D.H.A. Blank and H. Rogalla, *MRS Fall Meeting*, Boston, USA (1999)

Acknowledgements

To my family and my friends

The work described in this thesis would not have been possible without the help, knowledge and friendship of several people.

First, I would like to address a special thanks to my supervisors, Prof. Horst Rogalla and Prof. Dave Blank for the opportunity they gave to me to study in the Low Temperature Group and for the time and trust they invested in me. Dave, thank you for your kind help every time a scientific or administrative problem came about, for very creative scientific discussions during the period of my PhD, and for the knowledge you sheared with us. A big *thank you* goes to Guus (Rijnders) for his encouragement, helpfulness, and patience throughout the last four years! Almost everything I know now about the PLD, the "famous" high-pressure RHEED, and thin film growth is due to your patience and huge talent for science and teaching. I enjoyed the time we spent behind the RHEED computer running different experiments. To all of you I owe a deep debt of gratitude.

I would also like to address a heartfelt thanks to a special friend of mine, Cristina (Rusu), who introduced me to the Dutch culture and helped me in difficult moments. I enjoyed every discussion we had and the time we spent together in Enschede, Leuven, Leiden etc. Nicole and Stelian, thank you for your friendship and for all the help. Nicole, good luck with your thesis!

There are a number of people in the Low Temperature Group that made my work easier and pleasant. First, I would like to thanks to you, Dragana, for the numerous discussions we had and the advises you gave to me. Good luck to you also with your thesis! It will be one of the best-written thesis, I am sure … I would like to acknowledge all the people that helped me in my work in the last four years: Mark, Koray (thanks for everything!), Frank and Dick for their technical support, Alexander, Hans, Henk-Jan (thank you for correcting the Dutch summary and for the scientific discussions we had!), Martin (a gentlemen … anytime, anywhere), Johannes, Liane (thanks for the always nice discussions), Sybolt and Gerrit for the help with the XRD experiments. Ans and Inke, thank you for your patience and kind help for all the administrative, travel, and paper work related to my studies. Thanks to everybody from the LT group who shaped my life in the last four years.

Special thanks goes to some MESA+ people: Mark, Rico, and Albert for their SEM, TEM, and XPS measurements. Bert, thanks for all the discussions we had and all the help you gave to me! Henry, thank you for helping me with the Dutch translation!

I cannot forget that without the knowledge and help of some special people from Romania I would not have the opportunity to write this thesis. Special thanks goes to Prof. Mircea Rusu and Mrs. Cornelia Rusu for their unconditional and continuous support and help from the moment they knew me. I hope I will be able to pass on at

least partially your enthusiasm for science! Special thanks goes to Prof. Ecaterina Andronescu, Prof. Maria Preda, and Prof. Virginia Burghelea, from UPB, Dr. Ana-Maria Moisin, Dr. Mihaela Zbarcea and the other people from ICPE, who trusted in me and supported me during and after my studies in Romania.

Bineinteles, nu pot uita suportul oferit de familia mea, de dragostea si grija lor, precum si de bucuria oferita de nepotelele mele, Stefi si Teo. Dar, nu in cele din urma, as vrea sa multumesc sotiei mele, Mihaela, ptr dragostea neconditionata cu care m-a inconjurat din momentul in care ne-am cunoscut si care creste cu trecerea timpului. Vei fi intotdeauna parte din mine si te voi purta cu mine oriunde destinul ma va duce!

Multumesc tuturor! Thank you everybody! Dank je wel allemaal!

To the memory of my father!

Enschede,
May 2003

a b
c d

Snapshots from Romania …

(a) Inside "Cold" cave (Pestera Rece), Bihor County; (b) Peles castle, Sinaia; (c) Episcopal Cathedral, Curtea de Arges; (d) Dracula (Vlad Tepes) Castle, Bran (Brasov County)